Jet activity in top-quark events at $\sqrt{s} = 13$ TeV using 3.2 fb^{-1} data collected by the ATLAS detector

D I S S E R T A T I O N

zur Erlangung des akademischen Grades

doctor rerum naturalium
(Dr. Rer. Nat.)
im Fach Physik

eingereicht an der
Mathematisch-Naturwissenschaftlichen Fakultät
Humboldt-Universität zu Berlin

von
M.Sc. Christoph Eckardt

Präsident der Humboldt-Universität zu Berlin:
Prof. Dr.-Ing. Dr. Sabine Kunst

Dekan der Mathematisch-Naturwissenschaftlichen Fakultät:
Prof. Dr. Elmar Kulke

Gutachter:
1. PD Dr. Klaus Mönig
2. PD Dr. Andreas Meyer
3. Prof. Dr. Thomas Lohse

eingereicht am: 28.03.2019
Tag der mündlichen Prüfung: 23.09.2019

Ich widme diese Arbeit vor allem meiner Frau. Ohne sie hätte ich diese Arbeit wahrscheinlich nie zu Ende geschrieben. Meine beiden Töchter haben mich zusätzlich motiviert ein gutes Vorbild zu sein. Ich liebe euch! Ich habe unglaubliches Glück euch zu haben.
Außerdem widme ich diese Arbeit meinen Eltern, die mich während meines gesamten Studiums unterstützt haben.
Vielen Dank auch an meine hervorragenden Betreuer Klaus und Thorsten. Ich habe mich immer sehr wohl und kompetent betreut gefühlt. Thorsten, deine Begeisterung an der Physik sucht seines Gleichen und ist ansteckend! Zudem habe ich immer die abwechslungsreichen Gespräche mit meinen Kommilitonen Akanksha, Baishali und Elias genossen.

Abstract

In this thesis, the measurement of the normalised differential cross-sections of top quark pair production in association with jets using 3.2 fb^{-1} of proton-proton collision data at a centre-of-mass energy of 13 TeV by the ATLAS experiment at the LHC are presented. Jets are selected from top events which are defined by an opposite-charge electron-muon pair and two *b*-tagged jets in the final state. The cross-sections are measured as functions of several observables are sensitive to additional jets: jet multiplicities, transverse momentum of additional jets, transverse momentum sum of all objects in the event and spatial correlations of the two highest momentum additional jets. The data are corrected to obtain particle-level fiducial cross-section. The resulting measurements are compared to several predictions allowing detailed studies of Monte Carlo QCD modelling.

Zusammenfassung

In dieser Arbeit wird die Messung des normalisierten differentiellen Wechselwirkungsquerschnitts von Top Quark Produktionen mit zusätzlichen Jets präsentiert. Es werden Proton-Proton Kollisionsdaten des ATLAS Experiments am Large Hadron Collider bei einer Schwerpunktsenergie von 13 TeV mit einer Luminosität von 3.2 fb^{-1} verwendet. Die Top Quark Ereignissen werden durch ein entgegengesetzt geladenes Elektron-Muon Paar und zwei *b*-tagged Jets selektiert. Der differentielle Wechselwirkungsquerschnitt wird als Funktion von Observablen, die sensitiv auf zusätzliche Jets sind, gemessen: der Jetmultiplizität, des transversalen Impulses der zusätzlichen Jets, der Summe der transversalen Impulse aller Objekte im Ereignis und räumlichen Korrelationen zwischen den zwei Jets mit dem größten Impulsen. Die gemessenen Daten werden auf Teilchen-Level korrigiert und mit verschiedenen Vorhersagen für detailierte Studien des Monte Carlo QCD Models verglichen.

Contents

1. Introduction

The top quark plays an important role in the Standard Model. It is the heaviest known elementary particle, and its coupling constant to the Higgs boson is expected to be very close to 1. These properties alone make an understanding of top quark events crucial. Accurate modelling of the properties of the top quark is an important part of the LHC program because it is one of the main backgrounds of many other measurements.
In this thesis, the top quark pair ($t\bar{t}$) production in association with additional jets is studied. Additional jets are sensitive to higher-order perturbative QCD effects. A significant contribution to the magnitude of the uncertainty originates from additional jets in precision measurements, like top quark mass or the inclusive $t\bar{t}$ production cross-section measurements in proton-proton ($p - p$) collisions.
The Large Hadron Collider (LHC) [1] is producing millions of top quark events, which allows precise measurements of any top quark characteristic as functions of several kinematic variables. The measurement of normalised differential cross-sections in different bins of jets multiplicity provide high sensitivity to study the effects related to QCD radiation in detail. These effects are hidden in inclusive measurements due to the higher jet multiplicity. Data collected by the ATLAS experiment in 2015 at $\sqrt{s} = 13\,\text{TeV}$ corresponding to an integrated luminosity of 3.2 fb^{-1} is used.
Events with an opposite-charge electron-muon pair and two b-tagged jets in the final state are selected. Additional jets are defined as jets produced in addition to the two b-jets originating from the top quark decays required for the event selection.
The measured data events are corrected for detector effects to allow direct comparisons to several theoretical predictions. The range of available Monte Carlo (MC) predictions for additional QCD radiation varies from parton shower models to methods matching fixed-order QCD with the parton shower or next-to-leading order (NLO) QCD calculations. The results allow tuning of the Monte Carlo simulations to further improve the agreement of future QCD predictions with LHC data.
Measurements of the additional jet activity in $t\bar{t}$ events have been made by ATLAS [2, 3] and CMS [4, 5, 6] earlier. Comparison of the measured distributions with the predictions of Monte Carlo generators with data indicate that some state-of-the-art generators have difficulties in reproducing the data, while others show good agreement with data due to an appropriate tuning of generator parameters.
This thesis is structured as follows. Chapter 2 briefly describes the ATLAS detector. Chapter 3 reviews the theory of top quarks. The simulation of hadron collisions and used Monte Carlo simulations are introduced in Chapter 4. All details related to the study of additional jets in top quark pair events is given in Chapter 5, which is followed by an overview of the used datasets in Chapter 6. Chapter 7 explains the techniques to reconstruct physics objects and Chapter 8 defines the requirements for selecting events. Additionally, the background estimation is presented. The unfolding procedure used to correct the data for experimental biases is outlined in Chapter 9. The sources of systematic uncertainty are detailed in Chapter 10. Chapter 11 presents the fully corrected results with comparisons between simulation and data. A conclusion is drawn in Chapter 12.

2. ATLAS experiment

In this thesis data collected by the ATLAS detector [7] is used. The ATLAS detector is one of the two multi-purpose detectors at the Large Hadron Collider (LHC) [1]. All information about the accelerator and the ATLAS detector are mostly taken from references [1, 8], which can be used for further reading, and represent the design parameters of the LHC.
In Section 2.1 the structure of the LHC accelerator system is presented. Afterwards, the ATLAS detector including the performance that has been reached so far is described in Section 2.2.

2.1. Large Hadron Collider

The Large Hadron Collider (LHC) [1] is a particle collider located in the border region between France and Switzerland. The LHC ring is built in the tunnel of the former Large Electron-Positron Collider (LEP), which has a circumference of 26.7 km and is ∼100 m below the ground. It is designed to collide protons or heavy ions with a centre-of-mass energy $\sqrt{s}$ of up to 14 TeV. This thesis uses data taken from proton-proton ($p-p$) collisions in 2015 when the LHC was operated at $\sqrt{s} = 13\,\text{TeV}$.
Before the protons get injected into the LHC ring, they undergo a series of pre-accelera-tion steps, what is illustrated in Figure 2.1.

2.2. ATLAS detector

The ATLAS detector (A Toroidal Lhc ApparatuS) [7] is a general purpose detector and has a length of 45 m, a height of 22 m and a weight of 7000 tons. It is built in a cylindrical symmetry, with a barrel part around the interaction point[2] and end-caps at each end of the beam pipe. A cut-away view of the detector is illustrated in Figure 2.2.
Its main task is the reconstruction of the primary interactions in the proton-proton collisions by measuring the trajectory and energy of many different kinds of particles. ATLAS consists of several sub-detectors, which can measure the different properties of the particles. They are assembled in increasingly larger concentric cylinders around the interaction point.
There are three main specialised sub-detectors:

- The **Inner detector (ID)** is located just outside the beamline and uses silicon and transition radiation systems to measure the momentum of charged particles and reconstruct vertices produced by primary $p-p$ collisions, as well as secondary vertices from the decay of long-lived particles.
- The **calorimeters** are located radially outward from the ID and designed to measure the energy of particles with a shower sampling method.
- The **muon spectrometer** is located farthest from the IP and measures muon momentum and trajectory.

[2]The interaction point is where the LHC proton beams collide.

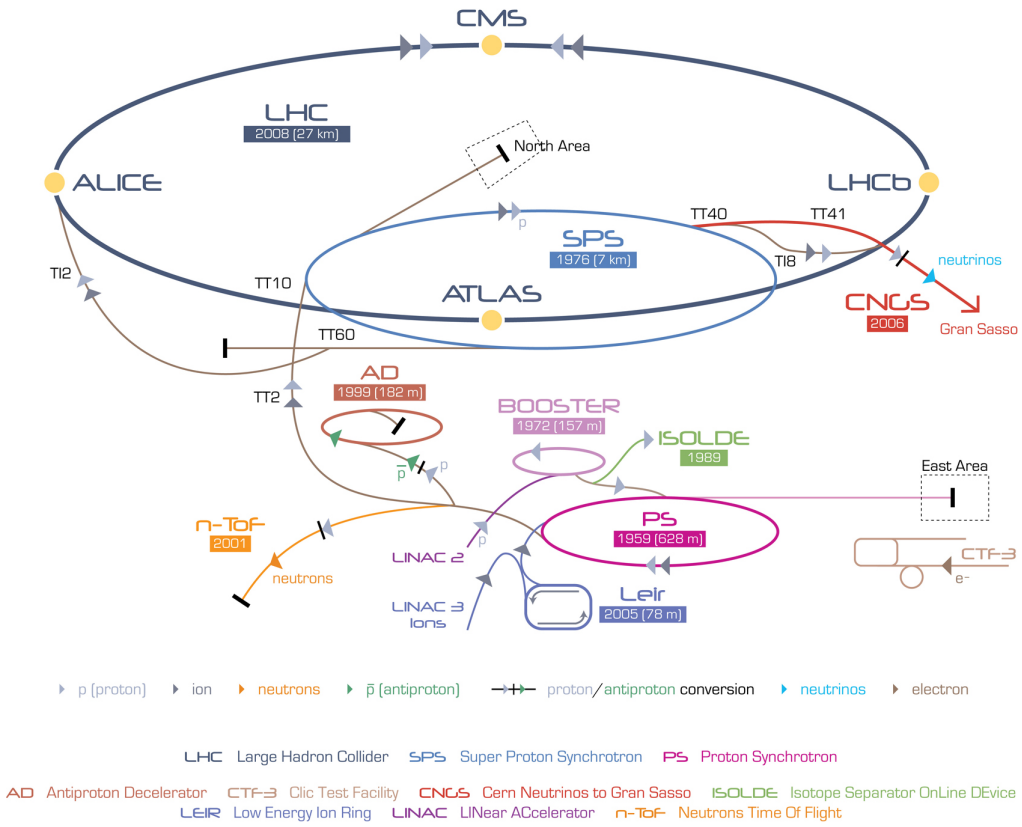

Figure 2.1.: The CERN accelerator complex [9].

Details of each sub-detector are provided below.
Additionally, ATLAS has a magnet system that bends the trajectory of charged particles as they travel through the detector, which allows the particles' momenta to be precisely calculated using the classical Lorentz force equation. The magnet system consists of two configurations. Just outside the ID is a solenoid magnet that produces a field of approximately 2 Tesla. A large toroidal magnet within the outermost part of the detector produces a 1 to 2 Tesla field.

2.2.1. Coordinate system

Due to the cylindrical symmetry, it is common to use a cylindrical coordinate system in the description of positions and directions of particles at ATLAS. The z coordinate describes the position along the beam pipe, whereas a positive z value represents points in the clockwise direction of the LHC ring. ϕ describes the azimuthal angle in the $x-y$ plane, and θ denotes the polar angle between the beam pipe and the particle direction. Particles created in the proton-proton collisions can have large boosts along the z-axis, while the angle θ is not invariant under boosts in this direction. Therefore one commonly uses the pseudorapidity:

$$\eta = -\ln\left(\tan\frac{\theta}{2}\right). \tag{2.1}$$

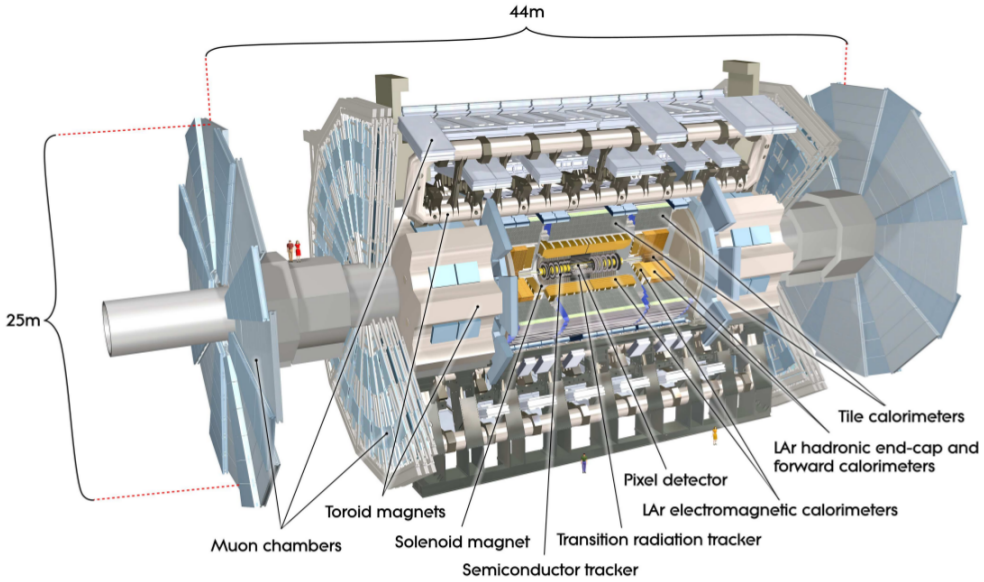

Figure 2.2.: The ATLAS detector with indicated sub-detectors and magnets [7]

Another characteristic quantity is ΔR which describes the spatial difference of two particle tracks in the $\eta - \phi$ space:

$$\Delta R = \sqrt{(\Delta\phi)^2 + (\Delta\eta)^2} \tag{2.2}$$

Due to the unknown longitudinal momenta of the interacting partons, the particle's energy E and momenta p are mostly described by their transverse components:

$$p_T^2 = p_x^2 + p_y^2. \tag{2.3}$$

2.2.2. Inner detector

Next to the beam pipe reside the high resolution tracking detector, the ATLAS Inner Detector (ID) [10]. The purpose of the ID is to make high precision measurements of the position of charged particles as they traverse the detector. The ID has a fine detector granularity to cope with the high particle densities produced by the LHC.
The ID uses silicon sensors and straw drift tubes to detect charged particles, which generate electron-hole pairs when they cross the silicon sensors. Sensors collect these pairs due to an applied electric field. The local coordinates of the sensors allow the identification of the particle position. The same process occurs in the straw drift tubes, where charged particles crossing the drift tubes ionise gas in the straw. The released electrons get recorded after they drifted to the wire at the centre of the straw due to an applied electric field.
The ID is built around the beam pipe with a cylindrical geometry. It consists of central barrel layers, centred around the interaction point, and end-cap wheels or disks at either end of the barrel. This layout allows the ID to cover the full ϕ range and the pseudorapidity range $|\eta| < 2.5$.
The ID has four levels of sub-detectors: the Insertable B-Layer (IBL), the Pixel Detector, the Semiconductor Tracker (SCT) and the Transition Radiation Tracker (TRT). The IBL was inserted as the fourth layer of silicon pixels at a radius of 3.3 cm from the beam line, before the start of

the Run-2 data tacking period. It is the closest sub-detector to the IP and consists of a cylindrical layer of a full length of 3.5 m. The dimensions of the IBL are $50 \times 250\,\text{m}^2$ in the ϕ and z directions. The IBL improves both the transverse and longitudinal impact parameter resolutions compared to Run-1, which results in increased efficiency in reconstructing secondary vertices. It improves tracking by providing an additional measurement point and mitigates the possible loss of hits in the three Pixel detector layers due to the LHC luminosity increasing and to radiation damage [11].
The Pixel uses silicon pixels and provides on average four measurements per charged particle. The pixel sensors have a minimum size of $50 \times 400\,\text{m}^2$ to ensure a position resolution of 10 μm in the $r - \phi$ plane and 115 μm along z or r in the barrel or end-cap region respectively. r refers to the distance perpendicular to the beam axis. This granularity allows a good separation between adjacent tracks.
The SCT surrounds the Pixel sub-detectors and uses silicon strips. Each SCT layer is composed of two silicon strips with a size of $6.4\,\text{cm} \times 80\,\text{m}^2$, whose axes are tilted by 40 mrad to one another. The location of charged particles is determined by pairs of measurements at each SCT layer with an accuracy of 17 μm in $r - \phi$ and with an accuracy of 580 μm along z. The SCT provides four to nine measurements per particle.
The TRT is the largest of the sub-detectors in the ID and consists of drift tubes (straws), which are the detecting elements, with a diameter of 4 mm. In the barrel region the 144 cm long straws are parallel to the beam axis, in the end-cap, they are 37 cm long and arranged radially in wheels. The TRT provides more than 30 position measurements with an accuracy of $\approx$130 μm in ϕ. The straw hits at the outer parts of the sub-detector contribute significantly to the momentum measurement since the lower precision per point compared to the silicon is compensated by a large number of measurements and longer measured track length.

2.2.3. Calorimeters

The calorimeter system follows the tracking device. Most of the particles produced by a $p - p$ collision will deposit their energy via electromagnetic or strong interactions in this part of the detector. The calorimeter system measures both electromagnetic and hadronic showers by stopping hadrons, electrons and photons before they reach the muon system. Separate electromagnetic and hadronic calorimeters, both with a barrel and endcap components, provide full coverage in ϕ and $|\eta| < 4.9$.
ATLAS calorimeters are sampling calorimeters, which means that only part of the show-er energy is observed. Absorbing material used to initiate showers is interleaved with active material for detecting the showers. The energy of the full shower is estimated from the energy measured in the calorimeters.
The particles composing the hadronic showers are different from those composing electromagnetic showers. Electromagnetic showers are produced by a particle that interacts primarily via the electromagnetic force, usually a photon or electron. Hadronic showers are produced by hadrons mostly via the strong nuclear force.
However, the main differences between electromagnetic and hadronic showers are, that electromagnetic showers carry all energy of incoming electrons or photons, while in hadronic showers only a certain fraction of energy is fundamentally undetectable. This difference leads to a diverse calorimeter response. Further calibration is therefore required to take into account these two effects and bring the energy of hadronic showers to their correct energy scale, the hadronic scale. This thesis uses a technique to obtain the hadronic scale, which locally cali-

brates calorimeter cells first and then performs the reconstruction of the observables from calibrated cells.
The energy resolution of electromagnetic calorimeter is $\frac{\sigma_E}{E} = \frac{10\%}{\sqrt{E}} \oplus \frac{30\%}{E} \oplus 0.7\%$, while the hadronic calorimeter has a resolution of $\frac{\sigma_E}{E} = \frac{50\%}{\sqrt{E}} \oplus 3\%$.

2.2.4. Muon spectrometer

Of the known elementary particles only neutrinos and muons pass the ID and the calorimeter system without significant energy loss. The muon spectrometer (MS), which surrounds the calorimeter, measures the position of muons as they traverse the detector. Thus, only neutrinos are not detectable with the ATLAS detector.
The large toroid magnets deflect the tracks of the muons which enables the estimation of the muon momenta. The designed p_{T} resolution $\sigma(p_T)/p_T$ is 4% for muons with $p_T \epsilon [3, 100]$ GeV and it is up to 10% for muons with $p_T = 1$ TeV.

3. Theoretical introduction

This chapter gives a short introduction to the key concepts of the Standard Model (SM) of elementary particle physics while focusing on the heaviest known quark, the top quark. The production and decay of top quarks are explained.

3.1. Standard Model

The Standard Model (SM) of particle physics describes all known elementary particles and three fundamental interactions between them: the strong nuclear force, the weak nuclear force and the electromagnetic force. A complete overview of the SM is given in [12].
The matter we all know is formed by point-like particles with spin-$\frac{1}{2}$, which are called fermions. There are two types of fermions: leptons and quarks. Both types consist of six particles, which are divided into three generations. The first generation contains the lightest and most stable particles, whereas the second and third generations contain the heavier and less-stable particles.
Each lepton generation consists of an electrically charged lepton - neutrino pairs. Char-ged leptons are electrons (e), muons (μ) and tauons (τ). All of them have a neutral partner denoted by the generic symbol ν, the neutrino. A neutrino's flavour matches the flavour of charged leptons as indicated by the subscript. In the SM neutrinos are supposed to be massless but, recent observations suggest that this hypothesis is not correct; neutrinos can oscillate, and in this case neutrinos have mass. The electron is the only stable charged lepton; muons and tauons are both unstable, in fact the mean lifetime is $\tau = 2.2 \times 10^{-6}$ s for the muons, and $\tau = 2.9 \times 10^{-13}$ s for the tauons.
Each quark generation contains one up-type and one down-type quark. They carry fractional electric charges of $\frac{2}{3}|e|$ and $-\frac{1}{3}|e|$. In total six quark types are known: up (u), down (d), strange (s), charm (c), top (t) and bottom (b). In addition to the electric charge, quarks carry a conserved quantum number called colour. So far only colour neutral objects were observed, which is manifested in the confinement of quarks in hadrons. This process is called hadronisation. Hadrons composed out of the heavier quarks s, c, t and b are unstable and decay in typically 10^{-13} s to u and d combinations.
The SM also describes the interactions between the particles. Neutrinos interact only via weak force; leptons additionally interact via the electromagnetic force and quarks interact via strong, weak and electromagnetic forces. The description of the particles and their interactions is done in the framework of a Quantum Field Theory. These forces are mediated by gauge bosons, which are fundamental particles with integer spin. Each fundamental force has its corresponding boson.
The strong interaction is described by a quantum field theory called Quantum Chromodynamics (QCD). The strong force is mediated by massless gluons (g) and is responsible for interactions between quarks and hadrons. The electromagnetic (EM) force is mediated by the massless and chargeless photon (γ). Since the photon is massless, the range of the EM force is infinite. It is described by the gauge theory called Quantum Electrodynamics (QED). The weak force is

mediated by the W and Z bosons and is responsible for nuclear reactions such as beta decay.
The electromagnetic and weak interactions are described by the Electroweak Theory (EWT) which unifies the electromagnetic and weak interactions. The masses of electroweak gauge bosons are generated by interaction with the Higgs field while preserving the local gauge invariance of the SM. This mechanism, named after Brout, Englert and Higgs, is a spontaneous symmetry breaking of EWT. In 2012 the Higgs boson got experimentally discovered [13, 14], which manifests this theory in the SM.
All elementary particles of the SM are modelled by these fields with different properties, which are shown in Figure 3.1. Their masses were rounded and the errors omitted, with the purpose of illustrating only their order of magnitude in comparison to each other. Note that the top quark has the largest mass among all particles.
In fact, there is a fourth fundamental force, the gravitational force. Gravity is the weakest, but it has an infinite range. So far it was not possible to combine the quantum theory used to describe the elementary particle world with the general theory of relativity used to describe the macro world into a single framework. Nevertheless, the Standard Model still works well because the effect of gravity is so weak as to be negligible on the elementary particles.

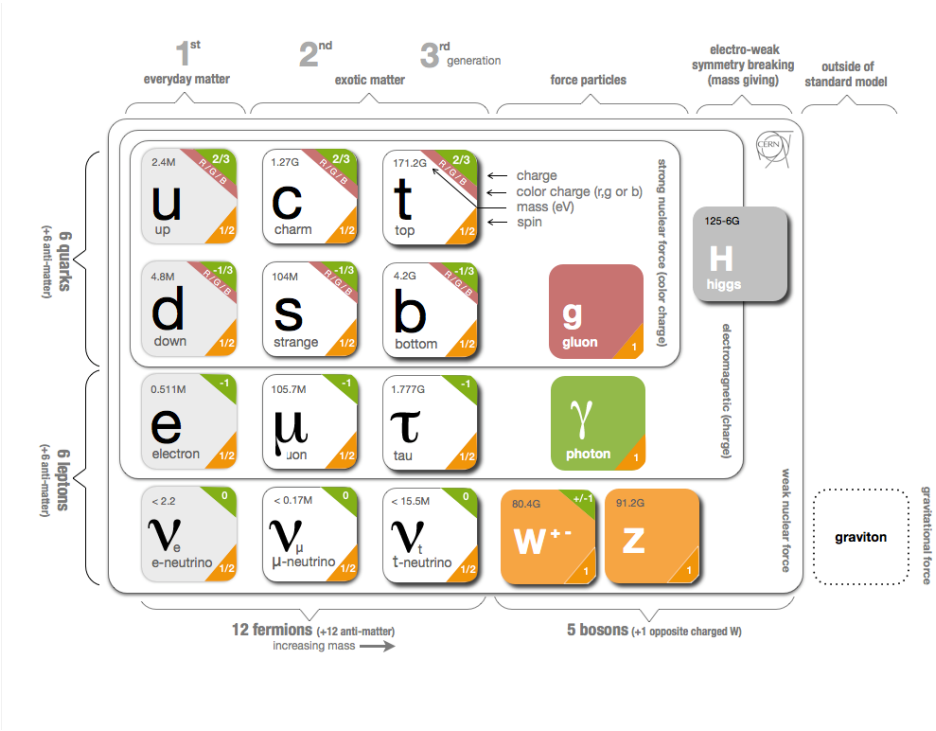

Figure 3.1.: Particles of the standard model. All twelve fundamental fermions are shown on the left side. The mass is written in the upper left corner of each tile in units of eV. The electric charge is given in the green corner in units of electric charge of the proton. The colour charge of quarks is below the electric charge in the red fields. The spin of the particles is written in the orange corner. All colours are reflected by the background colours of the five fundamental bosons which are shown on the right side. Loops indicate which bosons couple to which fermions [15].

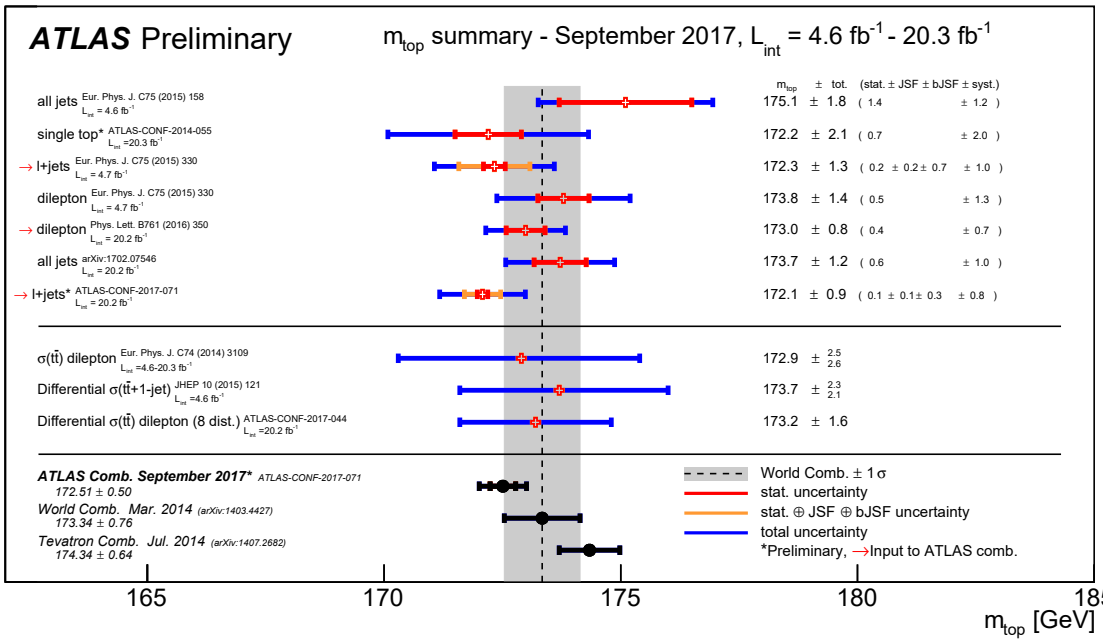

Figure 3.2.: Comparison of the latest ATLAS direct top quark mass m_t measurements and combinations of ATLAS, Tevatron and Tevatron+LHC [16].

3.2. Top quark

Out of all introduced elementary particles within the Standard Model, the top quark is a special particle because of its heavy mass and its short lifetime.
The top quark mass m_t is about the same as a gold atom nucleus, 40 times larger than the next heaviest quark and 10^5 times heavier than the lightest quark. Results from top quark mass measurements performed by ATLAS and Tevatron are shown in Figure 3.2. The current world combination (ATLAS + CMS + Tevatron) for the top quark mass is 173.34 ± 0.76 GeV [16]. The top quark decays before the hadronisation, because of its extremely short lifetime ($\sim 5 \times 10^{-25}$ s).
The top quark was experimentally discovered in 1995 at the Tevatron proton-antiproton ($p - \bar{p}$) collider in FNAL, Chicago. Two experiments, CDF and D0, independently could confirm the discovery. Nowadays the Large Hadron Collider (LHC) is the only experiment, where top quarks are produced and measured by the multipurpose detectors, ATLAS and CMS.
This thesis describes a measurement of the top-antitop ($t\bar{t}$) pair production, which is sensitive to perturbative QCD calculations. It needs to be said, that many other parameters from the SM are highly correlated to top quark properties. For example, the top quark is the only quark that allows a direct measurement of the Cabibbo-Kobayashi-Masakawa (CKM) matrix element $|V_{tb}|$ via top quark decays and single top quark production. Additionally, differential cross section measurements of the $t\bar{t}$ pair production are essential to confirm the SM predictions. A precise understanding of the top quark signal is crucial to claiming new physics.

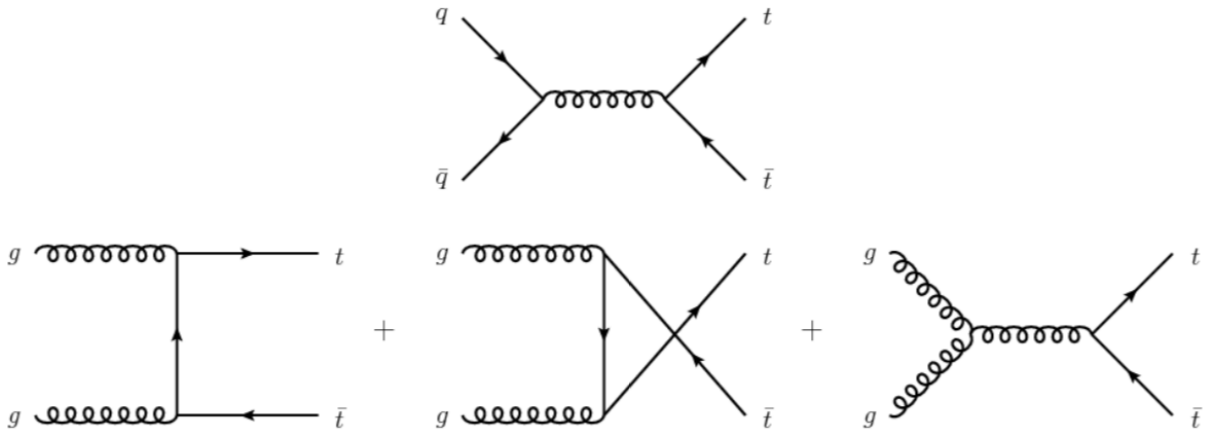

Figure 3.3.: Feynman diagrams for $t\bar{t}$ production at leading order QCD. In the top row the quark-antiquark annihilation is shown, while the bottom row shows the diagrams for the gluon-gluon fusion.

3.2.1. Top quark pair production at the LHC

In proton-proton colliders, top quarks can be produced singly or in pairs. The pair production occurs via the strong interaction. The leading order (LO), the first perturbative order of α_s, production channels for top-antitop quark pairs are gluon-gluon fusion and quark-antiquark ($q\bar{q}$) annihilation. The corresponding Feynman diagrams are shown in Figure 3.3.

At next-to-leading order (NLO), the second perturbative order of α_s, the processes are also a mixture of quark-gluon (qg) or antiquark-gluon ($\bar{q}g$). Some examples of the Feynman diagrams of these NLO processes are shown in Figure 3.4.

The relative contribution of these diagrams depends on the parton distribution functions (PDF), which describe the distribution of momentum among the partons inside a hadron. At the LHC, gluons dominate the PDF of the proton and therefore carry most of the energy of the proton. Thus, gluon-gluon fusion becomes the dominating processes.

Cross-section measurements are necessary to quantify the production of top quark pairs. The high $\sqrt{s}$ reached at the LHC allows considering quarks and gluons in the protons to be quasi-free particles. Therefore it is possible to describe the processes involved in the $p-p$ collisions in terms of interactions between the constituent partons. In Figure Figure 3.5 the parton model for the top quark pair production in a hard scattering process is shown. The two colliding protons P_1 and P_2 have momentum p_1 and p_2 respectively. Each parton i carries a momentum fraction x_i in the proton. The momentum of the parton is then given by $p_i = x_i p_P$, where p_P is the momentum of the proton.

The hard scattering process of two protons can be seen as interaction between the constituents partons of the protons. Therefore the cross sections are calculated as a convolution of PDFs of the colliding protons P_1 and P_2. The PDFs $f_{i/P_1}(x_i, \mu_F^2)$ and $f_{j/P_2}(x_j, \mu_F^2)$) describe the probability density for finding a parton i (j) inside the proton P_1 (P_2) carrying a momentum fraction x_i (x_j) at factorisation scale μ_F^2.

The inclusive production cross section of the process of $t\bar{t}$production can then be calculated by

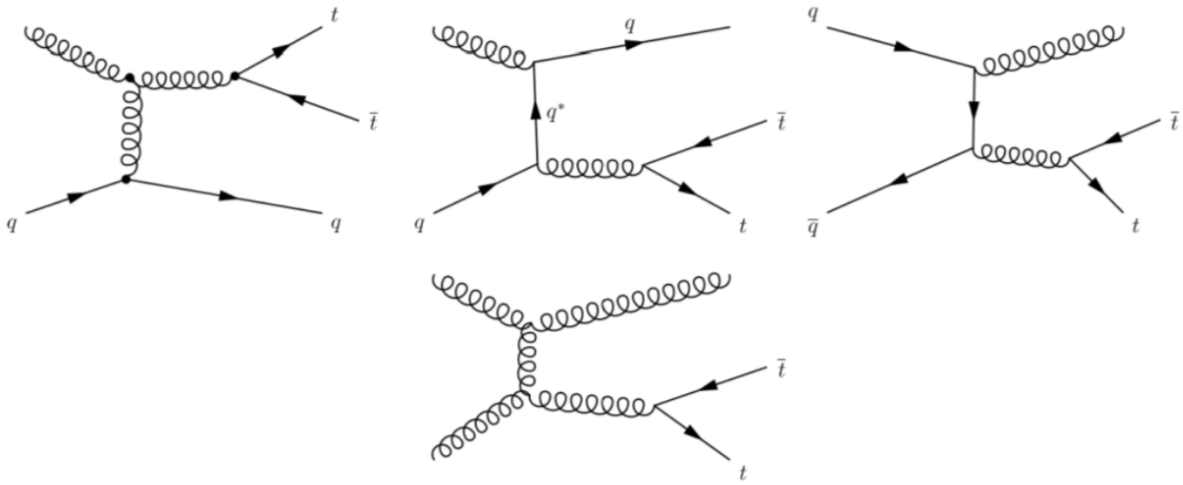

Figure 3.4.: Feynman diagrams for $t\bar{t}$ production at next-to-leading order QCD. In the top row, the quark-antiquark annihilation is shown, while the bottom row shows the diagrams for the gluon-gluon fusion.

using the factorisation theorem [17] and is given by:

$$\sigma^{P_1P_2\to t\bar{t}+X}(s,m_t) = \sum_{i,j=q,\bar{q},g} \int \mathrm{d}x_i \mathrm{d}x_j f_{i/P_1}(x_i,\mu_F^2) f_{j/P_2}(x_j,\mu_F^2) \hat{\sigma}^{ij\to t\bar{t}}(\hat{s},m_t^2,\alpha_s(\mu_R^2),\mu_F^2,\mu_R^2), \quad (3.1)$$

where α_s is strong coupling constant and $\hat{s}$ is the square of the center-of-mass energy of the colliding partons: $\hat{s} = (p_i + p_j)^2 = (x_i p_{P_1} + x_j p_{P_2})^2$. The sum runs over all pairs of partons (i, j) contributing to the process.
Furthermore, μ_R and μ_F are the renormalisation and factorisation scales, respectively. The partonic cross section $\hat{\sigma}$ can be expanded in fixed order series in $\alpha_s$as:

$$\hat{\sigma}_{ij\to t\bar{t}} = \alpha_s^2 \left[\hat{\sigma}(0) + \alpha_s \hat{\sigma}(1) + \mathcal{O}(2)\right] \quad (3.2)$$

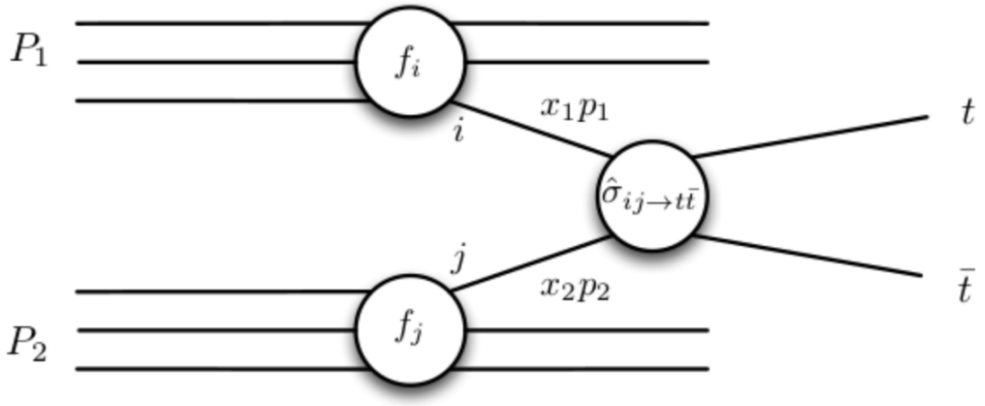

Figure 3.5.: The top quark pair production of a hard scattering process in the parton model.

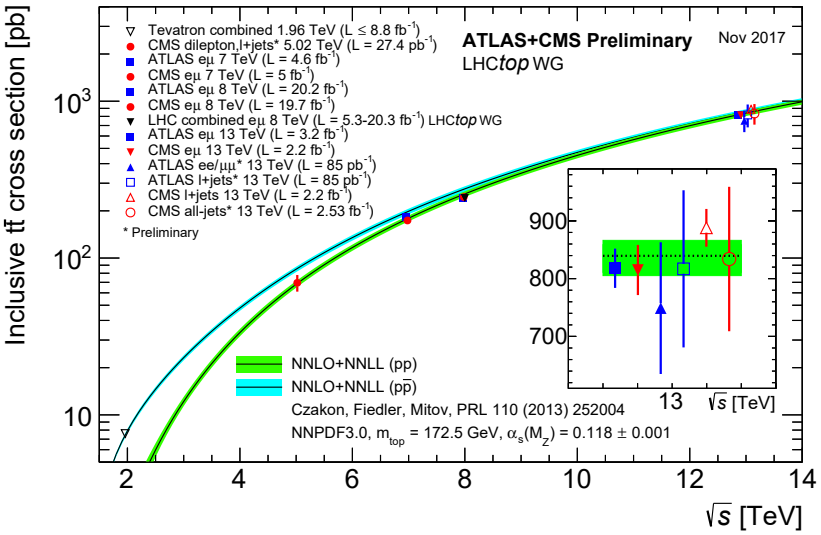

Figure 3.6.: Summary of LHC and Tevatron measurements of the $t\bar{t}$ production cross-section as a function of $\sqrt{s}$. Comparisons to NNLO+NNLL QCD calculation are shown. The measurements and the theory calculation are quoted at $m_t = 172.5$ GeV. Measurements made at the same centre-of-mass energy are slightly offset for clarity [16].

where the first term is the contribution at LO and $\hat{\sigma}(1)$ is the contribution at NLO.
The PDFs are evaluated at the factorisation scale μ_F^2 and α_s at the renormalisation scale μ_R^2 and account for divergences coming from loop diagrams. Both scale values are input to the MC generator calculation and handle the infinities cancellation and renormalisation which took place internally to the hard process generator. These two scales are chosen to be equal since they both give the scale at which perturbative calculation is separated by other effects. In the case of the top quark production, one typically evaluates the cross sections at $\mu = m_t$. The changes when varying μ between $m_t/2$ and $2m_t$ are usually quoted as an indicative theoretical uncertainty [18].
This calculation, of course, requires a given set of PDFs, which is further discussed in Section 4.1.1. Measurements of deep-inelastic-scattering are fitted to determined the PDFs by a variety of experiments. Many different collaborations perform several variations of fits to the data. These PDF sets are required to calculate the production cross section in all Monte Carlo (MC) generators. Therefore they are programmatically accessed via LHAPDF6 [19], which is a software tool providing PDF packages for experimental and phenomenological purposes.
Measurements of the total cross-section of top quark pair production at the Tevatron and the LHC are shown in Figure Figure 3.6. The theoretical prediction is computed at next-to-next-to-leading order (NNLO) with next-to-next-to-leading-log soft gluon resummation (NNLL) [20] with a final theoretical uncertainty of ∼3%. The NNLO+NNLL QCD prediction is in very good agreement with all measurements, including preliminary measurements at $\sqrt{s} = 13$ TeV.

3.2.2. Top quark decays

Top quarks decay to a W boson and a down-type quark: $t \to qW$ where $q = b, s, d$. In practice, the down-type quark is almost always a bottom quark, which is due to the CKM matrix element

$|V_{tb}|$, which is constrained by weak hadron decays and the unitary of the matrix. The average of Tevatron and LHC measurements combines to 1.009 ± 0.031 [21]. The rate of the $t \to qW$ decays is proportional to the square of the corresponding CKM matrix elements, $|V_{tq}|^2$ [12]. The top quark decay is distinguished by the two decay modes of the W boson: leptonic and hadronic. Therefore there are three different channels possible for $t\bar{t}$ decays:

1. **All hadronic:** Both W bosons decay hadronically: $t\bar{t} \to WbWb \to bbqqqq$. Because there are six quarks in the final state, this channel has a large multi-jet background, which can be difficult to subtract. However, 46% of the top pairs decay via this channel.

2. **Semileptonic:** One W boson decays to a quark pair and the other decays to a lepton and neutrino: $t\bar{t} \to WbWb \to bbqql\nu$. This channel is usually further differentiated by lepton flavour. 45% of the $t\bar{t}$ events decay semileptonically.

3. **Dileptonic:** Both W bosons decay to leptons: $t\bar{t} \to WbWb \to bbl\nu l\nu$. Though the dilepton channel has the fewest events, it often provides the least background. Only 9% of the top pairs decays have two leptons in the final state.

In this thesis the dilepton channel is used, where one lepton is an electron while the other is a muon, called $e\mu$ channel. This channel provides a minimal background and allows, therefore, more robust generator comparisons. Details of the event reconstruction are given in Chapter 8.

4. The physics of hadron colliders

The theoretical predictions of hadron collisions at the LHC are complicated, because of several aspects of these collisions: the energies of the colliding partons and the boost along the beam direction are unknown; there is a large probability for low-energy processes, and the simulation of the strong interactions of the partons is challenging.
In this chapter, the main concepts of event simulation of hadron collisions are discussed, and the Monte Carlo generators used in this thesis are introduced. Furthermore, the simulation of the detector geometry and digitisation of the energy deposited in the sensitive regions of the detector is explained.

4.1. Simulation of hadron collisions

The events of hadron colliders tend to be very complex, which is shown in a schematic example event in Figure 4.1. Hundreds of particles are produced through many types of physics processes. The event simulation is done step-by-step in Monte Carlo (MC) generators. Random numbers are taken from quantum mechanical probability distributions [12, 22] to simulate processes. Averaging over a large number of events gives the expected final distribution of events. In the end, the simulation should accurately describe the average final state particles as well as fluctuations around the average.
In the next sections, the following steps to generate an event at the LHC are discussed:

1. Parton distribution function (PDF)
2. Hard process
3. Parton shower
4. Hadronization
5. Final state
6. Detector simulation

4.1.1. Parton distribution function

As already explained in Section 3.2.1, simulating a collision of two protons requires the knowledge of the energy distributions among the partons.
Measurements of deep-inelastic-scattering are fitted to the data by a variety of experiments to determine the PDFs. These PDF sets are required to calculate the production cross section in all Monte Carlo (MC) generators. Therefore they are programmatically accessed via LHAPDF6 [19], which is a software tool providing PDF packages for experimental and phenomenological purposes.

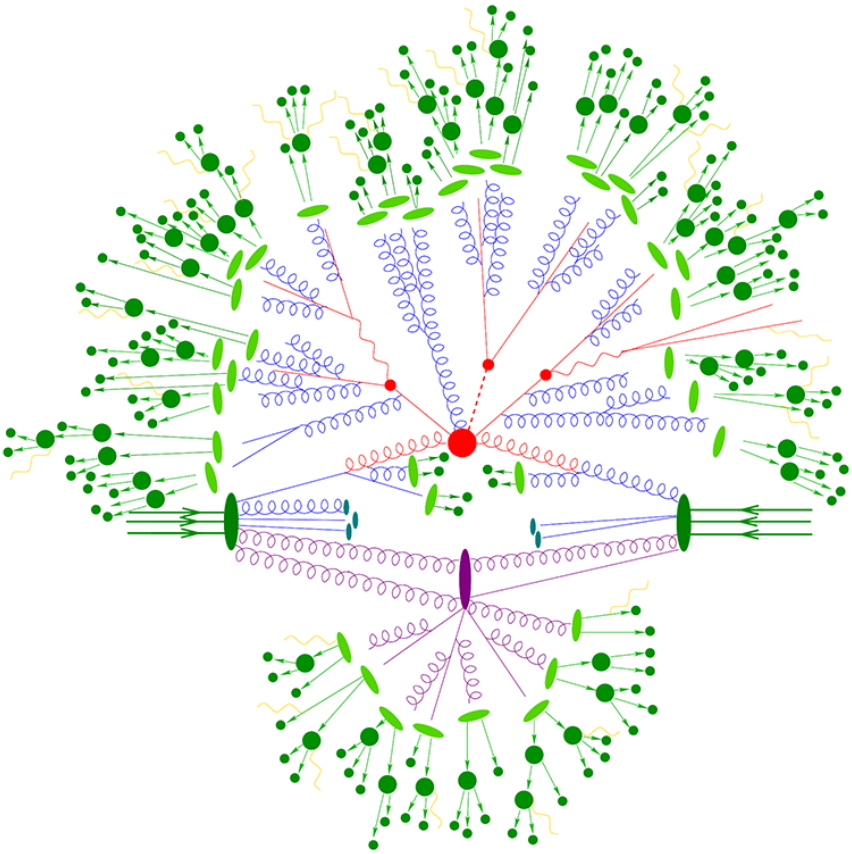

Figure 4.1.: Visualization of a top pair event from the Sherpa event generator. The hard scatter is shown in red, the parton shower in blue, the hadronzation in green, the underlying event in purple, and the QED final state radiation in yellow [23].

4.1.2. Simulation of the hard process

The two colliding protons are simulated as a group of partons with a centre-of-mass energy of 13 TeV. Each parton has a momentum according to the proton PDFs. One parton of each proton collide and form the hard process (marked red in Figure 4.1). Hard processes are defined by having a substantial momentum transfer with respect to the QCD scale. In this regime, the strong coupling constant α_s is perturbative. In contrast, non-perturbative effects in soft emission require complicated techniques, like parton showering as described in Section 4.1.3.
The generation of an MC event is evaluated by the corresponding matrix elements (ME) of the process of interest, calculated to some fixed order in perturbative QCD (pQCD), typically LO or NLO in α_s. In this thesis, the process of interest is the $t\bar{t}$ pair production, and therefore all Feynman diagrams that contribute to the $t\bar{t}$ pair production must be calculated and summed coherently.
Unstable particles like top quarks or W/Z bosons further decay as part of the hard process in order to properly transfer properties such as spin correlations. Therefore, in this thesis, the signal process is simulated as $gg \to t\bar{t} \to WbWb \to bblvlv$.

4.1.3. Parton showers

The emission of QCD radiation by partons is collectively called the parton shower (PS). The PS is used in MC generators to approximately simulate higher order terms of the perturbation expansion which are beyond the fixed order prediction. The parton shower can be applied to the initial state partons or to the final state partons, which is called initial state radiation (ISR) and final state radiation (FSR), respectively.
Several PS models are built on soft and collinear approximations to the full cross sections [24]. They are not able to consistently describe the wide-angle emissions and multi-jet final states.
Most MC generators generating $t\bar{t}$ events use fixed order prediction at NLO QCD which is then supplemented by PS. It is crucial to avoid double-counting of phase-space configurations when matching the fixed order calculation with the PS. There are several approaches on how to match PS with fixed order calculation, see [24].
The parton shower cannot give an approximate estimate on the total cross section from the missing higher order terms of the perturbation expansion. Therefore, the usual procedure of the simulation of $t\bar{t}$ events is to use MC generator at NLO QCD supplemented by PS, and normalise the distributions to the available prediction of higher order $t\bar{t}$ total cross section (nowadays NNLO+NNLL QCD).

4.1.4. Hadronisation

After all post-shower partons have an energy of below 1 GeV, where perturbative QCD can no longer be used, partons are confined into physically observable hadrons in the hadronisation step. The first-principles theory does not explain the process of hadronisation, but there are several phenomenological models for it. The two most common models are the Lund string model [25, 26] and the cluster model [27].
The string model, which is used by the MC generator Pythia [28, 29], models the confinement field as strings between two partons. When a string is stretched, it may break and from a new parton-pair connected via a string. At some point, the strings are relaxed and have low energy. The partons form hadrons.
The cluster model, which is used by Herwig++ [30, 31] and Sherpa [32], groups quark pairs into colourless clusters. These clusters then decay into other colourless clusters or SM hadrons until only SM hadrons remain.

4.1.5. Underlying event

The process of multiple parton collisions within the same $p - p$ collisions are called multiparton interactions (MPI) [33]. These are typically soft collisions between additional partons that were not involved in the hard scattering. MPI are usually simulated as $2 \rightarrow 2$ QCD process at low energies, which might influence the overall particle multiplicity of the final state and the overall colour flow of an event.
To simulate MPI an accurate description of low-energy strong interaction processes is essential. In the Minimum Bias analysis outlined in Section 4.3, charged-particle distributions have been measured to improve the understanding of these processes.

4.1.6. Monte Carlo generators

There are several MC generators available, which can be divided into two groups: general-purpose generators and fixed order ME generators.
General-purpose generators such as Pythia [28, 29], Herwig++ [30, 31], and Sherpa [32] can handle the entire process, from ME to PS and hadronization. These generators automatically calculate all relevant Feynman diagrams for a user-requested process. The required phase-space integrations are then performed, before applying parton shower algorithms and models of hadronisation and the underlying event.
ME generators such as MG5_aMC@NLO[34] and Powheg[35, 36] only generate a fixed order calculation of the hard process and must be interfaced to another generator, e.g. Pythia or Herwig++, for the PS. However, it is tricky to merge the hard process calculation with a PS. It is necessary to avoid double counting of partons, because both may produce wide-angle radiation.
MG5_aMC@NLO and Powheg use two different methods to avoid double-counting. MG5_aMC@NLO analytically computes which parts of the NLO calculation are already present in the PS and then subtracts this portion from the shower before combining. For Powheg, the probability of each iterative spread of the shower is modified for the first emission such that approximately NLO accuracy is reached. Then, any PS program can be used to shower the rest of the event with a p_{T} veto to ensure that the PS program does not produce any emissions harder than those from the NLO.

4.1.7. Detector simulation

After the previous steps, the generated final state particles, hadrons and showers are processed through a detector simulation. Many of the hadrons are unstable and decay at different timescales. Some of these decays take place within the detector volume. In GEANT4[37] the whole ATLAS detector geometry is built, which provides models for physics and infrastructure for particle propagation. So-called "hits" containing the energy deposition, position and time are recorded when particels travel through the detector [38, 39]. Instead of full ATLAS detector simulation, it is possible to use a faster simulation making use of parameterised showers in the calorimeters [39].
In the digitisation step, these hits from each subdetector are translated into signals identical to the output of the ATLAS data acquisition system, i.e. similar to the real detector output (raw data). Therefore the same ATLAS trigger and reconstruction packages can be used for simulated and real data from the detector [38].

4.1.8. Tuning and corrections of simulations

To improve theoretical predictions, it is possible to tune generators by changing parameters of the showering and hadronisation to match experimental data. Each generator has many relatively free parameters, most used to model the non-perturbative hadronisation process but also some for the perturbative hard interaction. All of these parameters have a physical motivation but are usually only known via rough scale approximations. Some parameters like α_s can be measured experimentally but still must be adjusted since generators use them in a fixed-order scheme, unlike nature. These parameters can be grouped into sets such as flavour, fragmentation, and hard process. Most of the hard process parameters are tunes to Tevatron and LHC data, while most of the hadronisation parameters come from LEP. The measurement

of this thesis is important for future tuning of PS parameters since additional jets are sensitive to ISR/FSR.
Furthermore, each MC event can have a particular event weight. This event weight is used to achieve better statistics in phase space regions with a low cross-section or to avoid double counting from the ME to PS matching step. Additional weights are used to correct for imperfect detector conditions.

4.2. Monte Carlo samples

In the following the MC samples used to develop the analysis, which includes correcting the data for detector acceptance and resolution effects, determining uncertainties, modelling background processes and comparing to data events, are presented.
All MC samples are scaled to the total integrated luminosity $\mathcal{L} = 3.2$ fb^{-1} corresponding to the data used in this measurement.

4.2.1. Signal samples

Several $t\bar{t}$ MC samples are used in this thesis. The reference sample, also called nominal sample, is simulated by Powheg+PYTHIA 6. Also, alternative generators and PS models are used to estimated modelling uncertainties (details in Section 10.2) or to compare to the unfolded data distributions.

Powheg+PYTHIA 6 $t\bar{t}$ sample

The nominal $t\bar{t}$ sample uses the NLO Powheg-Box v2 matrix-element generator [35, 36, 40], referred to as Powheg in the following, to generate the hard scattering process. It is interfaced to the CT10 [41] NLO PDF set. The resummation damping parameter (h_{damp}) controls the p_{T} of the first additional emission beyond the Born configuration and therefore regulate the high-p_{T} emission against which the $t\bar{t}$ system recoils. In the nominal $t\bar{t}$ sample, it is equal to the mass of the top quark (m_t). In previous analyses, the modelling of the $t\bar{t}$ system kinematics with respect to data improved by choosing this h_{damp} value [42].
PYTHIA 6 [28] (v6.427) is used to simulate the parton shower, hadronisation and underlying event with the Perugia 2012 set of tuned parameters (tune) [43] and the LO CTEQ6L1 PDF set [44].
The hard process renormalisation and factorisation scales are set to the default generator value $\mu^2 = m_t^2 + p_{\text{T}}^2$, where m_t^2 is the top quark mass and p_{T} refers to the transverse momentum of the top quark before QCD radiation.
Low and high radiation settings are investigated by Powheg+PYTHIA 6 samples, where the renormalisation and factorisation scales are varied by a factor of 0.5 (2) and the value of h_{damp} is varied to m_t ($2m_t$) respectively [42, 45]. These varaitions are called RadLo and RadHi in the following and correspond to less and more parton-shower radiation respectively.

Powheg+Herwig++ $t\bar{t}$ sample

The hard process of this sample is generated with the same setup as for the nominal sample, but in this case, the PS, hadronisation and the underlying events are simulated using Herwig++ [30] (v2.7.1) with the UE-EE-5 tune [46] and the corresponding CTEQ6L1 PDFs.

MadGraph5_aMC@NLO+Herwig++ $t\bar{t}$ sample

This sample is generated by MadGraph5_aMC@NLO [34] (v2.2.1), referred to as MG5_aMC@NLO hereafter, with NLO ME and CT10 PDF sets. The central scale set to $\mu^2 = m_t^2 + 0.5 \times (p_{\mathrm{T},t}^2 + p_{\mathrm{T},\bar{t}}^2)$, where $p_{\mathrm{T},t}$ and $p_{\mathrm{T},\bar{t}}$ refer to the p_{T} of the top and antitop quark, respectively. Similar to the Powheg+Herwig++ $t\bar{t}$ sample, Herwig++ is used to simulate the PS, hadronisation and the underlying events.

Powheg+PYTHIA 8 $t\bar{t}$ sample

The same generated hard process as the nominal sample is interfaced with PYTHIA 8 [28, 29] (v8.183) with A14 tune and the corresponding CTEQ6L1 PDFs.

MadGraph5_aMC@NLO+PYTHIA 8 $t\bar{t}$ sample

This sample is generated using MG5_aMC@NLO (v2.2.1) interfaced by Pythia8 (v8.183) with A14 tune and the corresponding NNPDF2.3LO PDF.

Sherpa v2.2 $t\bar{t}$ sample

Improved precision is expected from using Sherpa [47] (v2.2). The events are generated at NLO for inclusive and the one additional jet process and at LO for up to four partons using the OPENLOOPS [48] and COMIX [49] matrix-element generators. The matrix elements are merged with the SHERPA PS [50] using the ME+PS@NLO prescription [32, 51].

All samples described are normalised to the cross-section $\sigma = 832^{+20}_{-29}(scale)^{+35}_{-35}(PDF)$ pb as calculated with the TOP++2.0 program at NNLO accuracy in pQCD including NNLL soft-gluon resummation, while taking a top quark mass $m_t = 172.5$ GeV.

4.2.2. Background samples

Several background events can pass a $t\bar{t}$ signal selection due to other physics processes producing the same final state or due to misidentification of objects by the detector. These events are subtracted from data using the unfolding procedure as described in Section 9.3. The processes considered are the single top quark production, Drell-Yan and diboson final states.

Single top sample

Single-top quark events associated with a W boson (Wt) are simulated using Powheg+PYTHIA 6. The same configuration as used for the nominal $t\bar{t}$ sample were used. The Wt single top background is determined from MC simulation and normalised to the approximate NNLO cross-section of 71.7 ± 3.8 pb, determined as in Ref. [52]. Two different predictions were simulated in order to resolve the interferences with the $t\bar{t}$ final state at next-to-leading order. The "diagram removal" (DR) generation scheme is used to remove the interference part of the phase space from the background calculation. Alternatively, the "diagram subtraction" (DS) method [53] is used to generate a sample that allows evaluating systematic uncertainties for the interference removal.

Drell-Yan sample

The Drell-Yan background originating from events with a $Z/\gamma^* \to \tau\tau \to e\mu$ is simulated with Sherpa v2.1 [32] interfaced with the CT10 PDF set [41]. The matrix elements at NLO contain up to two partons and at LO up to four partons. The total cross-section is normalised to NNLO predictions [54].

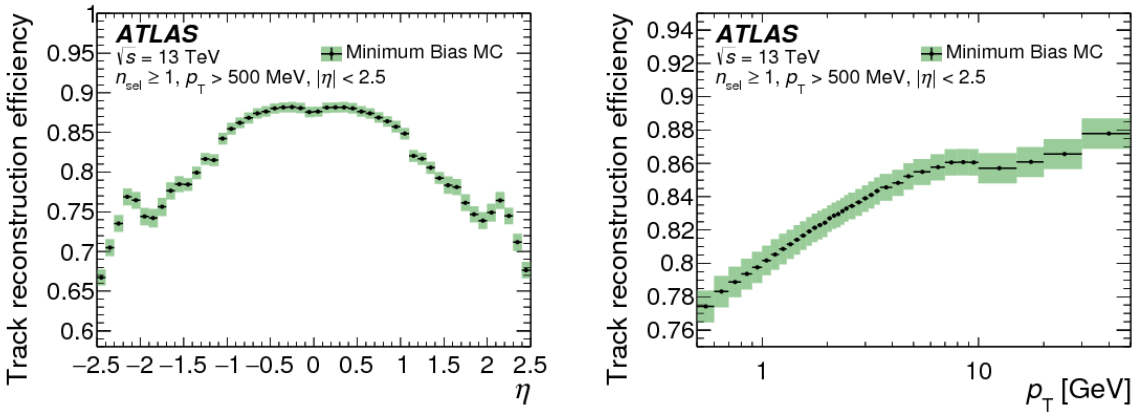

Figure 4.2.: Track reconstruction efficiency of tracks matched to stable particles as a function of (a) η and (b) p_{T} of the stable particle.

Di-boson sample

Di-boson processes, where both decay leptonically, were simulated using the Sherpa v2.1 event generator. They are calculated for up to one (ZZ) or zero (WW, WZ) additional partons at NLO and up to three additional partons at LO using the same methods for ME and PS simulation as used for Drell-Yan. The CT10 PDF sets were used in conjunction with dedicated parton shower tuning developed by the authors of Sherpa. The event generator cross sections, which are already at the NLO accuracy, are used in this case.

4.3. Minimum Bias analysis

Measurements of charged-particle multiplicities, as published in [55], are an important input for pile-up modelling in $p-p$ collisions and a handle on multi-parton interactions at the LHC. They provide insight into many aspects of non-perturbative QCD in hadron collisions.
At the beginning of the 2015 data taking, during a special LHC fill with low pile-up, the ATLAS detector recorded data with an integrated luminosity of 170 μb^{-1}. In the Minimum Bias analysis, the charged-particle multiplicity is measured as a function of transverse momentum and pseudorapidity. Additionally, the dependence of the mean transverse momentum on the charged-particle multiplicity is studied. Charged particles are required to have $p_{\mathrm{T}} > 500$ MeV and $|\eta| > 2.5$. The events are expected to have at least one charged particle satisfying these kinematic requirements.
The distributions are unfolded to particle level by using a Bayesian unfolding similarly as described in Chapter 9. The main correction factor during the unfolding procedure is the tracking efficiency, which is defined as the ratio of reconstructed tracks that correspond to an actual generated stable particle[1] and the total number of stable particle in the kinematic range. Figure 4.2 shows the measured tracking efficiency. Additionally, the data events are corrected for the trigger, and vertex inefficiencies and contributions from secondary particles[2] and strange baryons are subtracted. The resulting charged-particle multiplicities are shown in Figure 4.3.

[1]Stable particles have a lifetime greater than 300 ps.
[2]Secondary particles are particles that decay before or during the flight through the ID.

These measurements provide important and tighter constraints on existing models of soft QCD interactions.

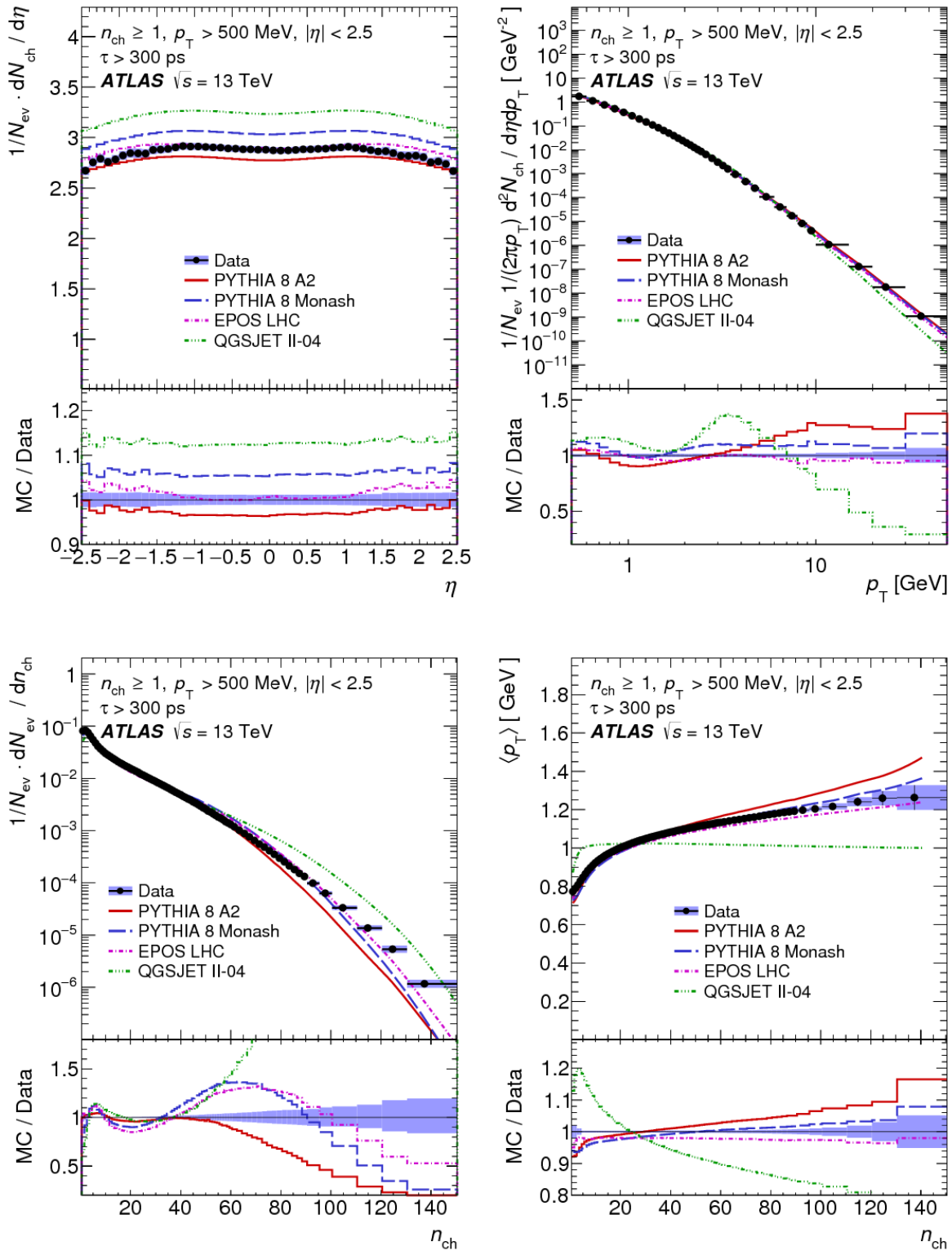

Figure 4.3.: Charged-particle multiplicities as a function of (a) η, (b) p_T, (c) the multiplicity of charged particles n_{ch}, and (d) the mean transverse momentum versus n_{ch}.

5. Analysis of extra jets in $t\bar{t}$ events

This thesis presents a measurement of the activity of additional (a.k.a. extra) jets produced in association with $t\bar{t}$ decay products. In this analysis both top quarks decay leptonically into an $e\mu$ pair, resulting in a final state with at least two b-tagged jets and the two leptons. The extra jets and the b-jets are constructed with the $R = 0.4$ anti-k_T algorithm, which is introduced in Section 5.1.
Additional jets mainly arise from hard gluon emissions from the hard-scattering interaction beyond $t\bar{t}$ production. The high centre-of-mass energy in LHC Run 2 ($\sqrt{s} = 13\,\text{TeV}$) opens a large kinematic phase space for QCD radiation. As already pointed out in Section 4.1, several theoretical approaches are available to model the production of these jets, which are described in Section 5.2.
This analysis aims to test the theoretical predictions of additional jet production mechanisms and to provide data to optimise predictions by adjusting the free parameters of the models. In the last Section 5.4, the analysis strategy and the measured distributions are presented.

5.1. Definition of jets

The gluons and quarks in the final state of the initial process of the beam collision are not measurable. Via hadronisation these particles produce hadrons. After further decay, we will observe the bunches of particles in the detector. They will leave an energy deposit in the detector calorimeter cells which is measurable. Jet reconstruction algorithms try to group these energy deposits by building a jet.
Each jet reconstructs initial partons from the ME (hard partons) after parton shower. However, a jet may contain parts of showers from multiple partons and ISR/FSR. Since a jet is not a fundamental physics object, there have to be rules to define them correctly. A jet has to be well defined and yield finite cross sections at any order of perturbation theory. Additionally, jets have to be infrared and collinear (IRC) safe [56]. Therefore jets should be stable under a modification of final state particles via soft emissions or collinear splitting to avoid infinite results in calculations due to infrared divergences.
There are three IR and collinear safe jet algorithms used by the ATLAS collaboration: the anti-k_T[57], k_T[58, 59, 60] and the Cambridge/Aachen (C/A) [61, 62] algorithm, which are all implemented in the FastJet package [63, 64].
The jet algorithms start with a list of all objects (particles, partons or clusters) and define for every entry i the distance:

$$d_i = p_{T,i}^{2n}, \tag{5.1}$$

where p_T is the transverse momentum of the entry i and n defines the algorithm and is equal to -1 (anti-k_T), 0 (C/A) or 1 (k_T).

For each pair of entries (i,j) the distance between them is defined as:

$$d_{ij} = \frac{\Delta R_{ij}^2}{R^2} \min\left(p_{T,i}^{2n}, p_{T,j}^{2n}\right), \tag{5.2}$$

where ΔR_{ij} is the separation between the objects in $\eta - \phi$-space. R controls the size of the resultant jet, which is given by the user.
If $d_{ij} < d_i$, then the entries i and j are merged into a new entry k. But if the minimum is a d_i, then the entry i is saved as a jet and i is removed from the list. This procedure is repeated until all entries are formed to jets.
The anti-k_T algorithm uses $n = -1$ and from the definition of the algorithm one can see that the objects with the most of the energy deposited are merged first. The resulting jets are conical in the $\eta - \phi$-space (see Figure 5.1(b)). However, the k_T algorithm ($n = 1$) combines low energy objects first, which produces jets with irregular shapes (Figure 5.1(a)). $n = 0$ refers to the Cambridge/Aachen algorithm and its shape is shown in Figure 5.1(c), which has no p_T ordering and combines the closest entries in η-ϕ space first.
Since anti-k_T algorithm uses the highest p_T constituents first, the jet axis stabilises after the first few combination and results in circular jets. Circular jets have better-defined acceptance, are easier to calibrate, and have more straightforward corrections for the pile-up. These advantages of the anti-k_T algorithm motivate its adoption as the ATLAS default and its use in this thesis.

5.2. QCD radiation and additional jets in top quark pair events

Similarly to the electron emitting photons via Bremsstrahlung, colour charged particles, like partons, can emit QCD radiation. Partons emit radiation either before or after the collision, which is called Initial State Radiation (ISR) or Final State Radiation (FSR) respectively. These emissions are collectively called the parton shower (PS). A true QCD calculation involves matrix elements that can interfere and hence no unique distinction between ISR and FSR is possible. The distinction between ISR and FSR makes sense in the context of MC generators because generators use a probabilistic approach that ignores such interference.
On the one hand, matrix elements give a good description of specific parton topologies where the partons have high energy and are well separated. However, in the soft and collinear limit, they neglect interference between multiple gluon emissions, e.g. angular ordering. On the other hand, parton showers include soft and collinear radiation that is logarithmically enhanced. Partons have low energies and small angles from the shower initiator.
A visualisation of generating inclusive $t\bar{t}$ events with NLO accuracy, like Powheg and MG5_aMC@NLO, is given in Figure 5.2. As the inclusive $t\bar{t}$ events are produced with NLO accuracy (Figure 5.2a), the first additional jet, originating from the real emission piece of the NLO calculation, has only leading order accuracy in QCD (Figure 5.2b). The generated events at parton level (partons from ME calculation) are then interfaced to MC programs to provide the parton shower, hadronisation and underlying event models (Figure 5.2c). Jets originating from the parton shower are often quoted as having leading logarithmic accuracy.
Sherpa was used to produce $t\bar{t}$+jets events with LO accuracy, which is schematically visualised in Figure 5.3. Contrary to the NLO generators, the inclusive $t\bar{t}$ system is produced with just LO accuracy (Figure 5.3a). However, the matrix elements for $t\bar{t}$ production with multiple additional partons in the final state are also included with LO accuracy (Figure 5.3b). Parton showers are

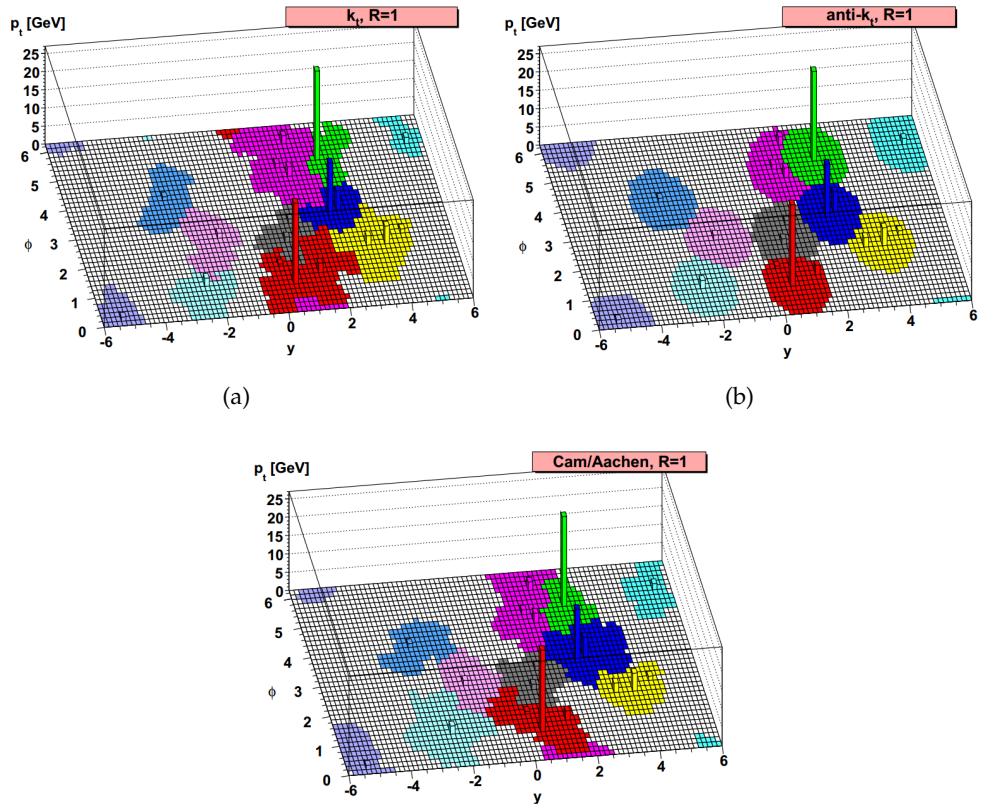

(a) (b)

(c)

Figure 5.1.: Shapes of reconstructed jets with $R = 1.0$ using the following algorithms: (a) k_T, (b) anti-k_T and (c) C/A. The figure is taken from [65]. Anti-k_T jets are noticeably the most regular in shape. The used events, generated with the Herwig event generator, are at generator-level. At this level the partons produced by the generator are used.

then applied as before (Figure 5.3c), along with the usual hadronisation and underlying event models.

5.3. Additional jet measurement

In this thesis normalised differential cross-sections of additional jets in $t\bar{t}$ events for the centre-of-mass energy of 13 TeV are presented. A Bayesian unfolding procedure is used that corrects the measured distributions to particle level. Details on the method are given in Section 9.3. The fiducial volume is defined in Section 9.1.
The normalised differential cross-sections are measured as a function of the jet multiplicity above a jet p_T threshold of 25, 40, 60 and 80 GeV, as well as a function of leading[1] b-jet and leading additional jet p_T. These results are published in Ref. [66].
Additionally, the cross-section as a function of the p_T sum of all objects in the event H_T is

[1] A leading object is an object with the largest transverse momentum in an event.

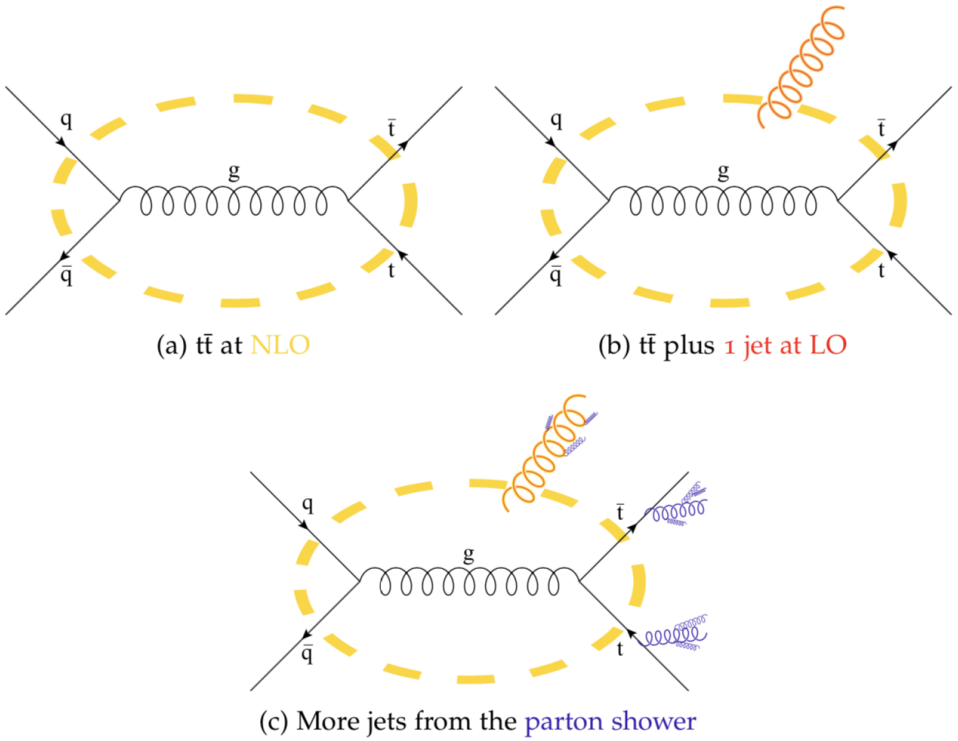

Figure 5.2.: Visualisation of $t\bar{t}$ events generated with the NLO accuracy, like MG5_aMC@NLO and Powheg. The dashed oval in (a) represents all virtual corrections to the leading order $t\bar{t}$ diagram. The external gluon shown in (b) represents the real emission corrections, which could be attached to any leg of the diagram enclosed by the loop. The cartoon in (c) shows the additional QCD radiation produced by the parton shower, which is typically softer than that produced by the matrix element.

determined in this thesis. H_T corresponds to the overall energy in the event, which is expected to change with gluon radiations, e.g. a jet originating from initial-state radiation might pass the event selection and therefore increase the overall energy of the event. Comparable to this approach, jet multiplicities are split into m_{llbb} regions. m_{llbb} is defined as the invariant mass of the selected two leptons and two b-jets from the top decay. A system with higher energy in the event (higher m_{llbb}) is expected to have more QCD radiations. For events with at least two additional jets, correlations between the two additional jets with the highest p_T are studied. The invariant mass of these jets m_{jj} is calculated and studied, because this will help in modelling $g \to jj$. The spatial correlations are studied by measuring $\Delta R(j,j)$ and $\Delta\phi(j,j)$.
Measurements similar to those presented in this thesis were performed by ATLAS at 7 TeV [2, 67] and have been used to tune parameters in Monte Carlo (MC) generators for LHC Run 2 [42, 68, 69]. In the lepton+jets channel, previous measurements of the inclusive jet multiplicity were done since it is difficult to distinguish jets originating in W decays from additional jets produced by QCD radiation. Recent measurements of jet multiplicity were performed in the single lepton channel by CMS at 13 TeV [6] and in the dilepton channel by ATLAS and CMS at 8 TeV [3, 5].

5.4. Analysis strategy

In general, three levels are available to compare distributions from data to theoretical predictions: detector, parton and particle level, which are shown in Figure 5.4. Mainly, two different approaches exist to compare theory to measured data:

- Use MC simulations and model the detector response in order to compare directly to the data measured by the respective experiment or
- Correct the measured data to the level at which they can be compared to a theoretical calculation, using the known detector response.

The first option, a comparison at detector level, requires folding theoretical predictions to detector level. The simulation of the detector response is applied to the MC sample; at the time the measurement is performed. Hence, if any improvements on the theoretical prediction are made, then the entire analysis needs to be applied again since the theoretical calculation is fully entangled with the detector response modelling. These repetitions are not feasible, from the experiments point of view. Also, any measurement at detector level depends on the actual experiment, like reconstruction efficiencies or energy resolutions. Therefore, it is not possible to compare the measurements of different experiments with each other.
In the second option, the measured data is unfolded to a detector independent level, which is either the parton level or the particle level (together called truth level in the following). A theoretical model has to be used to model the detector response, introducing a theory dependence on the data at the unfolded level. If the theory-dependence is strong, the same problem as for the first option occurs: theoretical and experimental modelling are so entangled that analysis has to be repeated, whenever improvements on the theoretical prediction are available. However, this dependence can be minimised by unfolding data to a well defined theoretically fiducial volume at generator level, which does not depend strongly on different underlying models. In general, a fiducial volume can be defined for different levels (parton or particle level) and different selection criteria. The fiducial phase should get defined similarly to the detector level selection criteria, which minimises extrapolation uncertainties from the detector level to the truth level.
For instance, at parton level measurements are compared to particles before hadronisation and top-quark decay, which describes elementary particles such as quarks and gluons not confined in hadrons. The unfolded procedure to parton level needs a theoretical model for showering and hadronisation, as well as a model for the interaction of stable particles with the detector. This usually introduces large physics modelling uncertainties, since the quark and gluon modelling depend on the technical details of the MC generators.
In the particle level approach, measurements are compared to particles with a relatively long lifetime. For ATLAS, particles with a mean lifetime $\tau > 300$ ps mm are considered. At the particle level, only the particle interaction with the detector has to be assumed. Thus measurements at particle level depend less on theoretical predictions than at parton level because the unfolding is independent of the technical details of MC generators.

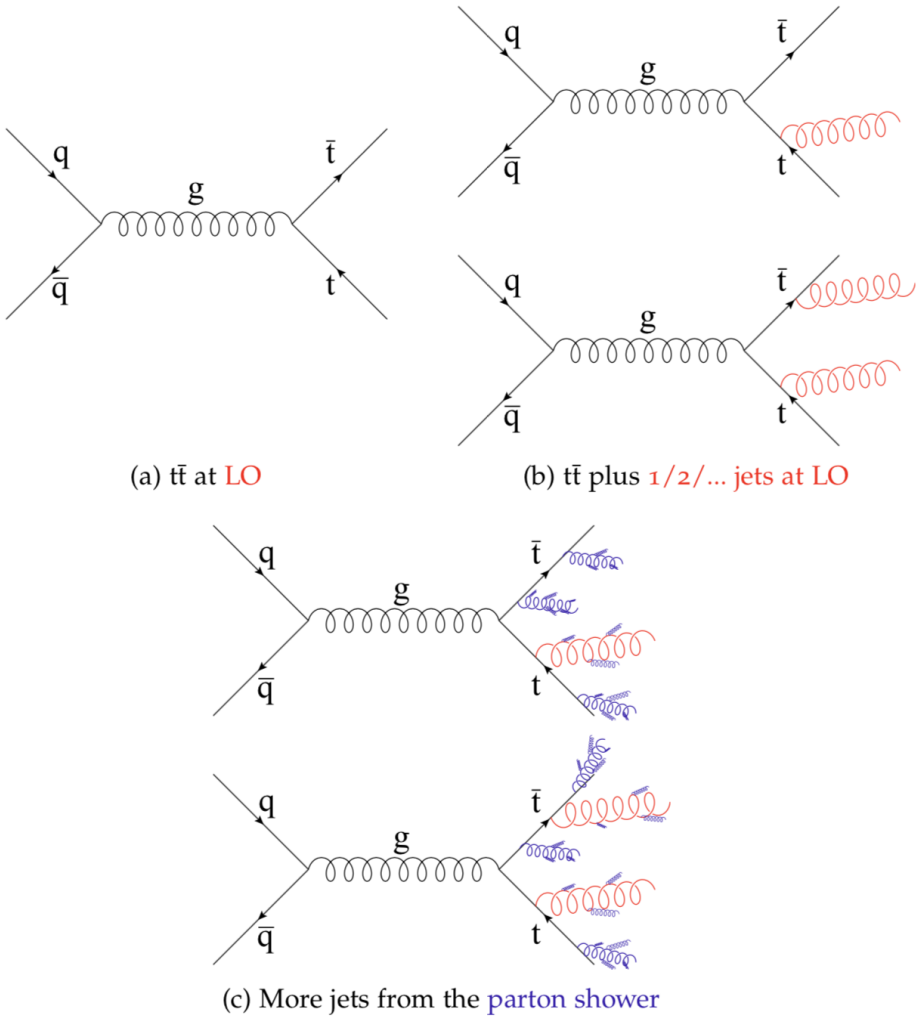

Figure 5.3.: Visualisation of the physics included in $t\bar{t}$ events generated with the multi-leg LO MCs like Sherpa. The external gluons shown in (b) represent the additional partons in the final state as part of the LO calculation. In (c) additional QCD radiation produced by the parton shower is shown.

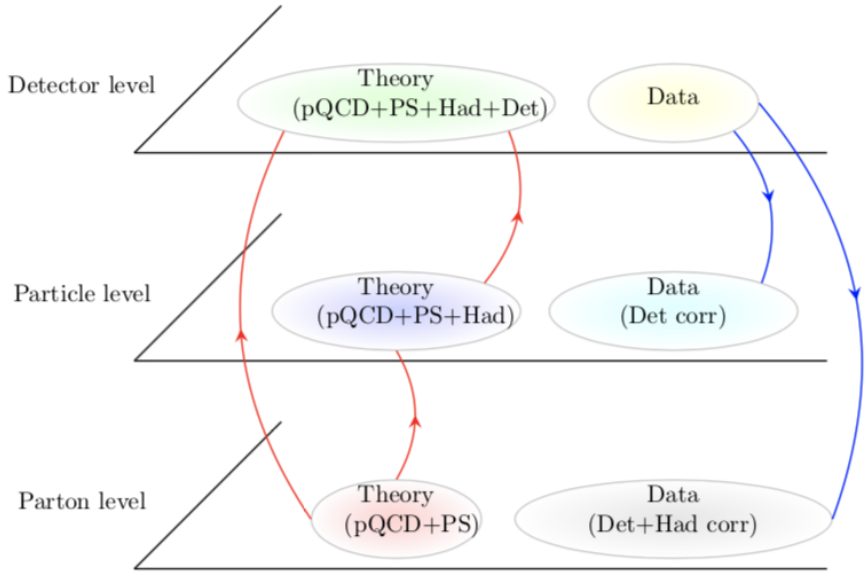

Figure 5.4.: Detector, parton and particle level visualisation. Comparison between data and theory can be performed either by folding theoretical predictions to detector level or by unfolding data to the level where theoretical calculation has been defined. Folding is represented by red lines while unfolding by blue ones. Ellipses represent the fiducial volumes defined for each level phase space.

6. Data collection and MC simulations

The data used in this thesis was collected during the 2015 LHC $p-p$ run at $\sqrt{s} = 13\,\text{TeV}$ with 25ns bunch spacing. The total integrated luminosity after applying data-quality assessment criteria based on beam, detector and data-taking quality was $\mathcal{L}$ = 3.2 fb^{-1}. The cumulative luminosity recorded in 2015 is shown in Figure 6.1.
Table 6.1 summarises the nominal LHC design parameters as well as the values achieved in the run period in 2015.

6.1. Pile-up

Each hard scattering event (the event of interest) at LHC can be overlayed by simultaneous interactions leading to multiple $p-p$ interactions happening at the same time, which is called pile-up. Two observables quantify the impact of pile-up. The average number of interactions per bunch crossing, μ, is shown in Figure 6.2. The average number of $p-p$ interactions per bunch crossing ranged from approximately 5 to 25, with a mean of 13.7.
Pile-up presents a significant challenge since it can rapidly increase the combinatoric complexity of reconstructing events and degrade the performance of the reconstruction algorithms. In measurements involving jets, it randomly adds energy deposits to calorimeter cells, and hence it degrades the reconstruction of the jets from the hard scattering event. Each $t\bar{t}$ pair event consists of several jets, and thereby the $t\bar{t}$ pair events are highly affected by pile-up. Mitigation of pile-up effects is necessary to obtain better response and resolution for the jet 4-momentum using a pile-up subtraction method. Another negative effect of pile-up is the occurrence of additional jets (pile-up jets) in the event, i.e. jets not originating from the hard scattering event, but mainly from pile-up. The influence of these jets to the measurement in this thesis is studied in Section 8.2.3.

Parameter	Design value	2015
Energy [TeV]	7	6.5
Bunch spacing [ns]	25	25
RMS bunch length [cm]	7.55	10
Average bunch intensity [10^{11} p/bunch]	1.15	1.15
Bunches per LHC injection	288 (4×72)	144 (4×36)
Total number of bunches	2748 (2808 in DR)	2244
Transverse emittance at IP [μm]	3.75	3.5
β^* at IP [cm]	55	80
Peak luminosity [$10^{34}\text{cm}^{-2}\text{s}^{-1}$]	~ 0.99	~ 0.5

Table 6.1.: LHC detector parameters. Both the design parameters and the actual parameters used during the 2015 data taking are listed.

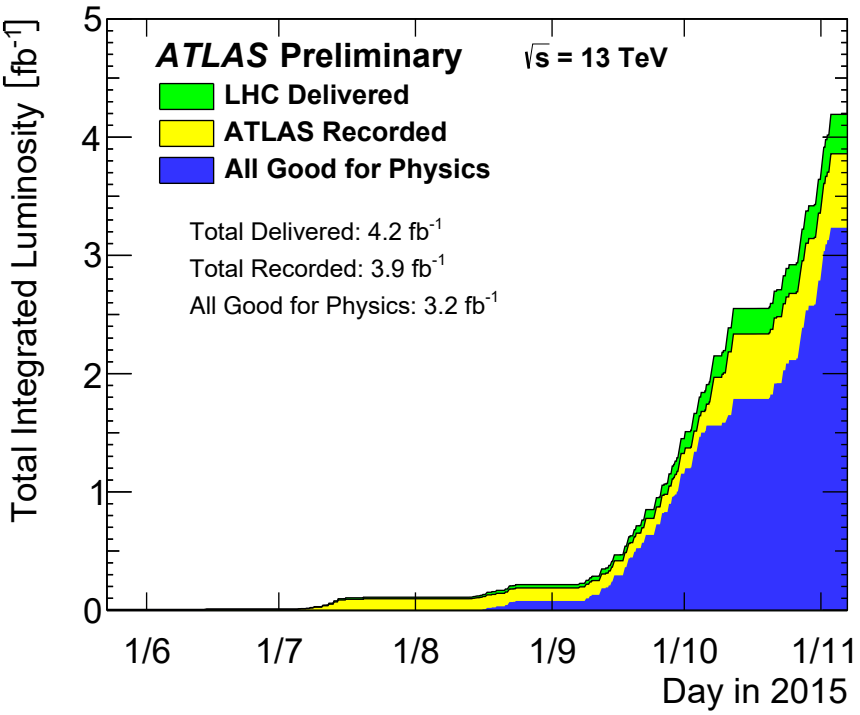

Figure 6.1.: Cumulative luminosity versus time delivered to ATLAS (green), recorded by ATLAS (yellow), and certified to be good quality data (blue) during stable beams for $p-p$ collisions at $\sqrt{s} = 13\,\text{TeV}$ in 2015.

6.1.1. Pile-up simulation

Multiple additional $p-p$ collisions were simulated with the soft QCD processes, that are precisely measured at the beginning of every data taking period. This measurement is called Minimum Bias analysis, which is presented in Section 4.3. The measured distributions help to tune the MC generators that simulate soft QCD processes.
In this thesis Pythia8.186 [29] is used with parameter values from tune A2 [70] and the MSTW2008LO [71] set of parton distribution functions (PDFs) in order to simulate pile-up by overlaying these events onto the hard scattering event. The number of additional $p-p$ collisions was generated randomly according to the expected μ for 2015 data. In the analysis, an event weight is applied to adjust the μ distribution to what was measured in 2015 (Figure 6.2).

6.2. Trigger

Limitations in disk space, computing power and write-out speed require a particular data recording. Therefore collision events are filtered to record only those of physics interest. In Run 2, the trigger system consists of two steps of event selection:

Level 1 (L1) is an online hardware trigger that has coarse granularity, that looks at any measured signal from the calorimeters and muon system. Only the trigger chambers are read out to achieve the necessary speed with a defined multiplicity and above a certain energy threshold. The acceptance rate of L1 is 100000 events per second.

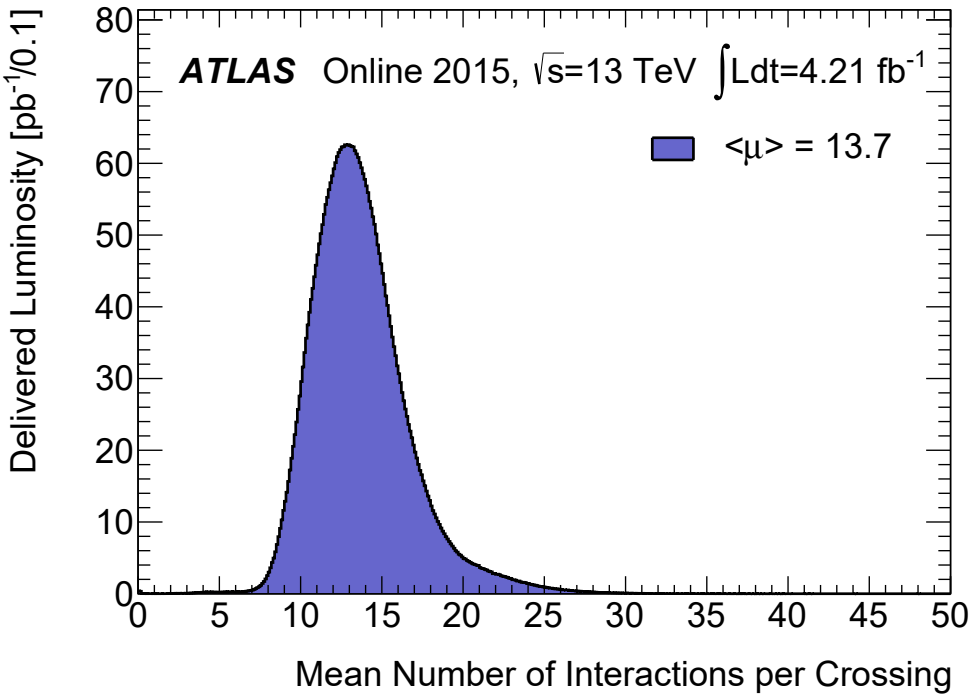

Figure 6.2.: Shown is the luminosity-weighted distribution of the mean number of interactions per crossing for the 2015 $p-p$ collision data at $\sqrt{s} = 13\,\text{TeV}$.

High-Level Trigger (HLT) is a software trigger that uses algorithms that are very similar to offline analysis software, with the constraint of processing time limits. It makes use of the full (non-reduced) granularity and precision of the calorimeter and muon chamber, and also incorporates tracking information from the inner detector. The HLT has a further reduced acceptance rate of 1 kHz.

In this analysis events were required to pass one trigger out of the following list of single electron or single muon trigger menus:

- HLT_e24_lhmedium_L1EM20VH
- HLT_e60_lhmedium
- HLT_e120_lhloose
- HLT_mu20_iloose_L1MU15
- HLT_mu50

The first three trigger menus refer to electrons with p_{T} thresholds of 24 GeV, 60 GeV and 120 GeV. The 'lhmedium'/'lhloose' quality criteria require that the electron pass at HLT the likelihood-based electron selection criteria 'medium'/'loose' [72]. All three electron triggers are seeded by the L1 trigger 'L1EM20VH', which refers to the electromagnetic trigger with an energy threshold of 20 GeV. The additional quality requirement 'V' denotes that the trigger threshold is varied as a function of the pseudorapidity to correct for the different amount

of material before the calorimeter, while 'H' ensures a small energy deposit in the hadronic calorimeter behind the electromagnetic cluster of the electron candidate relative to the electromagnetic cluster energy.
The last two triggers refer to muons with p_{T} thresholds of 20 GeV and 50 GeV. 'HLT_mu20iloose_L1MU15' is the lowest unprescaled single muon trigger for the 2015 data. It selects events containing at least one muon which has a p_{T} at L1 greater than 15 GeV and at HLT greater than 20 GeV and a loose track isolation requirement ('iloose') [73]. The 'HLT_mu50_iloose' trigger is seeded with the 'L1MU20' trigger and is required to satisfy the 50 GeV.

6.3. Corrections of the Monte Carlo Simulation

Simulations are never perfect, and there will always be differences between the performance in MC simulation and data. These differences are corrected in MC using inputs from various calibration measurements [74]. The corrections used are outlined in the following Chapter 7.
In order to correct efficiency differences between data and MC, a global event scale factor is applied, which is based on the data to MC ratio for the corresponding efficiency measurement. All individual scale factors are multiplied to get the global scale factor that is used to weight the event. By applying the event weight for each event, the reconstruction, identification and trigger efficiencies of various objects can be corrected. With an event scale factor, also the b-tagging performance can be corrected.
Also, the 4-momenta and the resolution of reconstructed objects in MC simulations are adapted to the performance in data events by applying corrections on the object metrics itself.
Each correction has its associated uncertainties that are propagated to the final physics results.

7. Object reconstruction at ATLAS

In this analysis, the top quarks created in the $p-p$ collisions are decaying leptonically ($t \to Wb \to l\nu b$). One top is required to have an electron in the final state, while the other is required to have a muon. Therefore it is necessary to identify the leptons and b quarks as objects from signals in the detector. The object reconstruction relies on some basic objects explained in Section 7.1. The reconstruction, efficiency and calibration of jets (Section 7.2), electrons and muons (Section 7.3) used at the ATLAS experiment are reviewed.

7.1. Basic objects

Physical objects, like electrons, muons and jets, are reconstructed by using the basic objects: tracks, vertices and clusters, which are described in the following.

7.1.1. Track reconstruction

All charged particles from the $p-p$ collisions leave energy depositions in the sub-detectors of the ID. Each silicon cell (pixel or strip) with energy above a certain threshold is called hit. Connected cells on a detector module are combined into clusters. For pixel detector measurement each cluster directly leads to a three-dimensional space-point object, which is later used to form track seeds. For SCT measurement the space-points are created by using the sandwich structure together with a beam spot constraint. The track reconstruction algorithm used at ATLAS [75] consists of two separate sequences, finding tracks from the inside of the detector outward (inside-out algorithm) and vice versa (outside-in algorithm).

Inside-out tracking The inside-out method is useful to reconstruct charged particles from the hard process, which are either directly produced in $p-p$ interactions or result from subsequent decays of intermediate particles[2].
Track candidates are built from space-points via pattern recognition. In the second step, ambiguities due to fake tracks or overlapping track segments with shared hits are resolved by finding the best track collection with a scoring schema. After extending tracks to the TRT, tracks are refitted using the information from all three ID sub-detectors in a final step.

Outside-in tracking In order to increase the overall tracking efficiency, a reverse tracking technique, called outside-in, is deployed. For the inside-out tracking it is difficult to handle the large density of hits near the beam pipe. The ambiguity solver can eliminate tracks. Furthermore, secondary particles not originating directly from the IP, like from kaon and lambda decays or photon conversions, may not have enough hits in the silicon detector.
The outside-in tracking algorithm is starting with global pattern recognition in the TRT. The found TRT segments are then extended to the silicon detector (backtracking).

[2]Particles produced from decays of particles with $\tau > 30$ ps are called secondary particles.

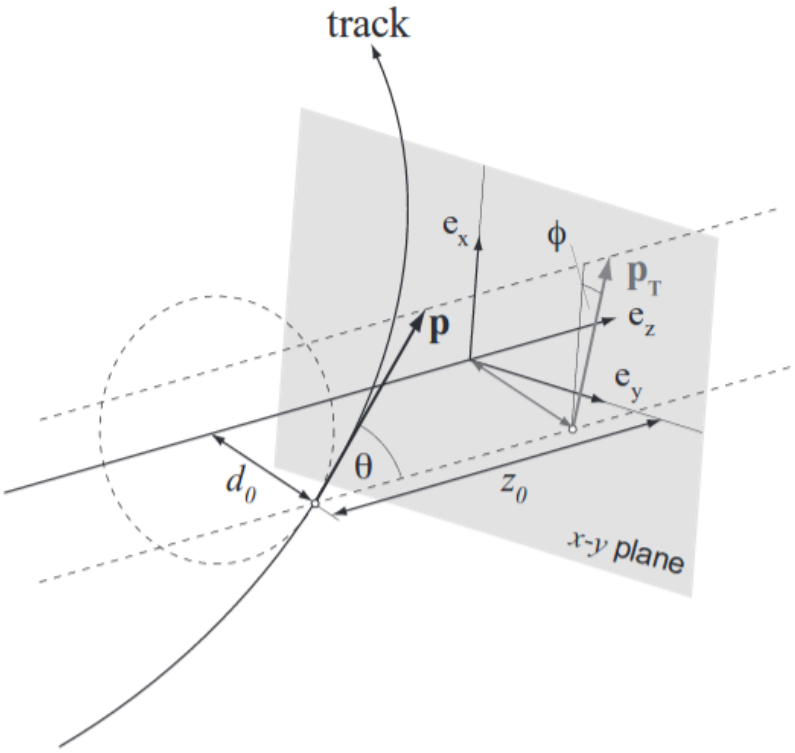

Figure 7.1.: Visualisation of track parameters [76]

Track parameterization Since the magnetic field bends charged particle tracks, the trajectory takes a helical form and can be expressed by five parameters, which are visualised in Figure 7.1:

d_0 - the transverse impact parameter, equal to the distance of closest approach in the plane transverse to the beam of the track to the primary vertex,

z_0 - the longitudinal impact parameter, equal to the z coordinate of the point of closest approach in $r - \phi$ to the primary vertex,

ϕ - the azimuthal angle of the trajectory at the point of closest approach to the primary vertex in,

θ - the polar angle formed by the track with respect to the beam and

q/p_T - the charge divided by the transverse momentum of the track.

7.1.2. Vertex reconstruction

Vertices are reconstructed using iterative vertex finding algorithm and vertex fitting, that is divided into three major steps - seeding, track assignment, and fitting [77]:

1. The impact parameters z_0 of all tracks with respect to the centre of the beam spot are used to produce a single seed at the location of the estimated mode in z, using an iterative method to find the most likely value.

2. Tracks compatible with the seed are grouped for fitting.

3. The adaptive vertex fitting algorithm is used to estimate the position and uncertainty of the vertex.

4. Incompatible tracks that are not used in a previous vertex are used to repeat the procedure starting from the creation of a new seed.

Since several $p-p$ collisions are likely to occur for each bunch crossing, some of the tracks will be associated with secondary vertices from pile-up rather than the primary vertex (PV) from the hard collision. The PV is conventionally defined as the vertex with the highest track ${p_{\mathrm{T}}}^2$ sum.

7.2. Jets

All particles produced by the outgoing quarks and gluons from the hard-scattering collision deposit their energy in many cells travelling through the calorimeter. The four-momenta of these energy depositions are grouped into topological clusters or topo-clusters [78], which are then used input parameters for an anti-$\mathrm{k_T}$ jet algorithm [63, 57] with $R = 0.4$ (see Section 5.1).
The topological clustering algorithm uses all calorimeter cells, which have significant energy compared to the expected noise. The seed cell is required to have at least four times the noise threshold, where the noise calculated for each cell as the sum of electronic noise and pile-up induced noise. Neighbouring cells with at least two times the noise threshold are iteratively added to the seed cell. In the last step, an extra layer of cells with measured deposited energy on the perimeter of the clustered cells are added. In the end, a cluster is formed by all connected cells.
The topological clusters are reconstructed at the so-called electromagnetic energy scale (EM), which corresponds to the energy deposited by particles in an electromagnetic shower in the calorimeter. The EM scale is established by calibrating the calorimeter electronic signals to the energies of electrons using test beam measurements of electrons in the barrel and endcap calorimeters [79].
The resulting measured jet energy at EM scale is lower compared to real deposited energy due to the following effects:

- Calorimeter non-compensation - energy deposited by hadrons is only partially contained
- Inactive or dead material - part of the energy is lost because of inactive material, cracks and gaps in the detector
- Outside jet cone - low energy charged particles will bend outside the jet cone due to the solenoidal magnetic field
- Leakage - energy lost due to showers that are not fully contained in the calorimeter

To correct for these effects the jet energy calibration is relating the measured jet energy to the energy of the corresponding reference jets in Monte Carlo simulations (truth jets)[1]. It is worth mentioning that there is an alternative cluster calibration available at ATLAS: the local cell signal weighting (LCW), which was mainly used at 7 and 8 TeV [79]. This calibration reduces

[1] Truth jets are built from generated stable particles using the same jet algorithm (without detector simulation).

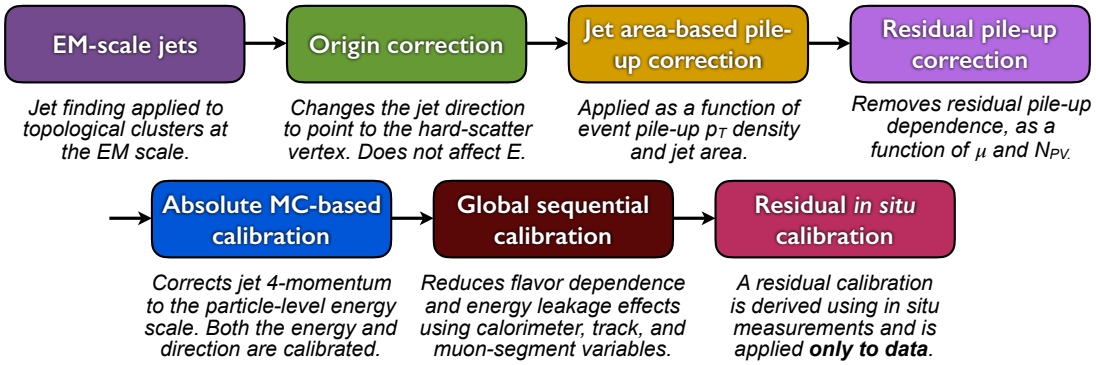

Figure 7.2.: The calibration steps applied to correct the energy of jets [81].

energy fluctuations due to the non-compensation of the hadronic calorimeter.
In this thesis jets reconstructed with the anti-k_T algorithm (R = 0.4) within the fiducial region $p_T > 25$ GeV and $|\eta| < 2.5$ are used. The transverse momentum criteria are applied to reject jets from underlying events. In the following the jet calibration and energy resolution are described (Section 7.2.1 and 7.2.3). Furthermore the suppression of jets reconstructed from pile-up and the association to b-Hadrons is explained in Section 7.2.4 and 7.2.5. More details about the jet reconstruction can be found in [66, 80].

7.2.1. Jet calibration

The jet reconstruction is corrected to the initial parton kinematics by a series of corrections, which are derived from both the MC simulation and from data, with the latter referred to as in-situ corrections [81]. The full correction procedure is visualized in Figure 7.2.

7.2.1.1. Origin correction

The origin of a jet is corrected to point back to the hard-scatter interaction point rather than the centre of the detector [82]. The jet four-vector is modified such that the energy is unchanged, but the direction originates from the primary vertex. This improves the η resolution of jets as shown in Figure 7.3.

7.2.1.2. Pile-up correction

The diffuse background from pile-up is subtracted from the energy of jets by two corrections [81]. First, an area-based pile-up contribution is subtracted utilising the average energy density ρ in $\eta \times \phi$ space and the jet area A obtained by ghost matching [83]. A second correction is applied to remove any residual in-time and out-of-time pile-up effects, which is illustrated in Figure 7.4. The corrected transverse momentum of the jet is defined by:

$$p_T^{\text{corr}} = p_T^{\text{EM}} - \rho \times A - \alpha \times (N_{PV} - 1) - \beta \times \langle \mu \rangle \tag{7.1}$$

where p_T^{EM} is the initial transverse momentum of the jet at EM scale. The in-time pile-up correction depends on the parameter α and the number of primary vertices N_{PV}, while the out-of-time pile-up depends on β and the average number of interactions per bunch crossing $\langle \mu \rangle$.

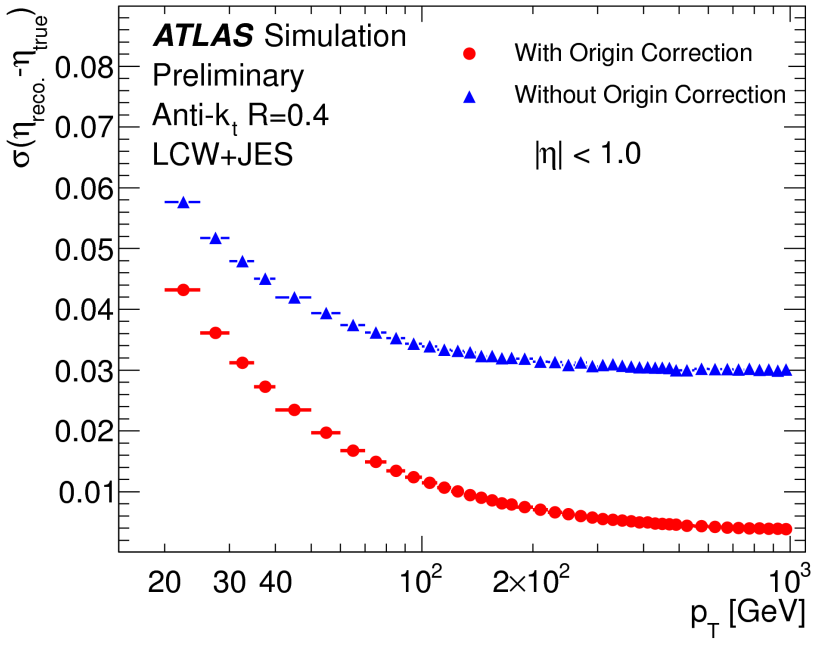

Figure 7.3.: The effect of the origin correction on the η resolution for data taken in Run-1 [82]. In this study the origin of LCW jets is corrected. Similar results are obtained for EM jets.

7.2.1.3. Jet energy response and η correction

The jet energy scale (JES) calibration is derived from simulation to correct the EM scale jets to the generated jet energy [81]. The jet energy response is derived from isolated jets from an inclusive dijet MC simulation after applying origin and pile-up corrections by comparing the jet energies of reconstructed jets with their corresponding geometrically matched truth jets. The average jet energy response parameterized in detector pseudorapidity η_{det} is shown in Figure 7.5(a), which is the inverse of the jet calibration factor. The detector pseudorapidity is useful when deriving average corrections that depend on detector geometry. A lower energy response is a result of an absorbed or undetected particle in detector gaps and transitions between sub-detectors.
After applying the JES correction a bias in the reconstructed η direction of the jets is found in certain η_{det} regions, shown in Figure 7.5(b). These regions correspond to the before mentioned gaps and transitions in the detector. Therefore an additional correction is used to reduce this bias and consequentially improve the closure of energy scale correction.
Since the jet energy scale calibration is derived in inclusive dijets events, a mixture of quark and gluon jets in the sample is presented. The jet response for individual quark or gluon which initiate jets is different due to the differences in jet fragmentation and particle composition. The different response leads to an effect known as *flavor-dependence* of the jet response and is a major source of the JES systematic uncertainty.

7.2.1.4. Global sequential calibration

The global sequential calibrations (GSCs) [84] make use of the topology of the energy deposits in the calorimeter and tracking information associated to the jet in order to reduce the difference

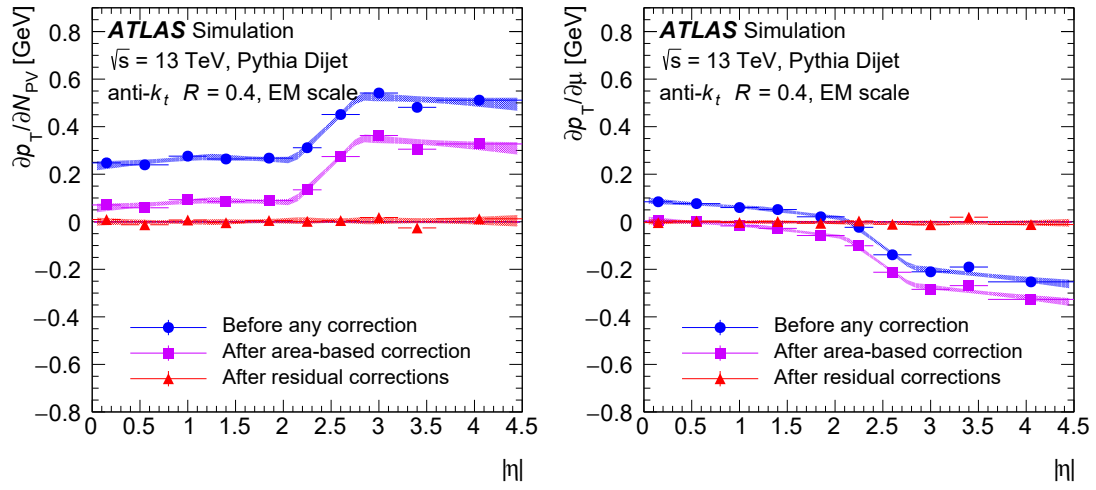

(a) (b)

Figure 7.4.: Removal of the residual pile-up effects on the jet p_{T} achieved by this each correction step. (a) shows the in-time pile-up subtraction and (b) the out-of-time pile-up subtraction [81].

in response between quark and gluon jets. Also, the GSCs exploit information related to the activity in the muon chambers behind a jet to correct jet energies of high-p_{T} jets which are not fully contained in the calorimeter (*punch-through* jets). These corrections are applied to improve energy response of individual jets while maintaining the mean energy response derived in the previous jet energy scale calibration.

7.2.1.5. In-situ jet energy calibration

The calibrations based on MC simulation are correcting the jets at EM scale to the energy scale at particle level, but may suffer from MC mismodeling. Any differences of the jet energy between data and simulation are removed by a residual *in-situ* calibration applied to the data only [82, 81]. The jet p_{T} is corrected by multiplying the response ratio:

$$\frac{\mathrm{Response}_{\mathrm{Data}}}{\mathrm{Response}_{\mathrm{MC}}} = \frac{\langle p_{\mathrm{T}}^{\mathrm{jet}} / p_{\mathrm{T}}^{\mathrm{ref}} \rangle_{\mathrm{Data}}}{\langle p_{\mathrm{T}}^{\mathrm{jet}} / p_{\mathrm{T}}^{\mathrm{ref}} \rangle_{\mathrm{MC}}}, \tag{7.2}$$

where the response is derived from transverse momentum balance between jet and a well measured object, called reference object. A large kinematic phase space is covered by applying a sequence of corrections using several reference objects (photons, Z bosons and other jets) while for each reference object the response ratio is estimated.
In the first step dijet events are employed to estimate an η-intercalibration in which the response of forward jets ($0.8 < |\eta| < 4.5$) with respect to well-modeled central jets ($|\eta| < 0.8$) is corrected. In this step non-uniformities due to mismodelled dead material and calorimeter response are corrected.
In the second step photons and Z bosons, decaying into ee or $\mu\mu$, are used as the reference object to calibrate jets with p_{T} up to 950 GeV in the central region $|\eta| < 0.8$.

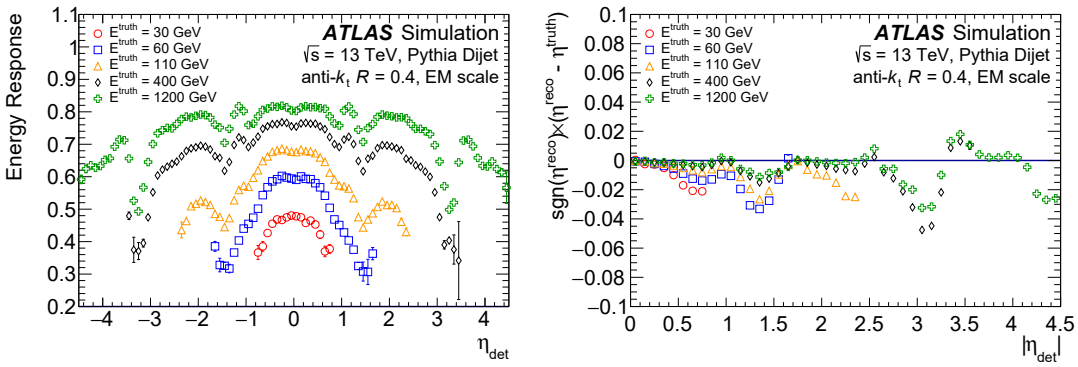

(a) (b)

Figure 7.5.: Jet energy response (a) and bias in the jet η reconstruction (b) as a function of η_{det} before JES correction [81].

In the last step, central jets ($|\eta| < 1.2$) up to 2 TeV are calibrated. In multijet events, these high p_{T} jets are recoiling against lower p_{T} jets, which are used as reference object since they are already well calibrated by the previous steps. The combination of all steps is shown in Figure 7.6. The difference between data and MC measured in these final calibrations is typically 1-4%.

7.2.2. Jet energy scale uncertainties

The uncertainties corresponding to the jet energy scale are expected to be amongst the leading ones for this thesis since it measures the jet activity in top events. Detailed descriptions of the JES uncertainties are provided in [81] and recommendations from the JetEtmiss performance group are provided in [81, 85]. A summary of the uncertainties is provided in the following.
The jet energy scale uncertainty consists of more than 67 nuisance parameters. The majority of these uncertainties are associated with the residual in situ correction; taking into account MC modelling uncertainties, the statistical uncertainty on the samples used to derive the correction, and the uncertainties from the reference objects balanced against the jet. Additional uncertainties are from the flavour composition (fraction of gluons and light quarks in the sample), the response to these objects, pile-up uncertainties, and the jet punch-through uncertainty. All uncertainties from individual calibrations are propagated to a final calibration. Figure 7.7 shows the jet energy scale uncertainty as a function of jet (a) p_{T} and (b) η. Note that *Absolute in situ JES* refers to the Z/γ-jet balance and multi-jet balance calibrations, and account for assumptions made in the event topology, MC simulation, sample statistics, and propagated uncertainties of the electron, muon, and photon energy scales. *Relative in situ JES* refers to the η-intercalibration, that corresponds to potential physics mismodelling, statistical uncertainties and a non-closure of the correction observed in the $2.0 < |\eta| < 2.6$ region. *Flavour response and composition* corresponds to differences in the calorimeter response and simulated jet composition of light-quark, b-quark, and gluon initiated jets. *Pile-up* uncertainties account for potential mismodelling of the number of primary vertices (N_{PV}), the number of interactions per bunch crossing μ, the average energy density ρ and the residual p_{T} dependence of the pile-up correction. One uncertainty is considered for the GSC *punch-through* correction.
The total uncertainties, shown in Figure 7.7a, ranges from 4 % for jets with $p_{\text{T}} = 25$ GeV, down to 1.5 % for 100 GeV jets and up to 2.5% for 2.5 TeV jets.

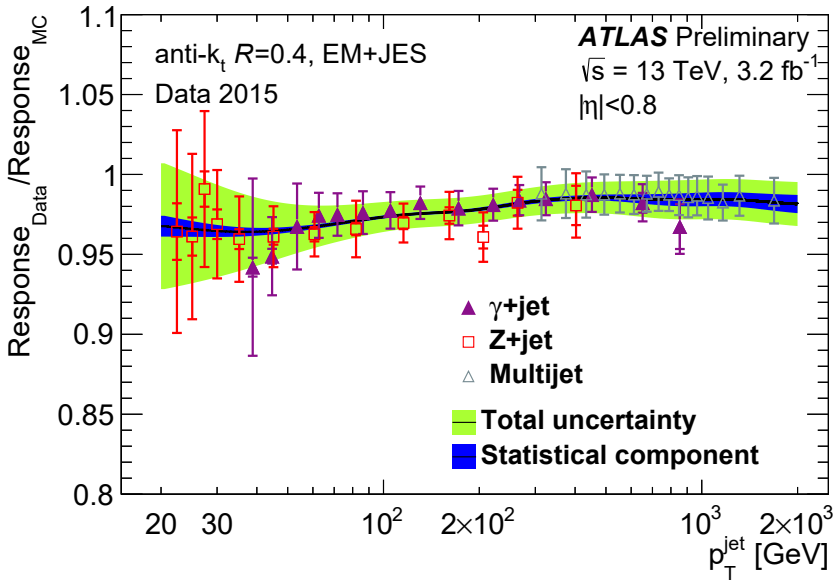

Figure 7.6.: Jet response ratio of the data to the MC simulation as a function of p_{T} for the three in-situ techniques combined to determine the in-situ energy scale correction. The green band indicates the total uncertainty resulting from the combination of in-situ techniques, while the inner band shows the fraction purely from statistical uncertainties [81].

The propagation of 67 nuisance parameters in an analysis would be extremely time consuming, and in many cases, the loss of correlation information caused by combining nuisance parameters has a negligible effect on the results of the analysis. Therefore this analysis uses a reduced set of 19 nuisance parameters (NPs) obtained by global reduction [86], which is performed through an eigen-decomposition of the 67 uncertainties from the in situ calibrations. The most significant components are kept separate, and the remaining components are quadratically combined into a single NP. The reduction procedure preserves to a percent-level the correlations across jet p_{T} and η.

7.2.3. Jet energy resolution

The jet energy resolution (JER) is another important quantity for the spread of the measured jet energies with respect to their true value, indicating how precisely the jet energy can be measured. The determination of the JER is a multi-stage process, which is described in full in [82].
Similarly to the above described residual in situ calibration, the JER determination is done by using the p_{T} balance of objects in dijet events and Z/γ+jets events to obtain the p_{T} response distributions. After applying a Gaussian fit to the obtained p_{T} response distributions, the ratio between the root means square of the fit $\sigma(p_T)$ and the mean value $\langle p_T \rangle$ is determined. The obtained JER as a function of jet p_{T} is shown in Figure 7.8.
The uncertainty is largest at low p_{T} due to the uncertainties on noise contributions and the extrapolation uncertainty. Since the extrapolation uncertainty is dominant, the JER nuisance parameters were combined to form a single nuisance parameter (part of the 19 NPs mentioned above).

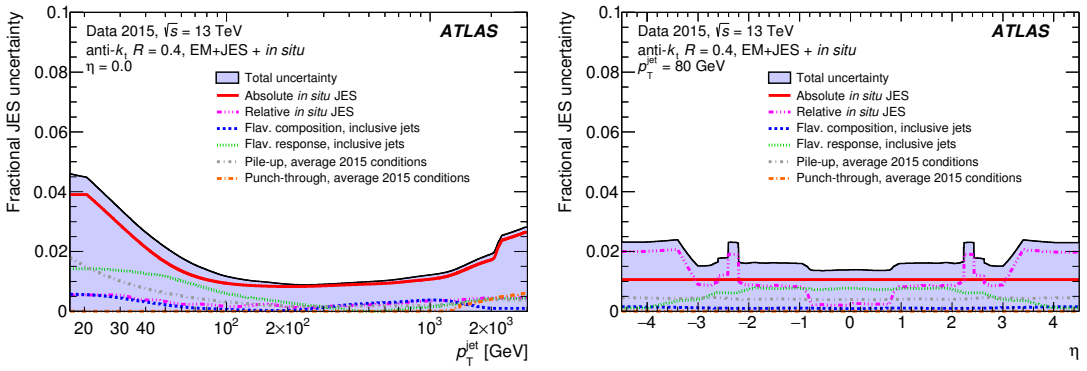

(a) (b)

Figure 7.7.: Final jet energy scale uncertainties as a function of jet p_{T} for jets of $\eta = 0$ and (b) jet η for jet p_{T} of 40 GeV. [81].

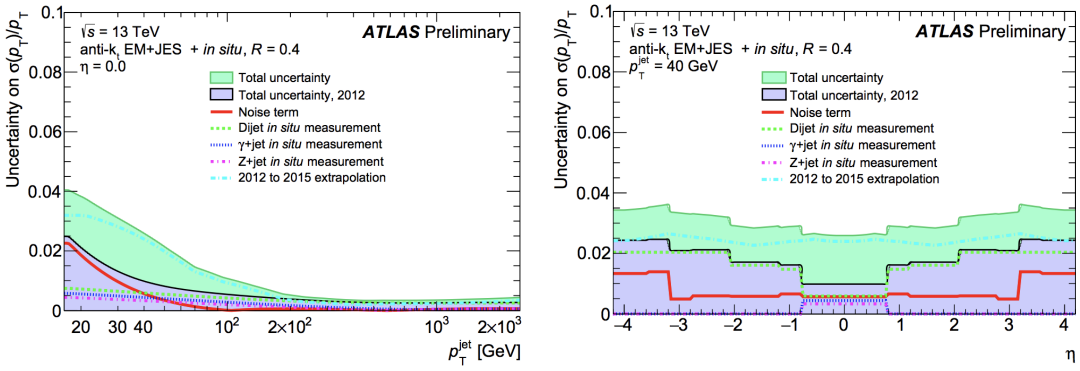

(a) (b)

Figure 7.8.: Final jet energy resolution uncertainties as a function of jet p_{T} for jets of $\eta = 0$ (a) and as a function of η for jet p_{T} of 40 GeV (b) [81].

7.2.4. Suppression of pile-up jets

Jets originating from pile-up are rejected by the jet vertex tagger (JVT), which is a two-dimensional likelihood method based on the observables R_{p_T} and corrJVF [87]. The variable R_{p_T} is defined as the scalar sum of the p_{T} of the tracks that are associated with the jet and originate from the hard-scatter vertex divided by the fully calibrated jet (including pile-up subtraction). The corrected jet vertex fraction (corrJVF) is the ratio of the same scalar sum of the p_{T} of the tracks that are associated with the jet and originate from the hard-scatter vertex to the scalar sum of p_{T} of all matched tracks in the jet, independently of their origin. Both observables can identify pile-up vertices and therefore distinguish between pile-up jets and jets from the hard scattering process, which is shown in Figure 7.9.
In this analysis jets with $p_{\mathrm{T}} < 60$ GeV and $|\eta| < 2.4$ are rejected using the JVT algorithm with a working point of 0.59. This JVT working point has an average efficiency of 92%[1].

[1]The JVT working points have been evaluated by selecting a sample of Z boson events decaying into muons with at least one extra jet.

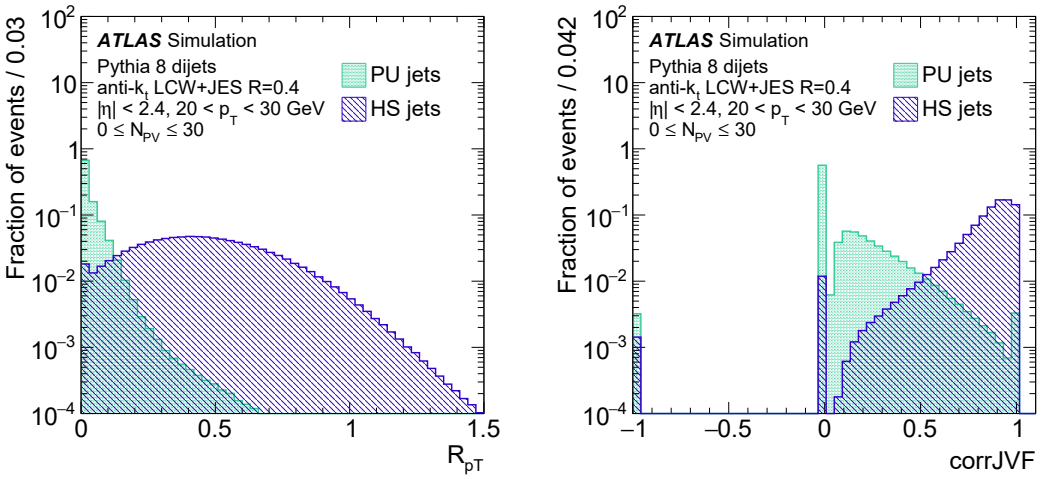

(a) (b)

Figure 7.9.: Distribution of corrJVF and R_{p_T} for pile-up (PU) and hard-scatter (HS) jets with 20 $< p_{\mathrm{T}} <$ 30GeV and $|\eta| < 2.4$ [87].

7.2.5. Association of jets to b-Hadrons

Top quarks are dominantly decaying into a W boson and a b quark. It is crucial to identify jets originated from b quarks to isolate events containing top quarks from lighter quarks. Algorithms to identify these jets, called b-tagging algorithms, are using the long lifetime of hadrons containing b quarks, large b-hadron mass and large branching ratio into leptons. The difference of b from light quark jets is mainly the relatively long lifetime of b-flavoured hadrons, which results in a secondary vertex because these hadrons are flying a significant length before they decay. In the end, this long lifetime leads to measurable impact parameters of the decay products. The ATLAS experiment utilises three distinct basic b-tagging algorithms, which are all described in [88]:

1. Impact parameter based algorithm,
2. Inclusive secondary vertex reconstruction algorithm and
3. Decay chain multi-vertex reconstruction algorithm.

They use impact parameters, invariant mass and multiplicity of tracks associated to jets as well as secondary vertex information.
In this analysis a multivariate algorithm, called MV2c20 [88], is used, that combines the input variables obtained from the three basic algorithms by using a boosted decision tree (BDT) algorithm to discriminate b-jets from light (u, d, s-quark or gluon jets) and c-jets. The training set consists of approximately 5 million $\mathrm{t\bar{t}}$ events. The MV2c20 algorithm is defined as the output of a BDT that gives a good trade-off between light- and c-jet rejection.
The working point of the MV2c20 tagger is chosen such that b-jets can be identified with an average 77 % b-tagging efficiency. The efficiency to tag b, c and light-flavour jets for the MV2c20 tagger for this operating point is shown in Figure 7.10. The tagging algorithm gives a rejection factor of about 130 against jets from light quark or gluon jets (light jets) and about 4.5 against

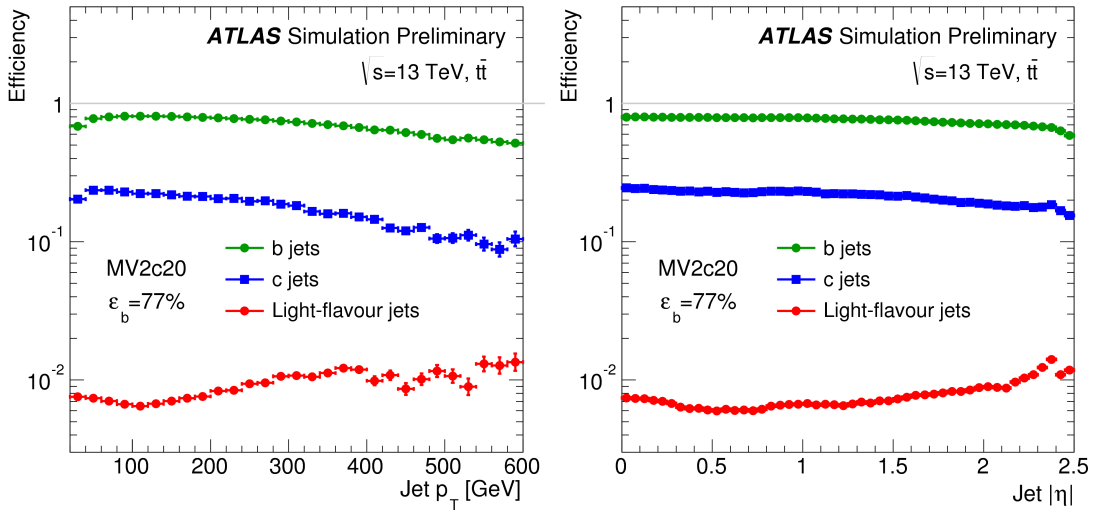

Figure 7.10.: The efficiency to tag b (green), c (blue) and light-flavour (red) jets for the MV2c20 tagger with the 77% operating point. Efficiencies are shown as a function of the jet p_T (a) and $|\eta|$ (b) [88].

jets originating from charm quarks (c-jets). With the addition of the IBL pixel detector the b-tagging efficiency has been boosted in Run-2 compared to Run-1 by around 10 % for a similar rejection of c- and light jets.
The b-tagging efficiencies can differ in data and simulation. Therefore a scale factor to calibrate the flavour tagging is used as described in [89]. The scale factor is multiplied to the event weight for each MC simulation, which ensures that the overall b-tagging performance will be the same in MC as in data.

7.3. Leptons

The lepton reconstruction is critical in this analysis because it allows us to distinguish between $t\bar{t}$ events and background events (see 3.2.2. In the following, the electron and muon reconstruction are described.

7.3.1. Electrons

The reconstruction of electrons is seeded by clusters in the electromagnetic calorimeter. A sliding-window algorithm with a size of 3 x 7 cells (area of size $\Delta\eta \times \Delta\phi$ = 0.075 x 0.175) in the barrel and 5 x 5 (area of size $\Delta\eta \times \Delta\phi$ = 0.125 x 0.125) in the end-caps is used to find clusters. The clusters are then matched to a track in the Inner Detector. The tracks, which are corrected for Bremsstrahlung effects, are required to have a minimum number of hits in the pixel and overall silicon layers to reduce photon contributions. Also, the impact parameter of the track has to be close to the primary vertex. This criterion rejects electrons from secondary processes. The energy of the electron candidate is determined by the cluster energy, while the position is defined by the track. More details about the electron reconstruction can be found in [66, 90].
All electron candidates must pass an identification likelihood-based (LH) algorithm with *medium*

quality [91]. It is based on the shower shape in the electromagnetic calori-meters and on the transition radiation observed in the TRT detector. With a multivariate analysis (MVA) technique the LH method evaluates probabilities for the object to be signal or background such as hadronic jets, photon conversions or electrons from heavy flavour hadron decays. It uses signal and background probability density functions (PDFs) of several discriminating variables, e.g. track quality, shower shape in the electromagnetic calorimeters and on the transition radiation observed in the TRT detector. More details are given in [91]. Also, electrons are required to have a transverse momentum $p_{\mathrm{T}} > 25$ GeV, which is slightly above the electron trigger. The pseudorapidity of the cluster is restricted to $|\eta_{\mathrm{cluster}}| < 2.47$ due to detector acceptance, while electron candidates are excluded if the energy cluster is within the transition region between the barrel and the end-cap of the electromagnetic calorimeter, $1.37 < |\eta_{\mathrm{cluster}}| < 1.52$, called crack-region, where a large amount of material is in front of the calorimeter. To reduce background from conversions and secondary particles, Electrons must be compatible with the primary interaction vertex of the hard collision. Therefore they must satisfy requirements of transverse impact parameter significance[1] $|d_0^{\mathrm{sig}}| < 5$ and longitudinal impact parameter $|z_0 \sin\theta| < 0.5$ mm. In order to further reduce the contribution of electrons originating from converted photons produced in hadron decays, electrons from heavy flavour hadron decay, and misidentified electrons from light hadrons, electrons must pass a track isolation requirement using the *gradient* working point [91]. The isolation is based on the sum of transverse momenta of all ID tracks, satisfying quality requirements, inside a cone size of $\Delta R = \min(0.2, 10\ \mathrm{GeV}/p_{\mathrm{T}})$. The cone size is decreasing for increasing transverse momenta. The used isolation requirements result in a 90 (99)% efficiency for $p_{\mathrm{T}} = 25(60)\ GeV$ for $Z \to ee$ events [91].

7.3.2. Muons

The muon reconstruction utilises all information from the inner detector and muon spectrometer. First, tracks are independently reconstructed in each sub-detector. The hits are then combined by a global refit to form a combined track. Most muons are first reconstructed in the MS and then matched to an ID track (outside-in pattern recognition). The inside-out algorithm is used for the remaining uncombined tracks. In the global fit, the energy loss in the calorimeters is taken into account. More details about the muon reconstruction can be found in [66, 92].
Muons are required to be of *medium* quality [93] to minimise the systematic uncertainties associated with muon reconstruction and calibration. Only 0.38% hadrons decaying in flight are misidentified as prompt muons in $\mathrm{t\bar{t}}$ events within a transverse momentum range of $20 < p_{\mathrm{T}} < 100$ GeV, while prompt muons from the W decay are identified with an efficiency of 96.5% [93]. The transverse momentum of the muon is required to have $p_{\mathrm{T}} > 25$ GeV and due to the detector acceptance, a pseudorapidity $|\eta| < 2.5$ is required. In addition muon tracks must be compatible with the primary interaction by applying selection criteria on the transverse impact parameter significance $|d_0^{\mathrm{sig}}| < 3$ and on the longitudinal impact parameter $|z_0 \sin\theta| < 0.5$ mm. The same *gradient* isolation requirement as applied to electrons is used to obtain the same isolation efficiency performance as for electrons in order to reduce the contributions from fake and non-prompt muons, like muons from leptonic hadron decays.

[1] The transverse impact parameter significance is defined as $d_0^{\mathrm{sig}} = d_0/\sigma_{d_0}$, where σ_{d_0} is the uncertainty of the transverse impact parameter d_0.

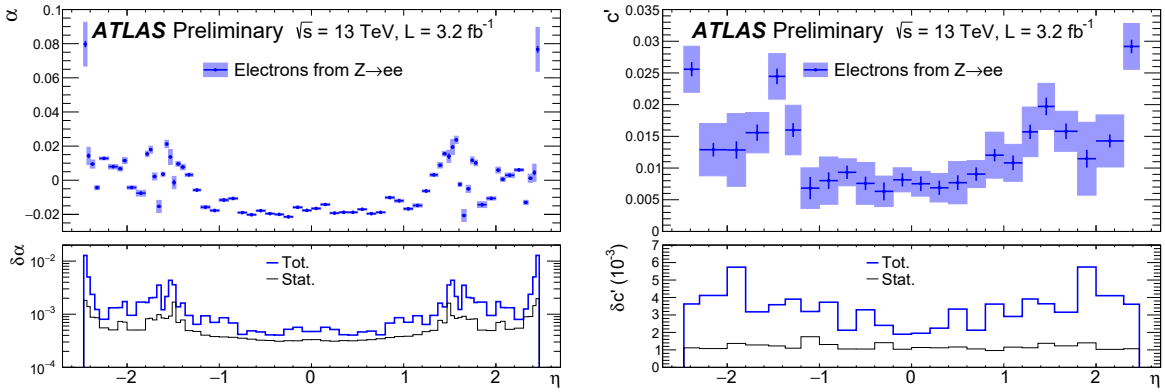

(a) (b)

Figure 7.11.: (a) Energy scale factor α, where α represents the deviation between data and simulation electron energies via $E_{\text{data}} = E_{\text{MC}}(1+\alpha)$. (b) Additional constant term c' for energy resolution, where c' is defined by $\left(\frac{\sigma(E)}{E}\right)_{\text{data}} = \left(\frac{\sigma(E)}{E}\right)_{\text{MC}} \oplus c'$. Both corrections are parameterized in η. The uncertainty bands on the top plots show the total uncertainties, while the black (blue) lines in the bottom plots represent the statistical (total) uncertainties [94].

7.3.3. Calibration

The electron energy and the muon momentum in simulation are corrected using $Z \to \ell\ell$ events to adjust the resolution in simulation to better model the data [94, 93].
The width of the reconstructed $Z \to \ell\ell$ mass distribution is sensitive to the energy/mo-mentum resolution. Differences between data and simulation are corrected by parameters, which are extracted by a binned maximum-likelihood fit derived from simulation comparing the invariant mass distributions for $Z \to \ell\ell$ candidates in data and simulation.
The measured electron energy calibration coefficients, shown in Figure 7.11, reach values up to a few percent. The total uncertainty on the electron energy scale factor is smaller than 0.1%[1], while total uncertainty on the energy resolution correction is around 0.3%.

The invariant mass distribution for corrected and uncorrected muons is shown in Figure 7.12. The total uncertainty on the momentum scale ranges from 0.05% for $|\eta| < 1$ to 0.3% for $|\eta| \sim 2.5$, which corresponds to a relative muon p_{T} resolution of 1.7% and 2.3% for small and high η values, respectively.

7.3.4. Event scale factors

In this analysis event scale factors are used, which are defined as the ratio of lepton reconstruction efficiencies measured in data and simulation in order to recover some precision in the detector simulation. The lepton reconstruction efficiency is determined by using a tag-and-probe method in $Z \to \ell\ell$ events [91, 93].

The scale factors are typically within 5 % of unity (except in crack-regions) and measured to a precision well below 1 %.

[1] Crack-region is excluded in electron selection

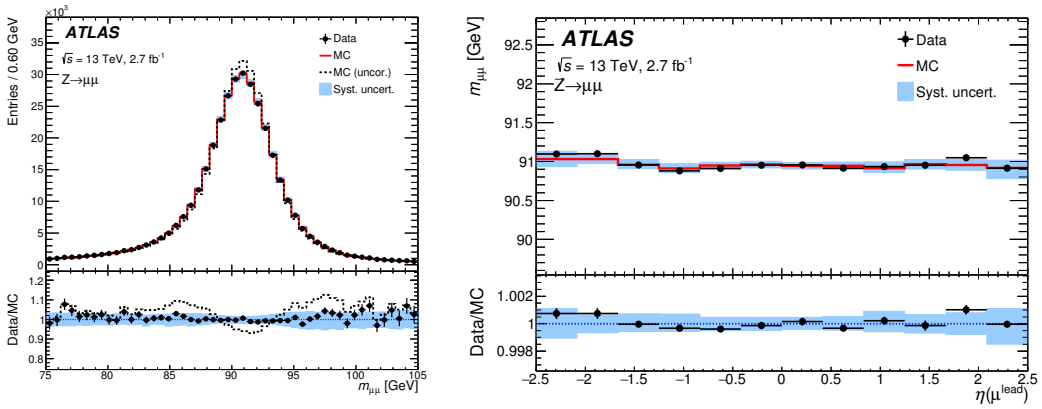

(a) (b)

Figure 7.12.: (a) Dimuon invariant mass distribution of $Z \to \mu\mu$ candidate events comparing data to the simulation with and without momentum corrections applied. (b) Stability of fitted mean mass for data and corrected simulation as a function of the pseudorapidity of the highest-p_{T} muon. In both plots the points show the data. The continuous line corresponds to the simulation with the muon momentum corrections applied to the MC sample while the dashed lines show the simulation when no correction is applied. The band represents the effect of the systematic uncertainties on the momentum corrections. The bottom panels show the data to MC ratios. The simulation distributions are normalized to the data [93].

7.4. Overlap removal

Most of the described reconstruction methods are run independently and therefore it is possible that some reconstructed objects can share the same energy depositions, e.g. electrons that are also reconstructed as jets in the calorimeter. The overlap removal is used to remove overlapping objects iteratively.

1. Jets reconstructed from calorimetric deposits of an electron are removed. This double counting of electron energy deposits is prevented by removing the closest jet with an angular distance $\Delta R < 0.2$ from a reconstructed electron. If the jet is b-tagged, the electron is removed instead.

2. Electrons are discarded if a jet exists within $\Delta R < 0.4$ of the electron, to ensure sufficient separation from the nearby jet activity, which reduces backgrounds from heavy-flavour decays.

3. Muons may be as a jet because of energy deposits from the muon in the calorimeter. Therefore, jets with fewer than three associated tracks are removed if they are within $\Delta R < 0.4$ of a muon unless the jet is b-tagged

4. Muons are discarded if they are separated from the nearest jet by $\Delta R < 0.4$, to reduce the background from muons originating in heavy-flavour decays inside jets.

8. Event selection and background estimations

The identification of $t\bar{t}$ pairs depends on the signature of their decay products. In Section 3.2.2 the top decay channels used in this thesis were described. The W boson from the top quark immediately decays into hadrons or leptons, while the b quark fragments into a b-jet. In the following chapter, the selection of dileptonic $t\bar{t}$ events at $\sqrt{s} = 13\,\text{TeV}$ is described. Thorough event selection is necessary to select the events of interest out of all $p - p$ collisions. Dileptonically decaying top quark candidates from the $t\bar{t}$ production are selected by requiring one isolated high-p_{T} muon and one isolated high-p_{T} electron with opposite charge signs. Also, at least two b-tagged jets with high-p_{T} are required. The b-tagging requirement ensures to select jets originating from b quarks with high probability. The events selection must take into account the detector acceptance. The full set of event selection requirements is presented in Section 8.1. Several other event selections that are slightly different from the standard selection (control regions) are utilised to estimate the contribution of background processes, which is explained in Section 8.2. Finally, the description of the data by the signal and MC simulations is demonstrated in Section 8.3 by comparing the event yields and differential distributions in various other control regions.

8.1. Event selection requirements

The first step of the event selection is to ensure that the data taking for the subdetectors have good quality, which means that no unrecoverable problem is affecting relevant detector components for a significant period of time. Therefore events are required to belong to runs taken over periods of stable LHC beams, listed in the so-called GoodRunList (GRL). Also, non-collision events (cosmic muons and beam background) are rejected.
During data taking sophisticated trigger, requirements are used to record as much as possible signal events since it is technically not possible to detect and record each $p - p$ collision. In this analysis two trigger chains are used: the single electron trigger chain and the single muon trigger chain. For electrons, events are required to have an isolated electron with $p_{\text{T}} > 24$ GeV and medium quality, an electron with $p_{\text{T}} > 60$ GeV and medium quality or an electron with $p_{\text{T}} > 120$ GeV and loose quality[2]. For muons, events are required to have an isolated muon with $p_{\text{T}} > 20$ GeV and loose quality or a muon with $p_{\text{T}} > 50$ GeV[3]. The event must pass one of the two trigger chains.
Events are required to have at least one primary vertex with five or more associated tracks with $p_{\text{T}} > 0.4$ GeV, to ensure that the event is a collision candidate. Events passing the above requirements are required to have exactly two selected leptons with opposite charge sign (OS)[4]. The lepton requirement drastically reduces the background from events with only hadronic activity. The jet cleaning requirement rejects events where any jet originates from detector effects (like sporadic noise bursts), beam and cosmic background. This criterium is referred to the bad

[2] HLT_e24_lhmedium_L1EM20VH OR HLT_e60_lhmedium OR HLT_e120_lhloose
[3] HLT_mu20_iloose_L1MU15 OR HLT_mu50
[4] SS indicates leptons with the same charge sign.

Criterion		Cut
1	GRL (data only)	data15_13TeV.periodAllYear_DetStatus-v73-pro19-08_ DQDefects-00-01-02_PHYS_StandardGRL_All_Good_25ns
2	Trigger (data only)	HLT_e24_lhmedium_L1EM20VH OR HLT_e60_lhmedium (seeded by L1EM20VH) OR HLT_e120_lhloose (seeded by L1EM20VH) OR HLT_mu20_iloose_L1MU15 OR HLT_mu50 (seeded by L1MU20)
3	Primary vertex	≥ 1
4	2 leptons	1 electron and 1 muon ($e\mu$ channel)
5	Jet cleaning	Bad jet rejection (tight)
6	≥ 2 b-tagged jets	MV2c20 with 77% WP

Table 8.1.: Nominal event selection. The object selections are used as described in Chapter 7.

jet veto later. For tight veto, events with jets originating from all possible detector effects get rejected, while for the loose veto only events with jets with noisy cells get rejected. Finally, at least two b-tagged anti-k_T jet (R = 0.4) with $p_T > 25$ GeV are required.
Table 8.1 summarizes the event selection separated in data and MC selections. MC events are reweighted using the scale factors on the identification, reconstruction, isolation and trigger efficiencies.

8.2. Background estimation

Several background processes have similar event topologies as the $t\bar{t}$ events in the dilepton channel. They can be classified into two types: events with two real prompt leptons from W or Z decays (including those produced via leptonic τ decays) and events with at least one misidentified lepton candidate (called fake lepton).
The first class includes single top quark production in the Wt channel, which is the dominant background in the $e\mu$ channel. Additionally, the diboson production channels WW, WZ and ZZ are considered as background since not every lepton is in the fiducial region. Drell-Yan processes in association with additional partons contribute by a small fraction to the $e\mu$ channel via $Z \to \tau\tau$. The Z/γ^*+jets events contribution is normalised by comparing to data (Section 8.2.1) in the same flavour channels, where its fraction of the background is much larger.
The second class includes events where at least one reconstructed lepton is misidentified. These leptons might originate from decays of a bottom or charm hadrons, photon conversions, hadronic jet activities or in-flight decays of pions or kaons. The contribution of these events is shown in Table 8.2 and is described in Section 8.2.2.

8.2.1. Drell-Yan background

The Drell-Yan (DY) process contributes via $Z/\gamma^* \to \tau^+\tau^-$ to the $t\bar{t}$ process in the $e\mu$-channel. In order to study the DY background, the selection criteria were adapted to have a DY enriched control region. The inclusive DY event selection requires two isolated, OS electron or muon pairs with $p_T > 25$ GeV and at least two jets (no b-tags). The inclusive DY production is reasonably well described by Sherpa v2.1 simulations as demonstrated in Figure 8.1.

Process	yield	stat. unc.	syst. unc.
Single top (Wt)	236	$\pm$ 2	$\pm$ 46
Fake leptons	117	$\pm$ 22	$\pm$ 120
Z+jets	6	$\pm$ 3	$\pm$ 1
Dibosons	3.1	$\pm$ 0.4	$\pm$ 1.5
Total background	362	$\pm$ 22	$\pm$ 130
$t\bar{t}(\geq 1$ pile-up jet)	310	$\pm$ 2	$\pm$ 88
$t\bar{t}$(no pile-up jets)	6850	$\pm$ 11	$\pm$ 940
Expected	7520	$\pm$ 25	$\pm$ 950
Observed	8050		

Table 8.2.: Yields of data and MC events fulfilling the selection criteria.

However, the amount of DY events in the nominal phase space is largely underestimated as shown in Figures 8.2(a) and 8.2(b).
In order to get a better estimate of the background normalisation for this analysis, a data-driven normalisation has been used. Events fulfilling the criteria described above were selected. The ratio of the number of events in the mass range of the Z production, $81 < M_{ll} < 101$ GeV, between data and MC is $1.29 \pm 0.07(stat) \pm 0.19(syst)$ for the ee channel and $1.44 \pm 0.06(stat.) \pm 0.35(syst)$ for the $\mu\mu$ channel [1]. The systematic uncertainty reflects the dependence on the additional jet multiplicity in the event, which is estimated using subsets of events with additional jets in the events. In Appendix A.1 the mass distributions for events fulfilling the nominal selection and requiring additional jets before are shown. The resulting scale factors as a function of the number of additional jets are shown in Figure 8.3. The quadratically sum of all differences of the scale factors to the nominal is used as systematic uncertainty.
The estimated ratio is used as a scale factor to correct the size of DY background contribution. The lepton mass distributions after applying the scale factors is shown in Figures 8.2(c) and 8.2(d). The scale factor for the analysis in the $e\mu$ channel is taken as the average of scale factors in the same flavour channels and amounts to $1.35 \pm 0.05(stat) \pm 0.20(syst)$.

[1] The same ratio estimated in the inclusive DY sample would result in a scale factor of $1.02 \pm 0.01(stat.)$ for the ee channel and $1.02 \pm 0.01(stat.)$ for the $\mu\mu$ channel.

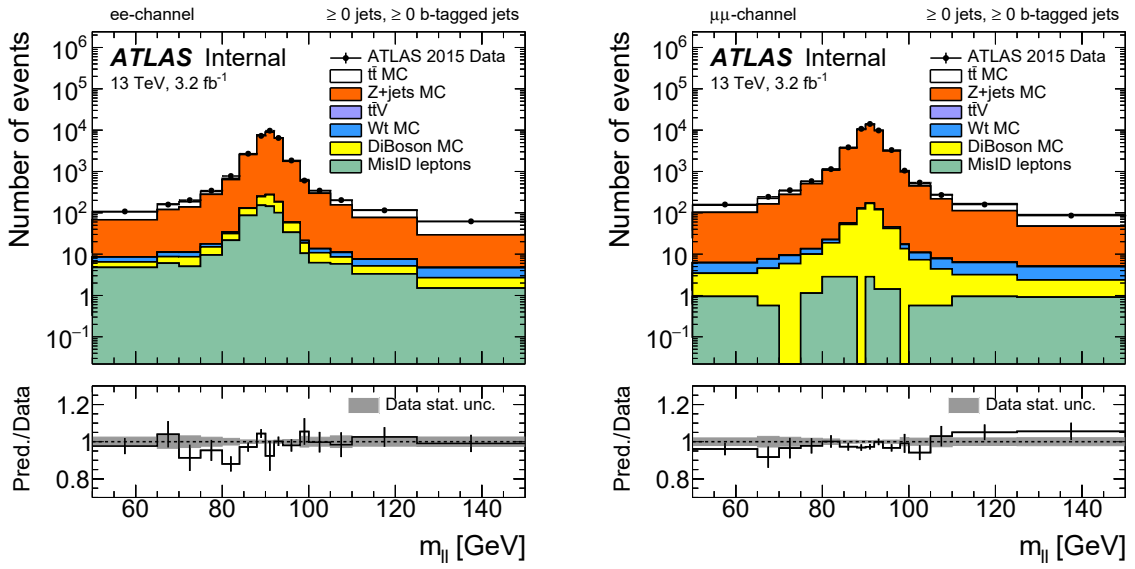

(a) (b)

Figure 8.1.: Dilepton mass distributions for events with two isolated, OS leptons with $p_{\mathrm{T}} > 25$ GeV and at least two jets (no b-tags) are shown for (a) *ee* channel and (b) $\mu\mu$ channel.

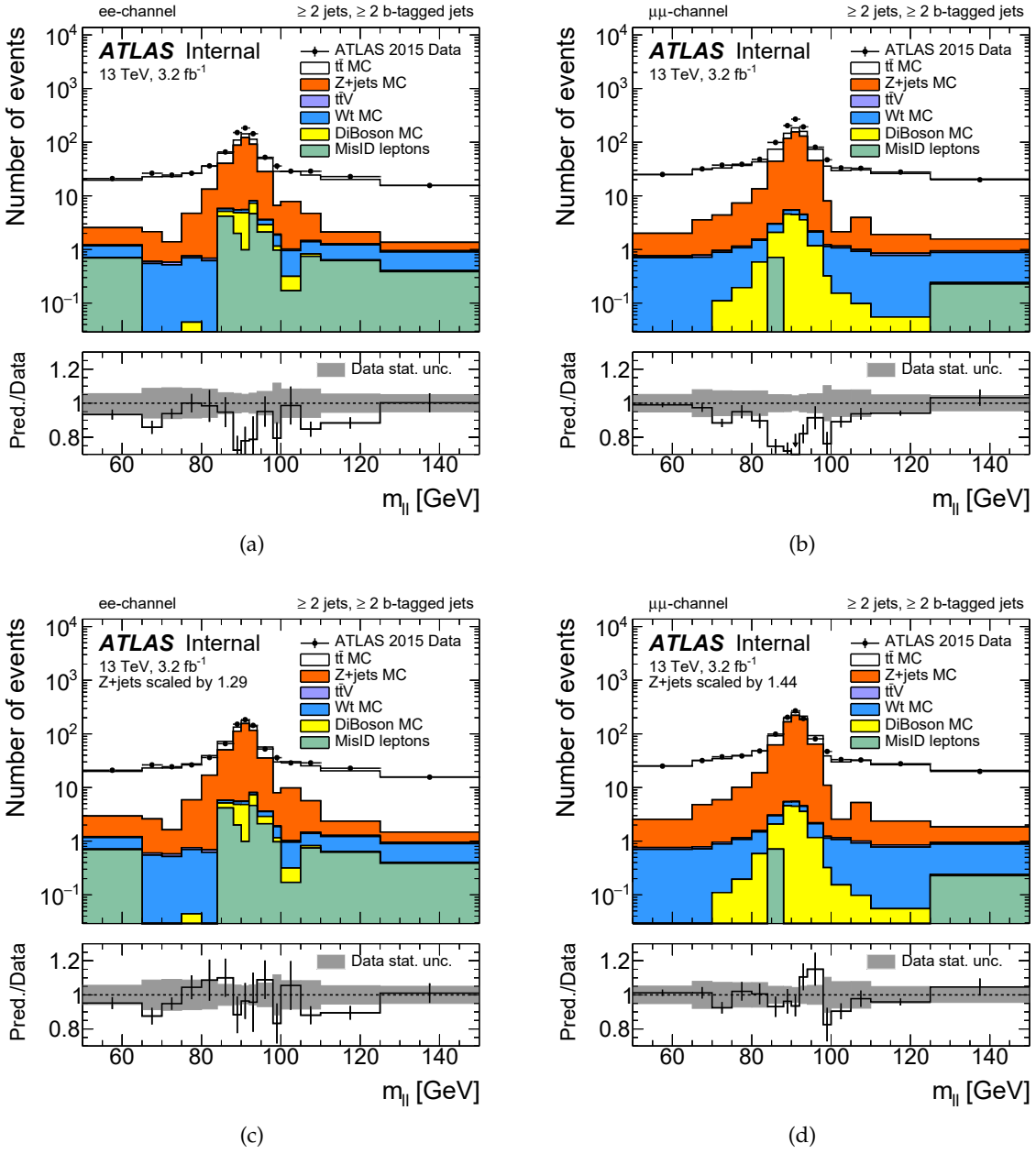

Figure 8.2.: Dilepton mass distributions in the same lepton flavour channels with nominal selection before (a, b) and after (c, d) applying the normalisation scale factors. The area under the the Z peak ($81 < M_{ll} < 101$ GeV) in (a, b) is used to derive the normalisation scale factor.

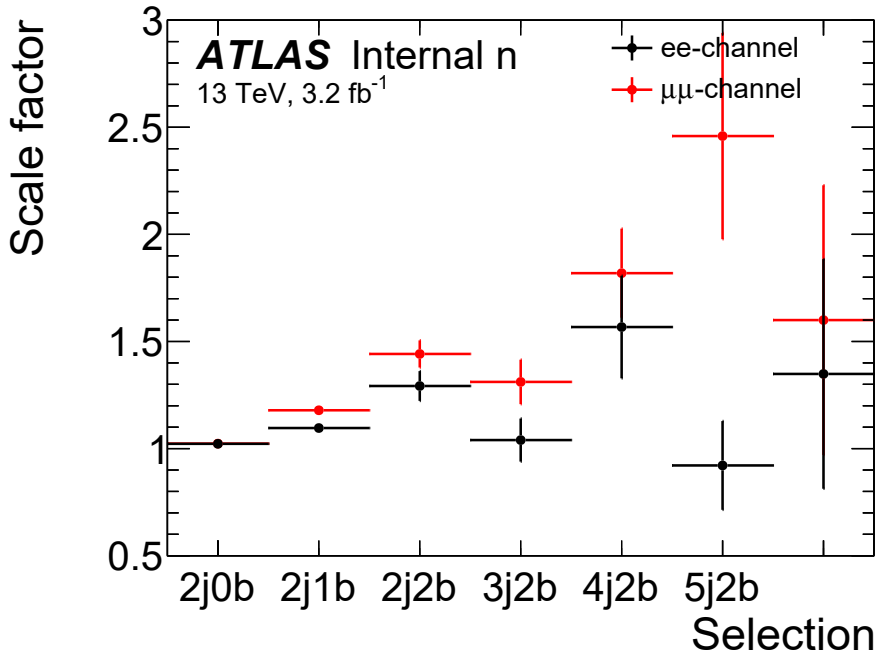

Figure 8.3.: Estimated scale factors as function of the minimal number of jets (j) and *b*-tagged jets (b). The bars show the statistical uncertainties.

Component	eμ-channel	
	OS	SS
Electrons from photon conversion	25.7	8.4
Electrons from heavy-flavour decays	1.3	1.5
Electrons from other processes	2.0	0.0
Muons from photon conversion	0.3	0.1
Muons from heavy-flavour decays	2.1	0.4
Mouns from other process	1.2	0.1
Total non-prompt leptons	32.7	10.5
Prompt leptons	7122.4	11.2
Total $t\bar{t}$ MC	7155.1	21.7
Total Data	8050.0	49.0

Table 8.3.: Overview of event counts for misidentified leptons. The counts from the $t\bar{t}$MC sample are split by sources of misidentified leptons based on the generated process information inside the sample.

8.2.2. Background from misidentified leptons

In addition to the processes with prompt $e\mu$ pairs, it is possible to have events with objects misidentified as electron or muon in the signal region. These fake or non-prompt leptons originate from either a heavy-flavour decay, photon conversion, jet misidentification or meson decay. The main source of these leptons comes from $t\bar{t}$ production where only one of the top quarks decays leptonically, while the other top quark decays hadronically and produces jets in the detector. This background is estimated from a combination of data and simulation, using the method as in [95]. This approach is chosen because it is almost impossible to simulate each process leading to misidentified leptons and rely on Monte Carlo predictions to understand this background.
In MC simulation the contributions from each misidentification source are estimated from $t\bar{t}$ events with at least two b-tagged jets. The history of the stable particles in the MC generator record is used to identify fake leptons from these processes by identifying leptons that have decayed from hadrons. In Table 8.3 the number of events for each process contribution to misidentified leptons arising from $t\bar{t}$ events is shown.

The contribution of events with misidentified leptons in data is calculated by:

$$N_{MisID,data} = (N^{SS}_{data} - N^{SS}_{prompt,mc}) \cdot \frac{N^{OS}_{MisID,MC}}{N^{SS}_{MisID,MC}}, \tag{8.1}$$

where $N_{MisID,data}$ refers to the number of background events in data. The total number of SS events in data, N^{SS}_{data}, is substracted by the number of dilepton $t\bar{t}$ events where one lepton is reconstructed with the wrong sign. Lastly, $N^{OS}_{MisID,MC}$ and $N^{SS}_{MisID,MC}$ refer to the number of misidentified events with OS and SS leptons according to the inclusive $t\bar{t}$ MC (see Table 8.3). This ratio is often called fake factor.
Other background processes with only one prompt lepton include t-channel single top production and W+jets with the W decaying to $e\nu$, $\mu\nu$ or $\tau\nu$ where the τ-lepton subsequently decays leptonically. The contribution of these backgrounds is very small and they are assumed to be negligible. Processes with two misidentified leptons, are also negligible for the event selections

used in this analysis.
The large difference in same-sign eμ events with at least two b-tagged jets between data and MC, shown in Appendix A.2 Figure A.5, leads to the decision to use an uncertainty of 100% for the backgound with misidentified leptons in the following analysis.

8.2.3. Background from pile-up jets

Additional analysis has been made to estimate the impact of jets arising from pile-up because this analysis is relying on a good reconstruction of additional jets in $t\bar{t}$ events. This is due to the unfolding to the particle level, which is explained in detail in Chapter 9. The step where the migration matrix is applied removes any additional jets from pile-up because the generator objects of the hard events in MC do not depend on the pile-up. Therefore a good data to Monte Carlo modelling is required, which is tested by a sideband method inverting the JVT cut. This sideband consists mostly of well-separated pile-up jets plus smaller contamination of good jets which fail the JVT algorithm due to inefficiency.
However, this requires to remove the tight veto for events with bad jets, because there is a strong correlation for jets passing the JVT cut and passing that veto. This veto removes events with jets that originate from detector effects (like sporadic noise bursts), beam and cosmic background. Not removing that veto would reject 40% of all events. Instead, the loose bad jet veto is used, which mostly reject only noisy cells. This veto rejects only 0.3% of the good events, which is fully acceptable for this study.
In order to study the impact of pile-up jets matching algorithm is applied to split reconstructed jets into signal and pile-up jets. The matching algorithm uses the spatial distance of the reconstructed jet to a particle level jet. Signal jets are considered those with $\Delta R < 0.4$ (matched jets), while jets with $\Delta R > 0.4$ are considered to be pile-up jets (unmatched jets). In order to avoid counting of split jets as pile-up, there is no limit on the number of jets matched to a given particle jet.
Figure 8.4 shows the distribution of the pile-up and the signal jets. As expected pile-up jets have mainly low p_{T} since they originate from background effects. On average there is a contamination of about 2-3% of pile-up jets in the signal jets which are dominantly at low p_{T} and make up 10% of the jets in the lowest p_{T} bin. A weak dependence on η can also be observed, especially at $1.1 < |\eta| < 1.6$, which is exactly the region where a lot of detector material is located (crack-region). In this region, the number of unmatched (pile-up) jets in the signal and the pile-up sample increases and the number of matched jets in the pile-up sample drops by about 15%.
Figure 8.5 shows the data-MC comparison of the signal and the pile-up jet regions. The pile-up region is not well modelled: the p_{T} of the pile-up jets is softer in MC than in data while the additional signal jets have a harder p_{T} in MC than in data. Following a similar logic as discussed in [96] we will deduce the efficiency for pile-up jets with the JVT cuts from data to scale the 2-3% of remaining pile-up jets in the signal sample with a proper background scale factor.
The scale factor estimation is based on events in the sideband of the JVT distribution ($JVT < 0.5$). This estimation requires good data to MC modelling of the pile-up jets. In Figure 8.6a the JVT discriminant for data compared to matched and unmatched jets in MC is shown. The same ΔR matching criteria as for the purity study above has been used. It is visible that the sideband is mostly contaminated by pile-up jets (unmatched jets) plus a smaller contribution of good jets which fail the JVT algorithm due to inefficiency (matched jets). The inefficiency is about 8% for the chosen JVT working point.

The scale factor for pile-up jets is calculated from

$$SF = \frac{N_{jets}^{data} - N_{jets}^{BG} - N_{jets}^{Match}}{N_{jets}^{Unmatch}}, \tag{8.2}$$

where N_{jets}^{data} and N_{jets}^{BG} are the number of jets in data and background fulfilling the standard selection criteria except the jet veto cut that is looser for this study. N_{jets}^{Match} is to the number of reconstructed jets with a $\Delta R < 0.4$ match to a particle level jet. $N_{jets}^{Unmatch}$ refers to pile-up jets, since the are not matchable to any particle level jet. The scale factor is estimated to be $SF = 0.83 \pm 0.03(stat.)$ from events in the side band. Figure 8.6b shows the JVT distribution after applying this scale factor. A better agreement is reached in particular for events with JVT=0.

An alternative approach is to estimate the uncertainty of the pile-up jet contamination by using pile-up variation samples, i.e. scaling the pile-up reweighting factor[1] up and down. This scaling is performed on the number of vertices in the event which is correlated with the number of additional $p - p$ collisions. Figure 8.7 shows the JVT distributions of the jets in events fulfilling the event selection on reconstruction level in data and MC and the various samples. These variations give a reasonable estimate on the possible differences between data and MC in the signal region $JVT > 0.59$. In order to estimate the overall uncertainty of the pile-up contribution to the sample, the largest difference from the pile-up reweighting variations is propagated to estimate the effect on the final result.

It is important to note, that, as already mentioned, most of the pile-up jet contribution is already corrected via the migration matrix of the jet multiplicity, shown in Figure 9.3. At particle level no pile-up jets are stored and therefore N_{jets}^{part} does not include any pile-up jets. However, as already shown, at reconstruction level pile-up jets survive the jet selection, which leads to an increase of the overall reconstructed jets, resulting in $N_{jets}^{reco} > N_{jets}^{part}$. pile-up jets have dominantly at low p_{T}, therefore this effect is mostly visible in the lowest jet p_{T} region (p_{T}> 25 GeV) and is already negliable for $p_{\mathrm{T}} > 40$ GeV. This is especially visible in the off-diagonal entries of the jet multiplicity response matrix, which are greater than 0.1 for $p_{\mathrm{T}} > 25$ GeV, but between 0.01 and 0.05 $p_{\mathrm{T}} > 40$ GeV.

8.3. Differential distributions

The differential distributions of Monte Carlo and data are compared in different control regions in the following. As basis for the event selection the standard selection criteria as listed in Table 8.1 is used and slightly modified for specfic control regions. The Drell-Yan background is reweighted as described in Section 8.2.1 and misidentified leptons are estimated as described in Section 8.2.2. In addition, all object level corrections that were described in Chapter 7 are applied.

8.3.1. Low jet multiplicity control region

In the first control region, the overall jet multiplicity is tested. The standard selection already includes a minimum of two b-tagged jets. Thus this cut has been removed to test the multi-

[1] Usually, Monte Carlo samples are produced before or during a given data taking period. Therefore only expected data pile-up conditions can be put into the Monte Carlo. Thus, there is the need at the analysis level to reweight the Monte Carlo pile-up conditions to what is found in the data taken.

plicities below two jets. In Figure 8.8 shows the jet multiplicity (n_{jet})and the b-jet multiplicity (n_{b-jet}). The contributions from the background of Drell-Yan, di-boson and single top (Wt) production are the largest for $n_{jet} \leq 2$ and especially for $n_{b-jet} < 2$. Events without a b-jet are mainly from Drell-Yan production. However, the background from Drell-Yan and Diboson drops significantly with the increasing number of b-jets. This show nicely the importance of requiring at least two b-tagged jets, since this removes almost all background events and leaves an almost clean $t\bar{t}$ sample with only minimal background (dominantly from Wt).

8.3.2. Data-MC comparison for standard selection criteria

In the last step of the comparison between data and Monte Carlo prediction the lepton and jet distributions are checked when applying the standard selection criteria as described in Table 8.1.
Figures 8.9(a) and 8.9(b) show the jet p_{T} of the leading b-jet and the leading extra jet. Difference between data and MC simulation are 10-15%. Additionally, the jet multiplicities for jet p_{T} thresholds of 25 and 40 GeV are shown in Figure 8.9(c) and Figure 8.9(d). For the lowest jet p_{T} threshold, a jet multiplicity dependent deviation between data and simulation is visible which increases to about 20% at the highest multiplicity bin. For the 40 GeV threshold, the predictions are lower than the data in the highest multiplicity bin.
A full collection of data-MC comparisons is available in appendix Appendix B. Some of the not published diagrams are highlighted in the following.
In Figure B.5 the jet multiplicity is shown for three different m_{llbb} regions. m_{llbb} is reconstructed by summing up the Lorentz vectors of the electron, the muon and the two b-tagged jets with the highest p_{T} in the event. The thresholds of the regions are chosen in a way that every region is left with enough data events to get statistically significant results. Figure B.5 shows that the data is described well for events with no additional jets in the events for all regions. However, with the increasing jet multiplicity, there are fewer events in the simulation, which results in differences of about 20-30%. However, the statistical uncertainties increase as well, and the significance gets smaller with increasing jet multiplicity.
Figure B.6(a) shows the distribution of H_{T}, which is defined as the p_{T}-sum of all reconstructed objects. H_{T} peaks at around the mass of the $t\bar{t}$ system. Simulation has about 10% fewer events in all bins compared to data. Figure B.6(d) and Figure B.6(b) show the $\Delta R(\mathrm{j},\mathrm{j})$ and $\Delta\phi(\mathrm{j},\mathrm{j})$ distribution for events with at least two additional jets in the event. Both correlations are using the two jets with the highest p_{T} for events with more than two additional jets in the event. The theoretical prediction has about 10-20% fewer events than data. The same observation is done for the invariant mass of the two leading additional jets, which is shown in Figure B.6(c). The invariant mass is calculated using the reconstructed Lorentz vectors of each jet.

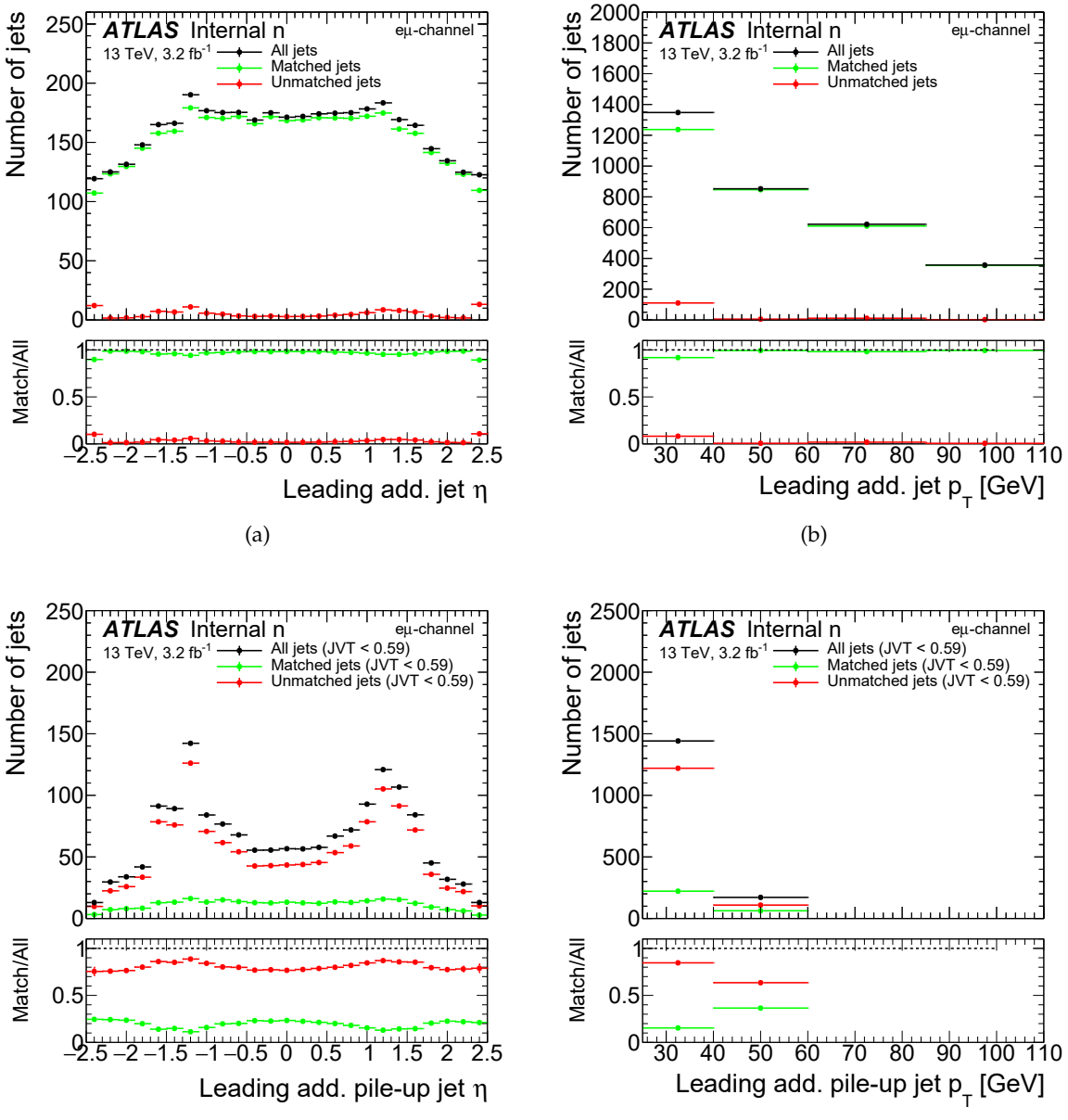

Figure 8.4.: Distributions of (a) η and (b) p_{T} of jets with JVT>0.59 in events fulfilling the standard selection criteria, while for (c) and (d) the tight jet veto cut got removed.

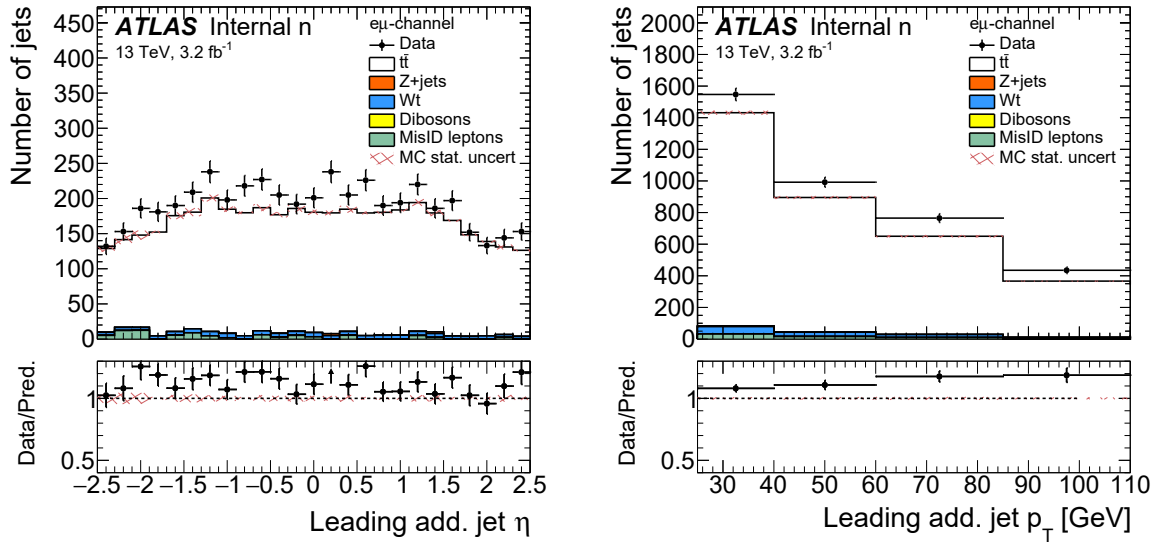

(a)

(b)

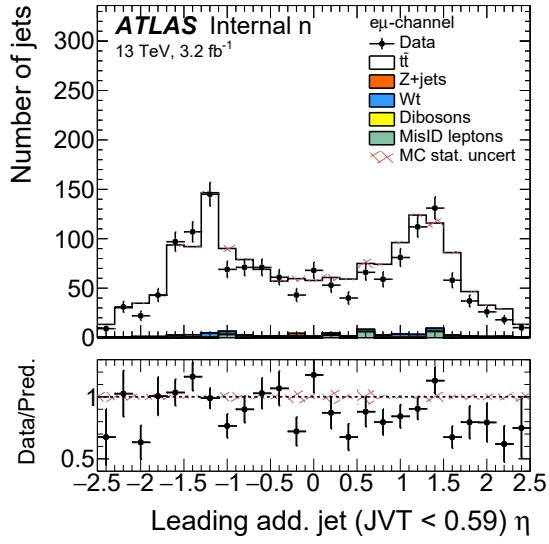

(c)

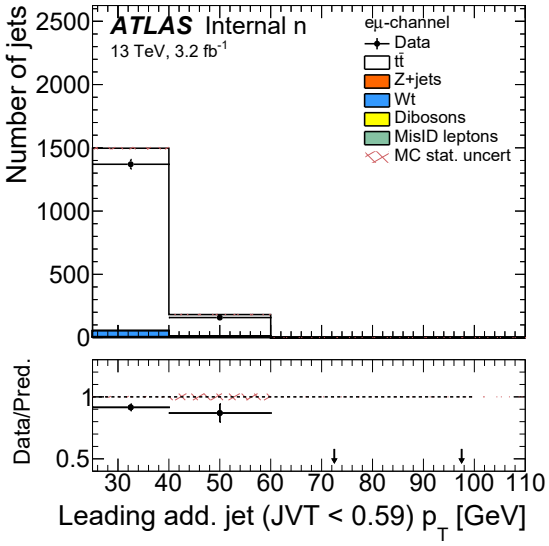

(d)

Figure 8.5.: a) eta and (b) p_{T}distribution of jets with JVT>0.59 in events fulfilling the standard selection criteria; (c) eta and (d) p_{T}distribution of jets with JVT<0.59 in events fulfilling the standard selection criteria except for the tight veto cut.

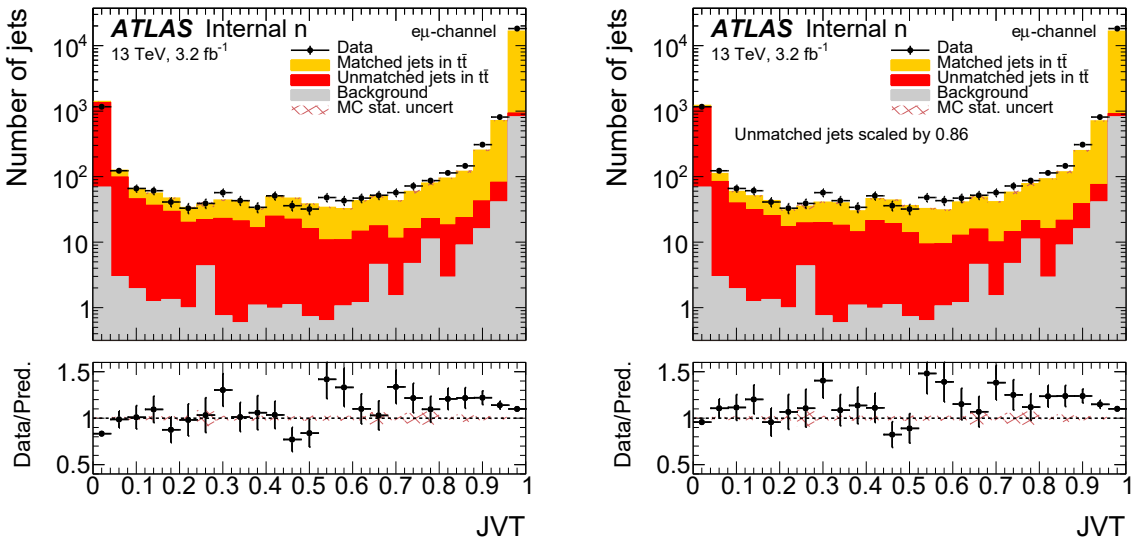

(a) (b)

Figure 8.6.: JVT discriminant (a) without and (b) with applying the scale factor for pile-up jets estimated from the JVT sideband ($JVT < 0.5$). Matched jets are those where the reconstructed jet could be matched to a particle level jet within $\Delta R < 0.4$, unmatched are those failing this criterion.

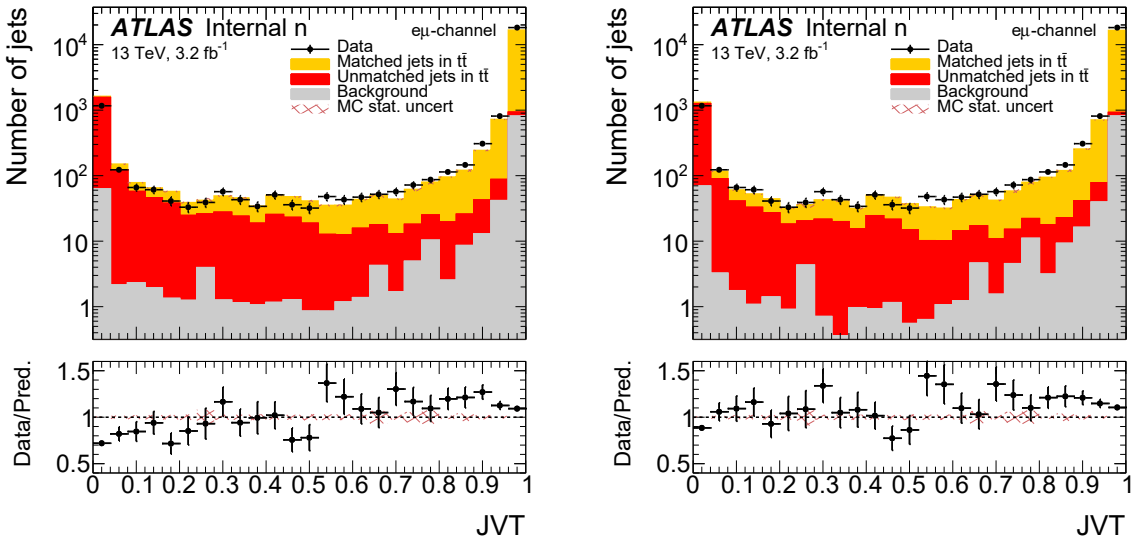

(a) (b)

Figure 8.7.: JVT distribution of jets fulfilling the standard selection criteria except the jet veto for (a) the sample with increased pile-up (up variation) and (b) the sample with decreased pile-up (down varaition).

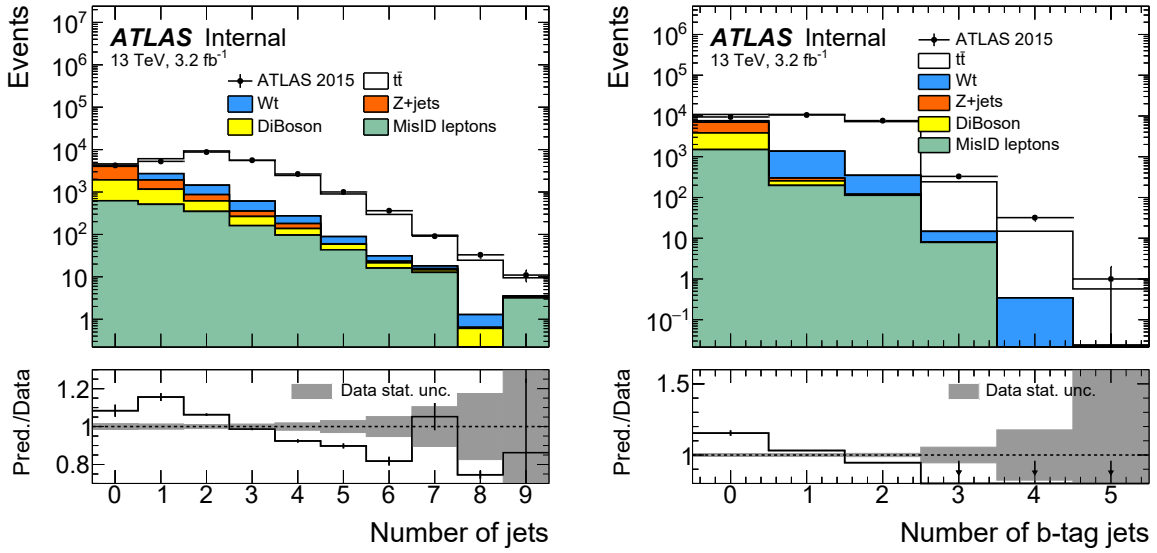

(a) (b)

Figure 8.8.: Low jet multiplicity control plots. Jet multiplicity (a) and b-jet multiplicity (b) in events with standard selection criteria except the requirement of at least two b-jets in the $e\mu$ channel. Uncertainties are statistical only.

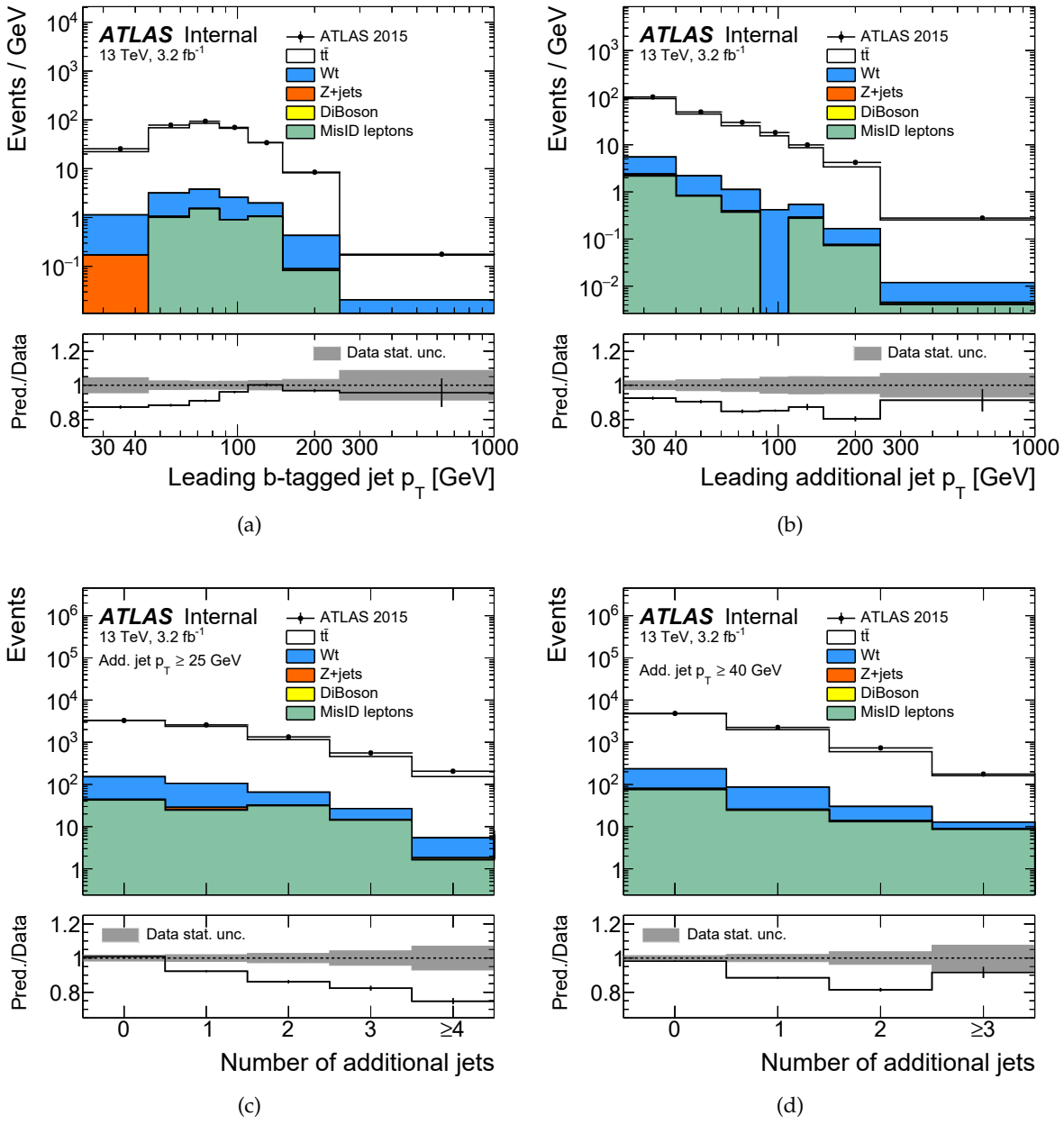

Figure 8.9.: Data-MC comparisons for events fulfilling the standard selection criteria as in Table 8.1. Leading b-jet p_{T} (a), leading additional jet p_{T} (b) and additional jet multiplicities with jet $p_T > 25$ GeV (c) and jet $p_T > 40$GeV (d) are shown. Uncertainties are statistical only.

9. Unfolding to particle level

This chapter describes the method that has been used to obtain the measured differential cross sections from data for all observables defined in Section 5.3. The unfolding technique described in the following corrects for any detector and reconstruction effects. These effects can change the actual extra jet spectrum in several ways. Jets from the hard scattering process can be lost due to inefficiencies in the reconstruction, the transverse momentum of the jet is smeared because of the p_{T} resolution of the calorimeters, and the rank of two reconstructed jets can be swapped relative to the truth jets (e.g. leading truth jet reconstructed as a subleading jet or vice versa). Also, jets can migrate into and out of the fiducial region. The unfolding procedure corrects for all these effects.
In order to compare reconstructed data with predictions a common fiducial phase space is defined in Section 9.1, which is followed by generator comparisons at particle level. The used iterative Bayesian unfolding method [97] is described in Section 9.3. The technique is then verified in Section 9.4.

9.1. Fiducial volume definition

All measurements in this thesis are corrected to the particle level in one common fiducial volume.
Only stable particles with a lifetime greater than 0.3×10^{-10} s are used to construct objects like leptons and jets from MC generators. These particles are called primary and are directly produced in $p-p$ interactions or subsequent decays of particles with a shorter lifetime.
All Leptons (e, $\mu, \nu_e, \nu_{mu}, \nu_\tau$) are selected that are not produced by hadron decays. Photon radiation effects (i.e. through Bremsstrahlung) are considered in the four-vector reconstruction of electrons and muons by adding all photon four-vectors within a cone of $\Delta R = 0.1$ around the original lepton directions.
Jets are clustered out of all particles except for the above-defined leptons using the anti-$\mathrm{k_T}$ algorithm with $R = 0.4$. Jets initiated by b-quarks were identified via the ghost matching [83] with hadrons containing a b-quark with $p_T > 5$ GeV.
The fiducial volume used in this thesis is defined using events with exactly one opposite-sign electron-muon pair and at least two b-tagged jets. All objects including additional jets are required to fulfill $p_{\mathrm{T}} > 25$ GeV and $|\eta| < 2.5$. In order to closely align with the object selection at reconstruction level (see Chapter 7) the same jet-lepton overlap removal has been applied, thus events with jet-electron or jet-muon pairs with $\Delta R < 0.4$ are rejected. A summary is given in Table 9.1.

Exactly 1 electron and 1 muon with opposite sign, $p_T > 25$ GeV and $\lvert\eta\rvert < 2.5$
Two or more b-jets with $p_T > 25$ GeV and $\lvert\eta\rvert < 2.5$
No jet-electron or jet-muon pair with $\Delta R < 0.4$

Table 9.1.: Fiducial volume definition applied on events at particle level.

9.2. Distributions at particle level

In Figure 9.1 the distributions at generator level for jet multiplicities with p_{T} thresholds 25 and 40 GeV are shown. Differences in the shapes of the distributions are especially visible for Sherpa v2.2 and MadGraph5_aMC@NLO+PYTHIA 8 compared to the baseline $t\bar{t}$ sample Powheg+PYTHIA 6. The relative differences reach values up to 40-50%, which highlights the effect of using different event generation and parton shower techniques. More distributions at particle level can be found in Appendix C.1.

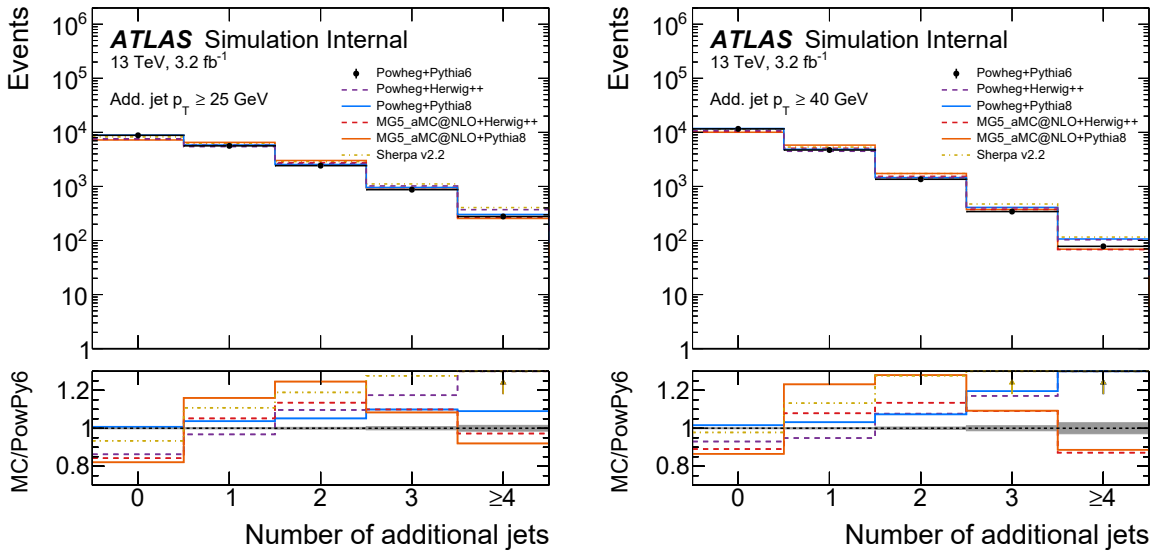

(a) (b)

Figure 9.1.: Generator comparison of jet multiplicity at particle level for different jet p_{T} thresholds: (a) 25 GeV and (b) 40 GeV.

9.3. Unfolding procedure

The normalised differential cross-section is given by:

$$\frac{1}{\sigma}\frac{d\sigma_i}{dX} = \frac{N^i_{unfold}(X)}{N_{events}} \tag{9.1}$$

where X is replaced by any observable used in this analysis. N_i is the number of entries in each bin i and N_{events} is the normalisation factor and thus the total number of events.
Due to limited efficiencies and detector resolutions, differences between reconstructed and particle-level distributions exist and were corrected with an iterative Bayesian unfolding [97]. The implementation in software package RooUnfold [98] is used.
In the following the unfolding procedure is observable independently described. The full cor-

rection procedure is given by the equation:

$$N^i_{unfold} = \frac{1}{f^i_{eff}} \cdot \sum_j (\mathcal{M}^{-1})^{part,i}_{reco,j} \cdot f^j_{acc}(\mathcal{N}^j_{data} - \mathcal{N}^j_{bg}), \tag{9.2}$$

where N^i_{unfold} is the total number of fully corrected particle-level entries in bin i. $\mathcal{N}^j_{data}$ and $\mathcal{N}^j_{bg}$ are the number of entries in bin j at reconstruction level. f^j_{acc} is the acceptance correction, while f^i_{eff} is the efficiency correction. $\mathcal{M}^{-1})^{part,i}_{reco,j}$ is the migration matrix. Each component is discussed in detail in the following.
The unfolding process starts with the number of entries in bin j at reconstruction level. To obtain this the number of entries in data $\mathcal{N}^j_{data}$ are substracted by the number of entries in background events $\mathcal{N}^j_{bg}$. In an ideal world this should correspond to only $t\bar{t}$ events folded with detector effects.
In the second step a factor f^j_{acc} corrects for migration across the fiducial boundary in reconstruction. This adjusts cases where the event passes all requirements at reconstruction level, but fail any requirement of the fiducial phase space. This might happen due to resolution effects on the transverse momentum, when leptons or jets fail the fiducial p_{T} or η cuts, while the reconstructed object pass. Another example is when the reconstructed leptons originate from the decay of a hadron or another background, such as conversions. In a few other cases, a light jet might get reconstructed as a b-tagged jet, while at particle level no B-hadron is matchable to the jet.
The following ratio, therefore, determines the acceptance correction:

$$f^j_{acc} = \frac{\mathcal{N}^j_{reco+part}}{\mathcal{N}^j_{reco}}, \tag{9.3}$$

where $\mathcal{N}^j_{reco}$ is the number of entries in bin j passing all selection criteria at reconstruction level. $\mathcal{N}^j_{reco+part}$ is the number of entries in bin j, where the events pass all criteria at reconstruction level and are within the fiducial volume as defined in Table 9.1. The Figure C.4 shows the acceptance correction as a function of the jet multiplicity at particle level for different m_{llbb} regions. The correction factor decreases with increasing jet multiplicity in every m_{llbb} regions by about 10%. In Figure C.5, which shows f^j_{acc} as a function of H_{T}, $\Delta\phi(\mathrm{j},\mathrm{j})$, $\Delta R(\mathrm{j},\mathrm{j})$ and m_{jj}, the factor is stable across the whole range of every observable. The final correction factor used for data is taken from the baseline Powheg+PYTHIA 6 sample.
The response matrix $\mathcal{M}^{part,i}_{reco,j}$ sets the distribution at reconstruction level in correlation with the one at particle level. Another way to express this is the conditional probability $\mathrm{P}(\mathcal{N}^j_{reco}|\mathcal{N}^i_{part})$ for finding an event with $\mathcal{N}^i_{part}$ entries in bin i at particle level given $\mathcal{N}^j_{reco}$ entries in bin j at reconstruction level. The matrix is filled from events of the baseline Powheg+PYTHIA 6 MC where both reconstruction and particle level requirements are fulfilled.
In the unfolding process the matrix is applied iteratively as part of Bayesian unfolding in order to go from a reconstructed distribution to a particle distribution. However, some bins of the matrix may be sparsely populated, and information loss occurs from detector imperfections. Therefore unphysical bin-to-bin fluctuations are prevented by regularisation through the iterative Bayesian algorithm. The corrected spectra were found to converge after four iterations of

the Bayesian unfolding algorithm [66].
C.6 shows the response matrix for the jet multiplicity in different m_{llbb} regions. All matrices have most of the entries in the diagonal while in the bins one above and one below the diagonal entries have values from 10% for low jet multiplicities to 20% for high jet multiplicities.
The particle jet multiplicity in the matrix does not contain any pile-up jets as they are not stored in the truth event record. However, the reconstruction level jet multiplicity does include pile-up jets if they fulfil the reconstruction level selection, in particular, $JVT > 0.59$. Pile-up jets surviving the selection would increase the fraction of events with $N_{jets}^{reco} > N_{jets}^{part}$.
In Figure C.7 the response matrix is visualised for H_{T}, $\Delta\phi(\mathrm{j},\mathrm{j})$, $\Delta R(\mathrm{j},\mathrm{j})$ and m_{jj}. About 15%-25% of the events have a smaller reconstructed H_{T} compared to the truth H_{T}. For $\Delta\phi(\mathrm{j},\mathrm{j})$ and $\Delta R(\mathrm{j},\mathrm{j})$ the off-diagonal entries are filled up to values of 10%. This might be caused due to the pretty coarse binning, which requires a rather big mismeasurement of the additional jet-pair system. The entries in the m_{jj}-Matrix above and below the diagonal line are equally distributed with 10%-15%.
In order to account for detector inefficiencies an efficiency factor f_{eff}^{i} is applied as bin-by-bin correction. The majority of events passing the particle level selection fail the reconstruction level selection criteria. Therefore f_{eff}^{i} determines the efficiency to reconstruct an event in bin i of the corresponding observable, when the event passes the particle level selection criteria:

$$f_{eff}^{i} = \frac{\mathcal{N}_{reco+part}^{i}}{\mathcal{N}_{part}^{i}}, \tag{9.4}$$

where $\mathcal{N}_{part+reco}^{i}$ is the number of entries in bin i fulfilling both, the fiducial volume selection at particle level and the reconstruction level selection, and $\mathcal{N}_{part}^{i}$ is the number of entries in bin i that fulfil the particle level selection. This correction is measured as function of each observable measured at particle level. Since the final measurement is normalized by the number of events in data, the correction factor f_{eff}^{i} corrects only for the bias in the spectrum, not the efficiency in number of events. The final correction factor used for data is taken from the baseline Powheg+PYTHIA 6 sample.
In Figure C.8 the efficiency correction is shown as a function of jet multiplicity at particle level in different m_{llbb} regions. The efficiency is not depended on the jet multiplicity and is flat at around 30%. The same is true for f_{eff}^{i} for $\Delta\phi(\mathrm{j},\mathrm{j})$, $\Delta R(\mathrm{j},\mathrm{j})$ and m_{jj} shown in Figure C.9. Only the correction as function of H_{T} shows a dependence on the measured observable. With increasing H_{T} the efficiency rises from around 27% to 36%.

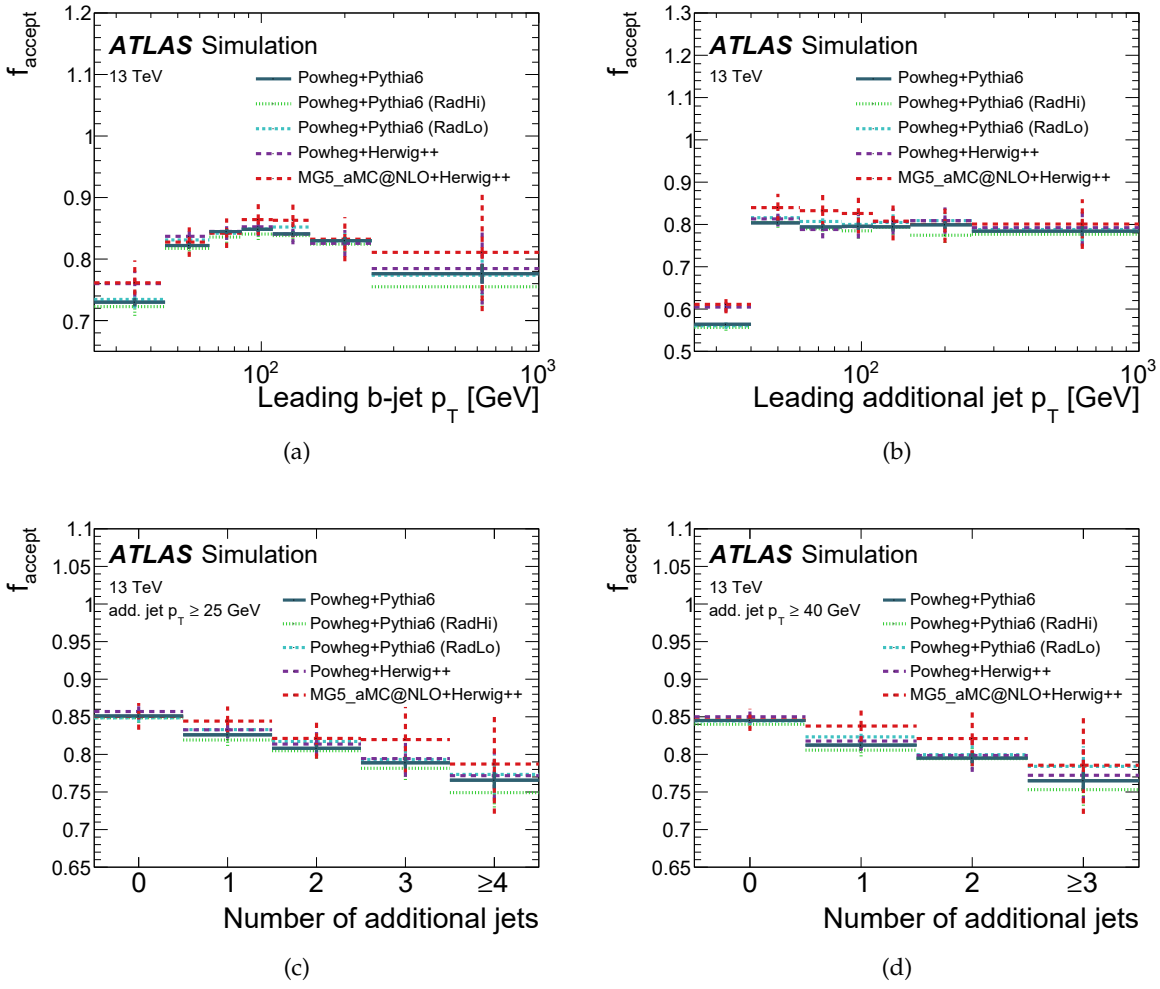

Figure 9.2.: Acceptance correction as defined in Equation 9.3 for (a) leading b-jet p_{T}, (b) leading additional jet p_{T}, (c) jet multiplicity with $p_{\mathrm{T}} > 25$ GeV and (d) $p_{\mathrm{T}} > 40$ GeV at reconstruction level. The distributions are shown with statistical uncertainties only. The blue solid line represents the corrections from the baseline Powheg+PYTHIA 6 MC, the distributions from other MCs are overlaid just for reference.

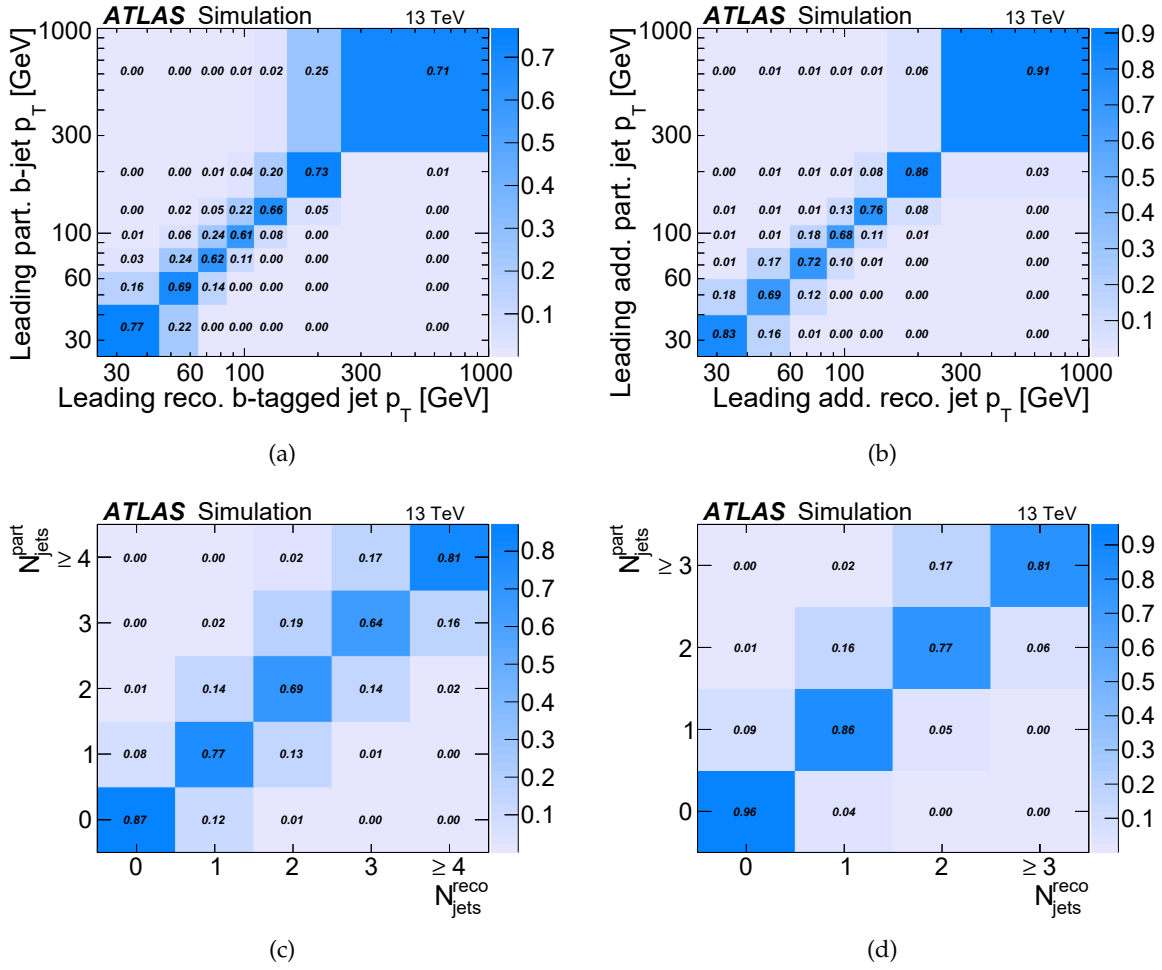

Figure 9.3.: Response matrix for (a) leading b-jet p_T, (b) leading additional jet p_T, (c) jet multiplicity with $p_T > 25$ GeV and (d) $p_T > 40$ GeV. The matrix is filled from events of the baseline Powheg+PYTHIA 6 MC where both reconstruction and particle level requirements are fulfilled.

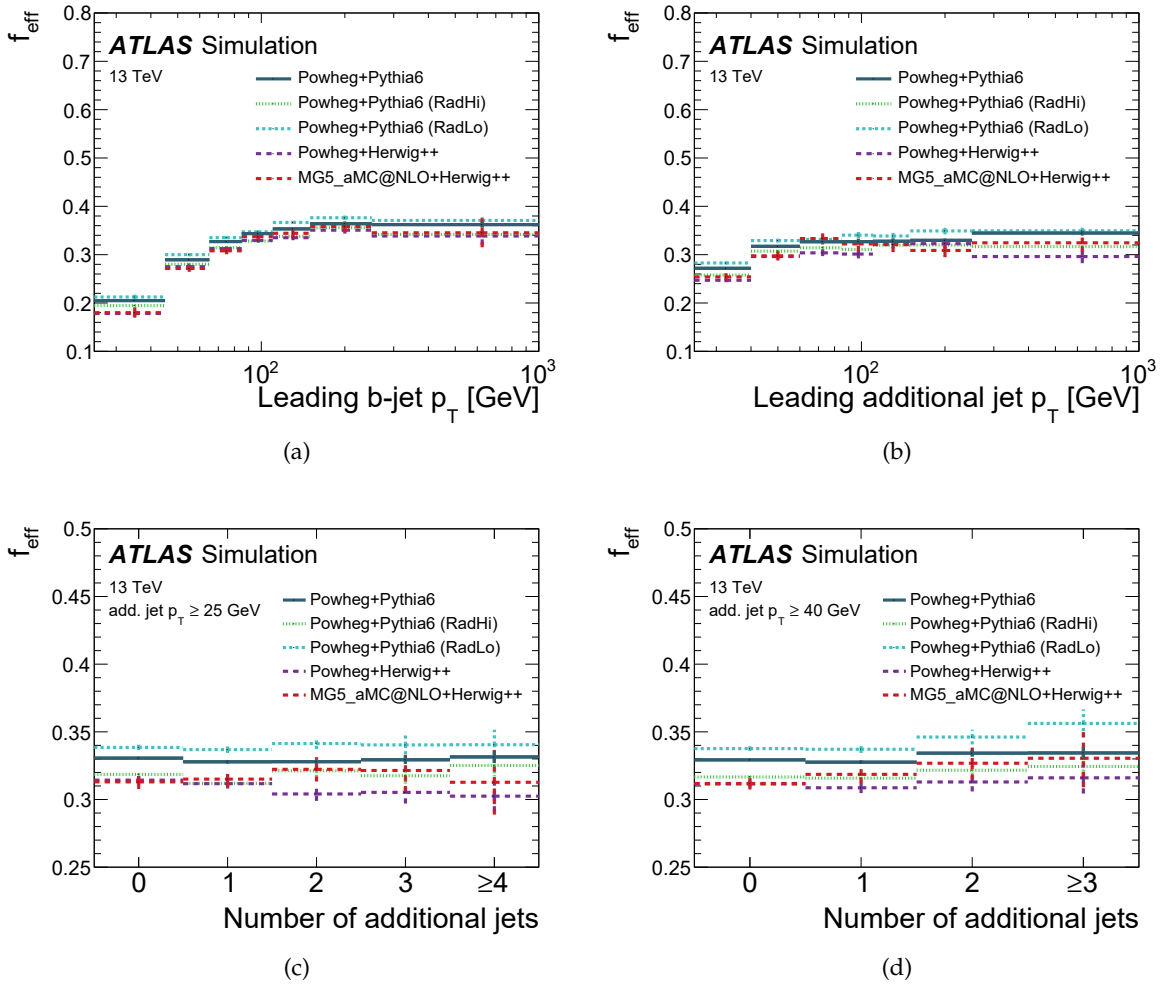

Figure 9.4.: Efficiency correction as defined in Equation 9.4 for (a) leading b-jet p_{T}, (b) leading additional jet p_{T}, (c) jet multiplicity with $p_{\mathrm{T}} > 25$ GeV and (d) $p_{\mathrm{T}} > 40$ GeV at particle level. The distributions are shown with statistical uncertainties only. The blue solid line represents the corrections from the baseline Powheg+PYTHIA 6 MC, the distributions from other MCs are overlaid just for reference.

9.4. Validation of the unfolding procedure

In this thesis additional observables as defined in Section 5.3 are unfolded, that were not published in [66]. In the following the unfolding procedure is validated based on these additional observables.

9.4.1. Stability of the unfolding procedure

The stability of the unfolding method is checked by a so-called *closure test* using MC simulation. In order to test the dependence of unfolding on the statistical power of the data, the statistical uncertainty obtained by the unfolding procedure is compared with the actual statistical variation. The test is performed using pseudo-experiments with the same statistical power as the data to ensure that the closure test appropriately measures the stability.
In this thesis test, 10000 pseudo-experiments are used, that were generated from Gaussian sampling parametrising the reconstruction level distribution of the baseline
Powheg+PYTHIA 6 $t\bar{t}$ sample. Each pseudo-experiment is chosen, so the number of events is equal to that of data. The extra jet distributions from each pseudo-experiment are then unfolded. Each unfolded distribution is compared to the truth distribution obtained from the full sample of events used to train the migration matrix.
The stability is checked through pull distributions, that is defined as:

$$p^i = \frac{N^i_{unfold} - N^i_{part}}{\sigma_{N^i_{unfold}}}, \tag{9.5}$$

where N^i_{unfold} refers to the number of entries in bin i after unfolding the distribution at reconstruction level and $\sigma_{N^i_{unfold}}$ is the error on the unfolded distribution in bin i obtained from the standard deviation of the Gaussian fit to the pull distribution. N^i_{part} is the number of entries in bin i at particle level. Therefore any deviation from zero in the pull p^i could indicate a potential bias from the unfolding method in units of standard deviations on the measured value. The width of the pull is expected to be one, which indicates that the unfolding correctly estimates the statistical uncertainties.
The pull distributions in Figures 9.5 and 9.6 are estimated from the reconstruction level distribution from each pseudo-experiment of the baseline Powheg+PYTHIA 6 MC. The correction factors and response matrix used in the unfolding (see Equation 9.2) are obtained from the same MC simulation. The uncertainty on the unfolding method is obtained from the mean value of the error from 10000 unfolded distributions (blue band), where the error from an individual experiment comes from the covariance matrix of the unfolding (red band).
No significant bias is visible which confirms the applicability of the method for this analysis. The uncertainties on the pull distribution range from 0.95 to 1.0. The bias with respect to the truth particle-level distribution is small and is well within the error on the pull distribution.

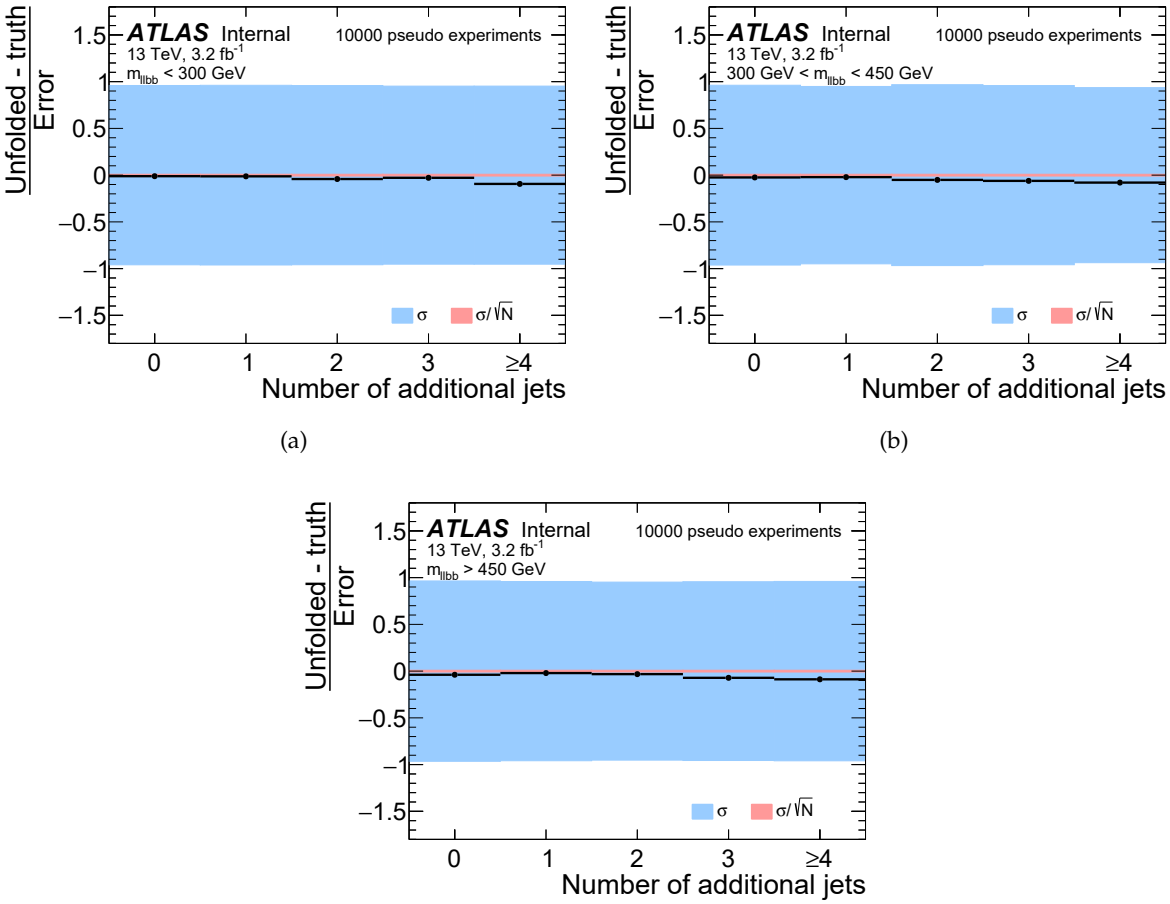

(a) (b)

(c)

Figure 9.5.: Pull distributions as defined in Equation 9.5 for the jet multiplicity in different m_{llbb} regions: (a) $m_{\text{llbb}} < 300$ GeV, (b) 300 GeV $< m_{\text{llbb}} < 450$ GeV and (c) $m_{\text{llbb}} > 450$ GeV. The uncertainty on the unfolding method is obtained from mean value of the error from 10000 unfolded distributions (blue band), where the error from an individual experiment comes from the covariance matrix of the unfolding (red band).

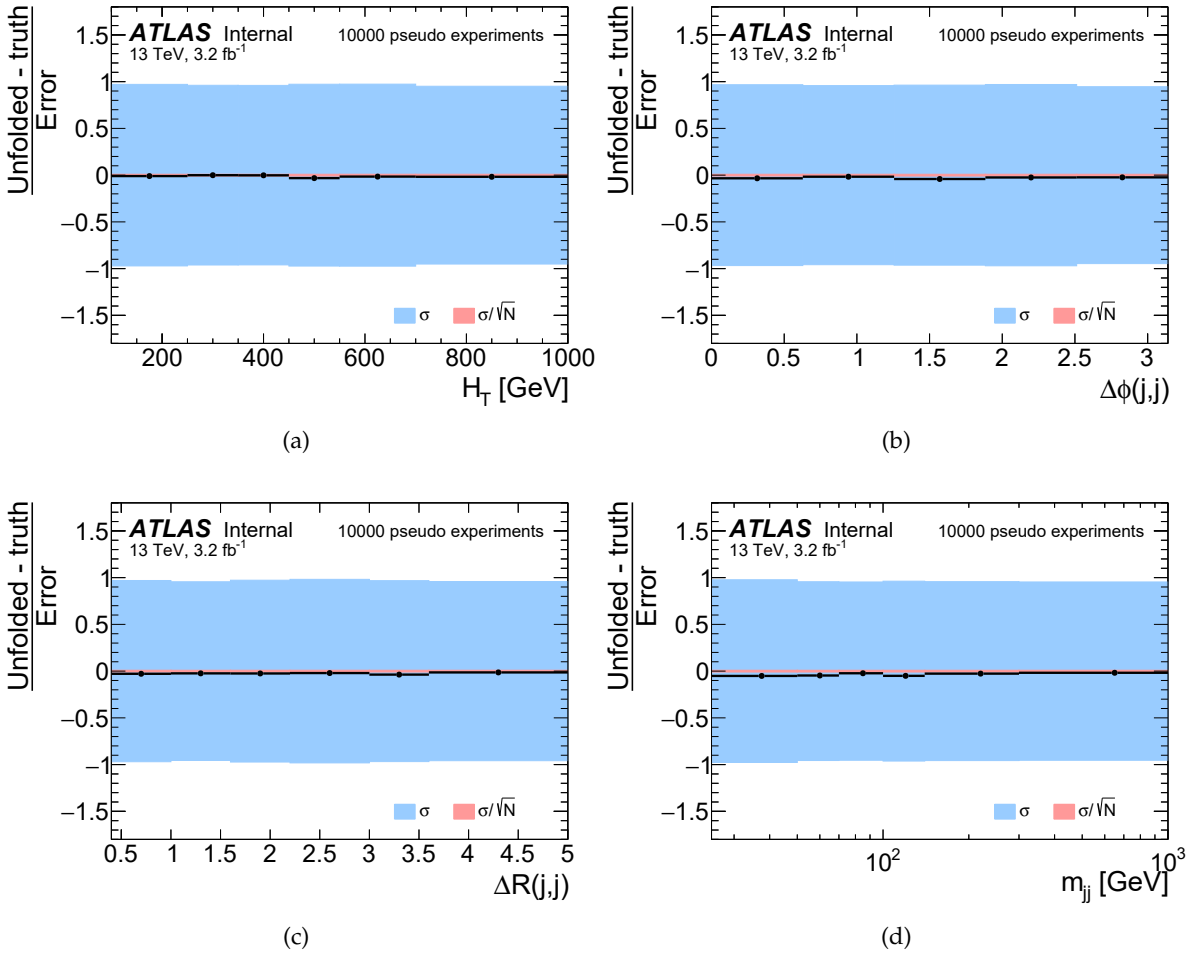

Figure 9.6.: Pull distributions as defined in Equation 9.5 for (a) H_{T}, (b) $\Delta\phi(\mathrm{j},\mathrm{j})$, (c) $\Delta R(\mathrm{j},\mathrm{j})$ and (d) m_{jj}. The uncertainty on the unfolding method is obtained from mean value of the error from 10000 unfolded distributions (blue band), where the error from an individual experiment comes from the covariance matrix of the unfolding (red band).

9.4.2. Prove of concept

In order to prove that the unfolding concept is valid, a so-called *stress test* is done. Stress tests are used to check the stability of the unfolding procedure against changes in the input spectra at reconstruction level by unfolding distributions from alternative theoretical predictions while using the same response matrix and correction factors obtained from the baseline Powheg+PYTHIA 6 MC.
Ten thousand pseudo-experiments are constructed by reweighting the reconstruction level distributions in the baseline MC sample. The weight for each bin is evaluated by the ratio of the particle level distributions from an alternative generator to the baseline. This procedure isolates the uncertainty associated with the choice of the spectrum from other generator-independent sources of instability (e.g. JES), which are accounted for separately.
The relative difference between the unfolded distribution and the particle level distribution is calculated by:

$$b^i = \frac{N^i_{unfold} - N^i_{part}}{N^i_{part}}, \tag{9.6}$$

where N^i_{unfold} refers to the number of entries in bin i after unfolding and N^i_{part} is the number of entries in bin i from the particle level distribution. This measure is called bias. The bias of each pseudo-experiment is fitted with a Gaussian. The mean value of the fit represents the bias for the particular MC generator, while the width of the fitted Gaussian gives an estimate for the error.
The described stress test has been performed for three alternative $t\bar{t}$ MC:
Powheg+PYTHIA 8, Sherpa v2.2 and MadGraph5_aMC@NLO+Herwig++. Figure 9.7 shows the bias for jet multiplicities in different m_{llbb} regions. The bias falls within the one sigma error contour of the fit even for large shifts from Sherpa v2.2 and MadGraph5_aMC@NLO+Herwig++. In Figure 9.8, which shows the bias for H_{T}, $\Delta\phi(\mathrm{j},\mathrm{j})$, $\Delta R(\mathrm{j},\mathrm{j})$ and m_{jj}, larger fluctuations are visible. The unfolding procedure fails to unfold the second bin of $\Delta R(\mathrm{j},\mathrm{j})$ spectrum obtained from MadGraph5_aMC@NLO+Herwig++. In general all spectra from MadGraph5_aMC@NLO+Herwig++ show significant shifts which result in fluctuations in the bias distribution. Therefore MadGraph5_aMC@NLO+Herwig++ is used to obtain systematic uncertainties on the MC modelling, see Chapter 10.

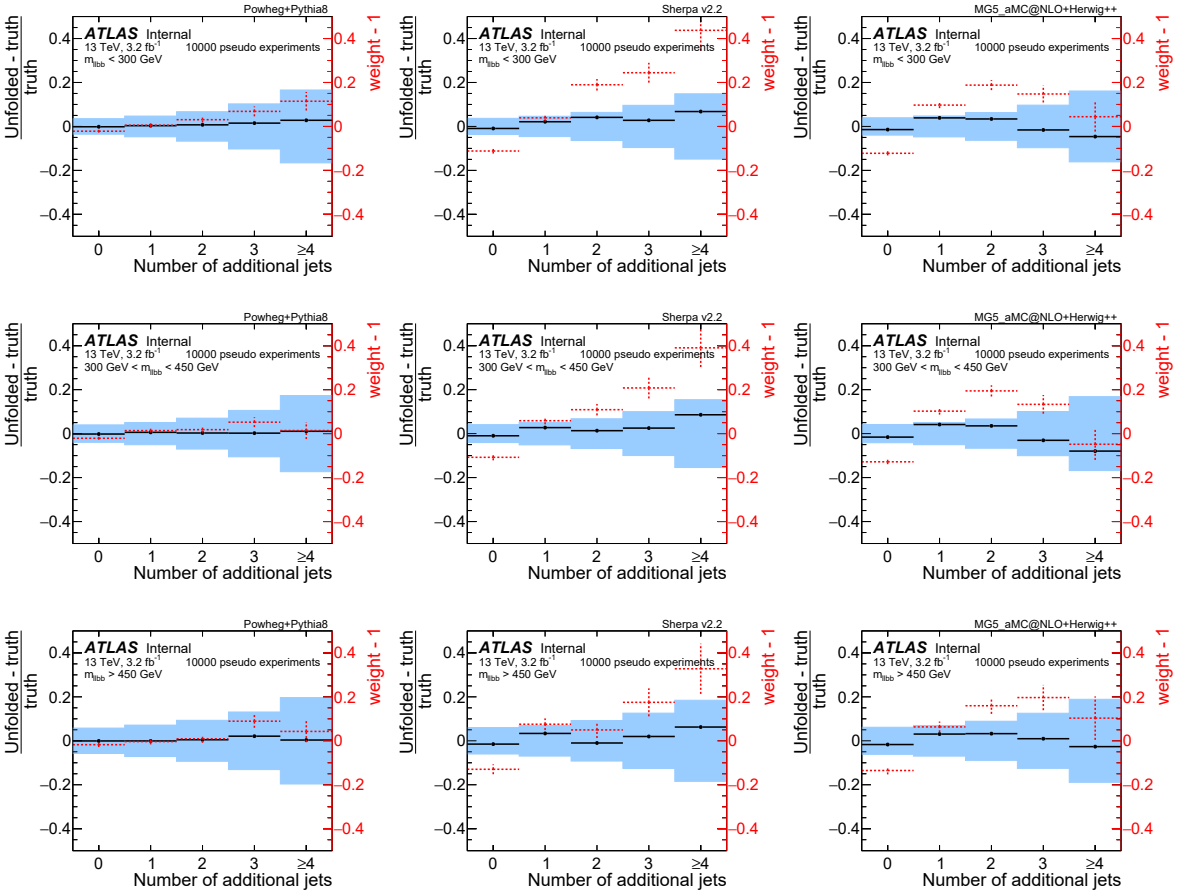

Figure 9.7.: Bias distributions representing the stress test as defined in Equation 9.6 for the jet multiplicity in different m_{llbb} regions: (a-c) m_{llbb} < 300 GeV, (d-f) 300 GeV < m_{llbb} < 450 GeV and (g-i) m_{llbb} > 450 GeV. The input distributions are reweighted based on Powheg+PYTHIA 8 (left), Sherpa v2.2 (middle) and MadGraph5_aMC@NLO+Herwig++ (right). The red points visualise the shift (weight-1) from the reweighting, where the weight is the ratio of distributions in the alternative models and Powheg+PYTHIA 6 at the particle level. The black points represent the mean of the Gaussian fit to the bias distribution from 10000 pseudo-experiments and blue band represents the width of the Gaussian.

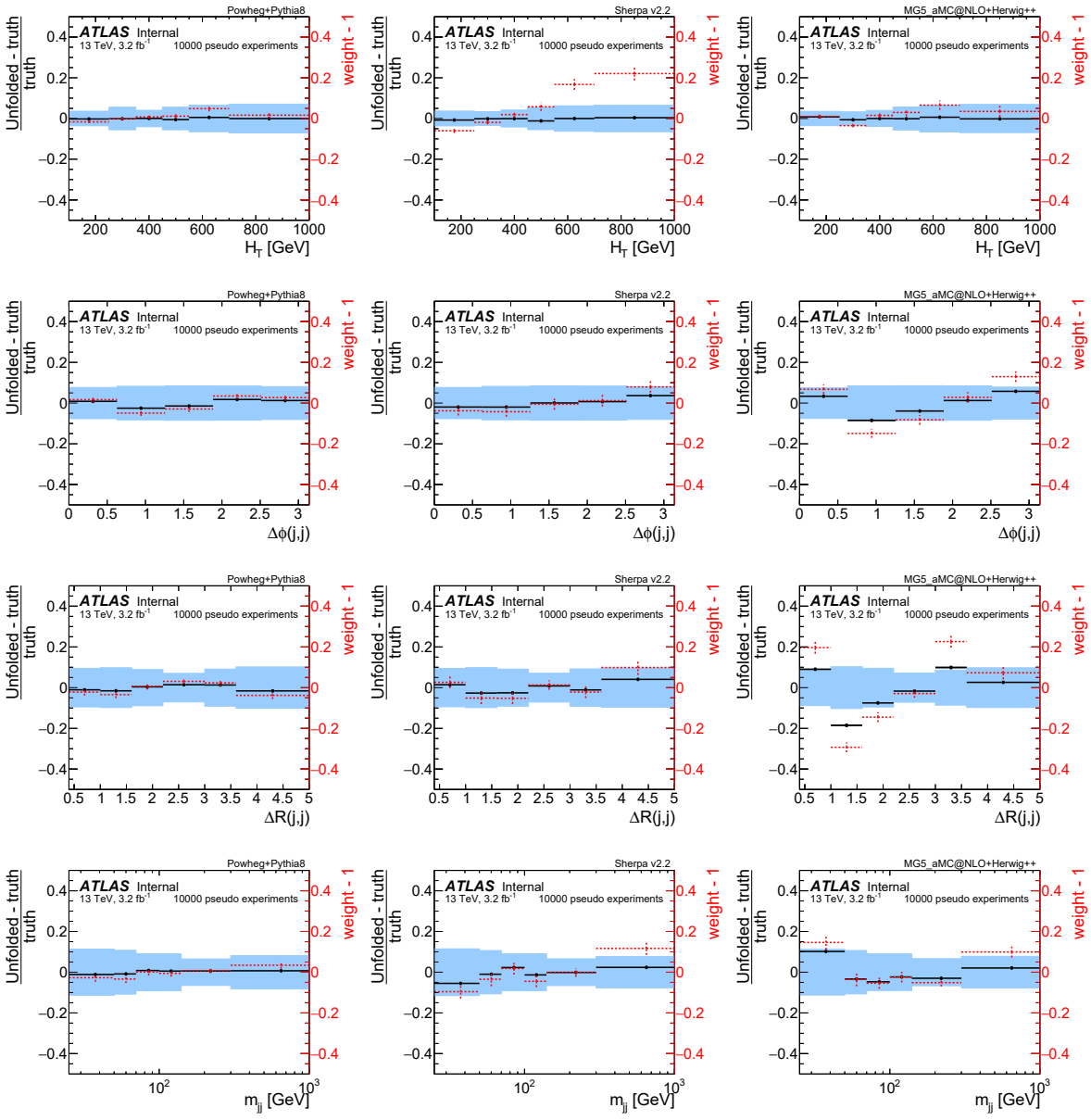

Figure 9.8.: Bias distributions representing the stress test as defined in Equation 9.6 for (a-c) H_{T}, (d-f) $\Delta\phi(\mathrm{j},\mathrm{j})$, (g-i) $\Delta R(\mathrm{j},\mathrm{j})$ and (j-l) m_{jj}. The input distributions are reweighted based on Powheg+PYTHIA 8 (left), Sherpa v2.2 (middle) and MadGraph5_aMC@NLO+Herwig++ (right). The red points visualise the shift (weight-1) from the reweighting, where the weight is the ratio of distributions in the alternative models and Powheg+PYTHIA 6 at the particle level. The black points represent the mean of the Gaussian fit to the bias distribution from 10000 pseudo-experiments and blue band represents the width of the Gaussian.

10. Sources of systematic uncertainties

The measured differential cross sections are affected by several sources of systematic uncertainties that impact the precision. In this chapter the estimation of systematic uncertainties related both to detector effects and to the modelling of the signal and background MC components are detailed.
Each of the systematic uncertainties is evaluated after the unfolding procedure. The evaluation of systematic uncertainties in the unfolded distribution is done by varying the considered distribution at reconstruction level by one standard deviation on the total effect generated by the considered uncertainty. Each varied distribution is unfolded using corrections from the baseline $t\bar{t}$ sample, and the unfolded distribution is compared to the particle-level distribution. Usually, this procedure results in two shifted distributions (up and down variation), each of one representing a shift to the nominal distribution. However, some of the uncertainties have only a single variation; in this case, the uncertainty is evaluated by symmetrising the single deviation. This evaluation of the systematics uncertainties is performed for each observable independently after the event selection and the unfolding procedure.
The total uncertainty is calculated as the square root of the quadratic sum of the components assuming that they are uncorrelated. Except where otherwise indicated, individual systematic uncertainties are assumed to be uncorrelated.

10.1. Detector level uncertainties

Detector modelling uncertainties are evaluated by unfolding the observables with the procedure as described in Chapter 9, where scale factors are varied within their systematic uncertainties. The difference between the unfolded distributions with and without varied scale factors is taken as uncertainty on the final result.
Jet-related uncertainties, primarily the jet energy scale, are the biggest source of detector modelling uncertainty. Other detector related systematics are leptons identifications, triggers and b-tagging efficiencies.

Electron uncertainties: The electron energy scale uncertainties are evaluated using studies of the $Z \to ee$ invariant mass distributions at $\sqrt{s} = 8$ TeV, supported by studies of $J\psi \to ee$ decays [99]. The electron reconstruction efficiency uncertainty is extrapolated from uncertainties derived for results at 8 TeV. The effect of electron reconstruction efficiency is negligible. The electron trigger efficiency and its uncertainty is based on tag-and-probe techniques on $Z \to ee$ decays in early 2015 data. These values are applied as scale factors on top of the simulation trigger efficiency predictions.

Muon uncertainties: The uncertainties on trigger efficiency, muon identification and momentum scale/smearing are evaluated using $Z \to \mu\mu$ decays in the $\sqrt{s} = 13$ TeV early data. The momentum smearing uncertainty has two components; one from the muon spectrometer (MS) and one from the inner detector (ID) both are taken into account. The effect

of the trigger efficiency systematic is at the per-mile level and can be neglected compared to other uncertainties.

Jet uncertainties: Regarding the uncertainties related to the jets, the jet energy scale uncertainties are evaluated using the 2012 final measurement and are extrapolated to $\sqrt{s} = 13$ TeV data [100]. Each of the 19 nuisance parameters, see Section 7.2.2, is independently varied and the uncertainty on the final result is evaluated. The JES uncertainty is 5.5% for jets with p_{T} of 25 GeV and quickly decreasing with increasing jet p_{T}. It is below 2% for jets above 80 GeV.
Also, the jet energy resolution (JER) uncertainty is based on measurements of the jet response in data and is smeared depending on the jet p_{T} and η. This method is only able to increase the resolution. Thus the resulting uncertainty is symmetrised. It is found to be maximal 3.5% at p_{T} of 25 GeV and quickly decreases with increasing jet p_{T} to below 2% for jets above 50 GeV.

JVT uncertainty : The efficiency of the JVT cut and its uncertainty (about 3%) [101] is derived using events of Z-Boson production with additional jets using the method explained in [96]. In order to cover potential differences due to different event topologies in top pair production events, the efficiency of the JVT cut has been determined in the events used for this analysis.

***b*-tagging:** The systematic uncertainties associated with *b*-tagging are divided into three categories, the efficiency for tagging *b*-jets, the efficiency of jets which are originated from *c*-quark but pass the *b*-tag requirements (*c*-quark tagging efficiency) and the efficiency for tagging light quark jets.
All three efficiencies are parametrised as a function of p_{T} and η. In each of these categories, scale factors to correct for the residual difference between data and simulation are used.
This uncertainty is expected to be independent of the jet multiplicity as shown in the 7 TeV analysis [2].

pile-up reweighing: The distributions are varied within the uncertainties on the pile-up weights. The difference between the final unfolded distributions and the nominal result is taken as systematic uncertainty for the pile-up reweighting.

10.2. Signal modeling uncertainties

The uncertainties on the $\mathrm{t\bar{t}}$ modelling take four major differences among available MC generators into account, which are discussed in the following.

Matrix element calculation uncertainty: The uncertainty due to the integrated effects of using a different NLO MC model is evaluated by unfolding the distributions from MadGraph5_aMC@NLO+Herwig++ samples with corrections and migration matrix determined from Powheg+Herwig++ MC. The unfolded spectrum of the MadGraph5_aMC@NLO+Herwig++ sample is compared to the particle level distribution of the Powheg+Herwig++ MC. The difference is used as the systematic uncertainty of the hard scatter generation modelling.

Parton shower and hadronisation model uncertainty: For the parton shower and hadronisation model uncertainty, the distributions from Powheg+Herwig++ samples are unfolded with the baseline MC. The corrections and response matrices are taken from the baseline MC sample. The unfolded result is compared to the particle level distribution of Powheg+Herwig++ and the difference is used as the systematic uncertainty of the parton shower.

ISR and FSR uncertainty: For ISR and FSR the reconstruction level distributions from RadLo and RadHi samples, see Section 4.2.1, are unfolded with corrections and response matrices taken from the baseline MC sample. The difference between the unfolded spectrum and the particle level distribution of the RadLo and RadHi sample is used as the systematic uncertainty of ISR and FSR.

PDF uncertainty: The uncertainty due to the parton distribution function (PDF) is evaluated by using a MadGraph5_aMC@NLO+Herwig++ $t\bar{t}$ sample. The events are reweighted by applying the PDF variations from 100 eigenvectors of the PDF4LHC set [102]. The choice of different PDF variation has an impact on the efficiency, acceptance and also the response matrix. Using these corrections, the central MadGraph5_aMC@NLO+Herwig++ distribution is unfolded. The relative difference is computed with respect to the expected central particle-level spectrum. The total uncertainty is obtained by adding these relative differences in quadrature. Also, the difference between the central PDF4LHC15 and CT10/CT14 is evaluated similarly and added in quadrature to the PDF uncertainty.

10.3. Background uncertainties

In this section, the systematic uncertainties affecting the backgrounds evaluated with MC simulations are shown. The uncertainties on the background modelling are evaluated using the baseline $t\bar{t}$ simulation by varying the background, which is subtracted from data in the unfolding procedure. The difference between the unfolded distributions with varied background and default background is taken as the uncertainty on the final result.

Single top: A systematic uncertainty is estimated by comparing the unfolded distributions where either the diagram removal or the default procedure, the diagram subtraction [53] is used. An additional uncertainty on the shape is considered negligible due to the small contribution to the overall background (see Table 8.2).

Diboson: The shape and normalisation are estimated by comparing the Sherpa prediction with that of Powheg+PYTHIA 8 [95]. A relative difference of 50% was found and considered as systematic uncertainty on the normalisation. In the unfolding algorithm, the diboson background is scaled up by 0.5 and compared to the unscaled background to get the uncertainty on the final result.

Drell-Yan: For Z/γ+jets backgrounds, the scale factor derived in the ee and $\mu\mu$ channels are varied by 20%, corresponding to the difference in the scale factors derived in subsamples with and without an additional jet, see 8.2.1. This value covers the variations of the correction factor derived from subsets of events with different jet multiplicities. An alternative unfolded distribution is estimated by scaling the Z/γ+jets background by 0.2 up to get the uncertainty on the final result. No theoretical uncertainty is applied to the Drell-Yan background normalisation as this is scaled to data.

Misidetified leptons: As described in Section 8.2.2, the systematic uncertainty on the prediction from MC is taken to be 100 % for fake lepton backgrounds. The background scaled by a factor of two is used to get the uncertainty on the final result.

11. Results

This chapter presents the final, fully corrected results of the analysis described in the previous chapters. The measured normalised differential cross sections as a function of jet multiplicity, leading b-jet and additional jet p_{T} at particle level are compared with several MC predictions. In Section 11.3 the additional cross section measurements as a function of H_{T}, $\Delta\phi(\mathrm{j},\mathrm{j})$, $\Delta R(\mathrm{j},\mathrm{j})$, m_{jj} and jet multiplicities in different m_{llbb} regions as introduced in Section 5.3 are presented. The unfolded data is compared with different MC predictions using χ^2 tests in Section 11.2.

11.1. Unfolded distributions

The unfolded normalised cross sections, which are published in [66], are shown in Figure 11.1 and are compared to different MC predictions. The last bin in Figures 11.1(a) and 11.1(b) shows events with up to three additional jets with p_{T} above 25 GeV exclusively (four jets inclusively) and up to two additional jets with p_{T} above 40 GeV exclusively (three inclusively) respectively. The differential normalised cross sections as a function of leading b-jet and leading additional jet p_{T} are shown in Figures 11.1(c) and 11.1(d).
The data are compared to Powheg and MG5_aMC@NLO matched with different shower generators, namely PYTHIA 8, Herwig++, and Herwig7 and to Sherpa, as shown in Figure 11.2. The MC simulations are within uncertainties, and only slight deviations are visible except Powheg+Herwig7, which deviates significantly from the data for all p_{T} thresholds. The MG5_aMC@NLO predictions agree within 5–10% regardless of which parton shower is used (except Herwig7), and the Powheg predictions vary slightly more. The largest difference is visible when different matrix element but the same parton shower generators have been used . Tables 11.1 to 11.4 list the detailed composition of the systematic uncertainties. The uncertainty on the jet multiplicity distributions rises from 4–5% for one additional jet to up to 20% for the highest jet multiplicity bin. Systematic uncertainties dominate in all measurements. In almost all bins for all p_{T} thresholds, the JES uncertainty dominates, followed by the modelling uncertainty. The statistical uncertainty dominates in almost all bins. The dominant source of systematic uncertainty originates from one of JES/JER, NLO generator modelling or PS/hadronisation. JES/JER is the largest uncertainty in the lowest p_{T} bins of all measurements.

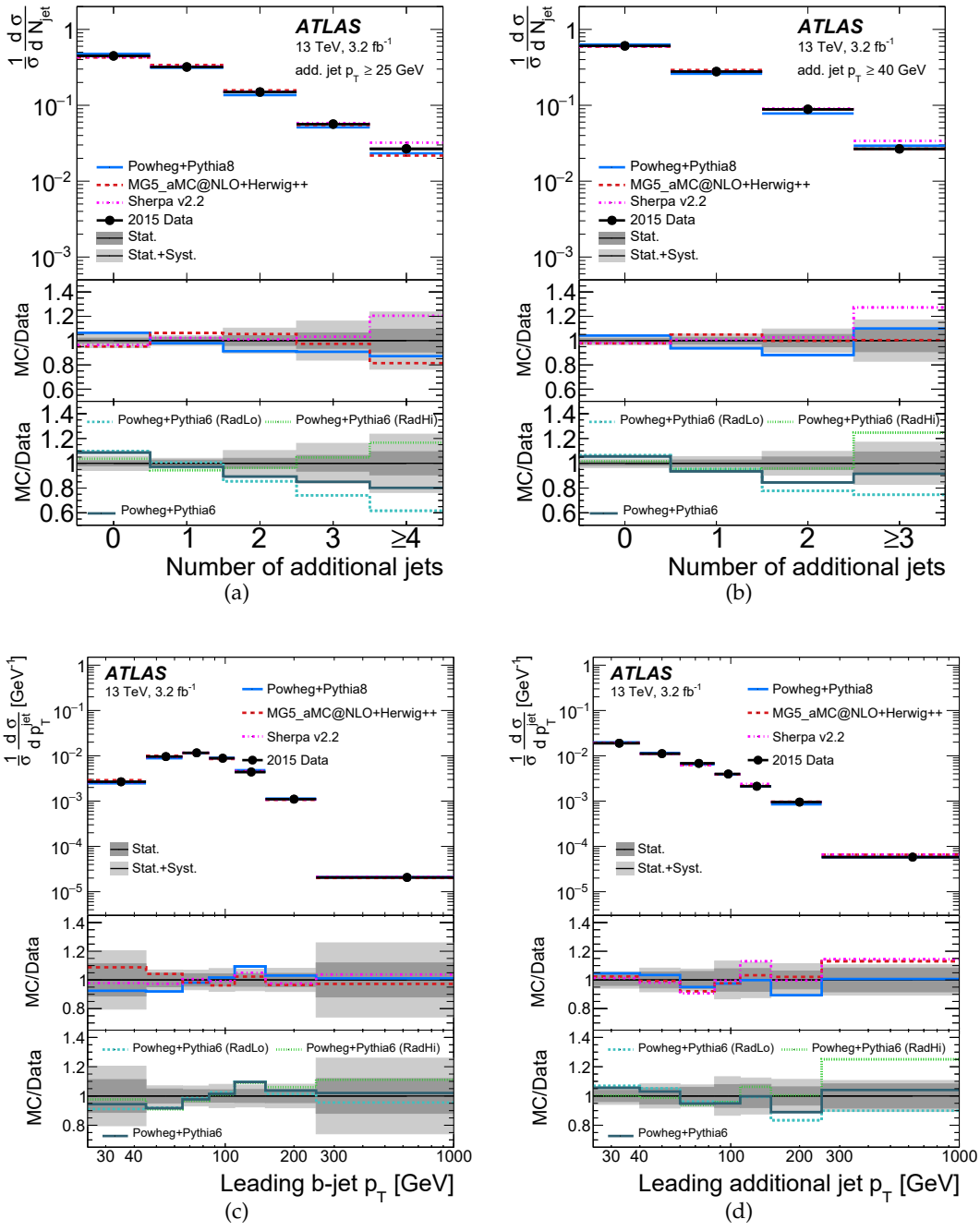

Figure 11.1.: Unfolded distribution for (a) jet multiplicity for additional jet $p_{\mathrm{T}} > 25$ GeV, (b) jet multiplicity for additional jet $p_{\mathrm{T}} > 40$ GeV, (c) leading b-jet p_{T} and (d) leading additional jet p_{T}. Comparison to different MC predictions is shown for these distribution in first panel. The middle and bottom panels show the ratios of different MC predictions of the normalised cross-section to the measurement and the ratios of Powheg+PYTHIA 6 predictions with variation of the QCD radiation to the measurement, respectively. The shaded regions show the statistical uncertainty (dark grey) and total uncertainty (light grey).

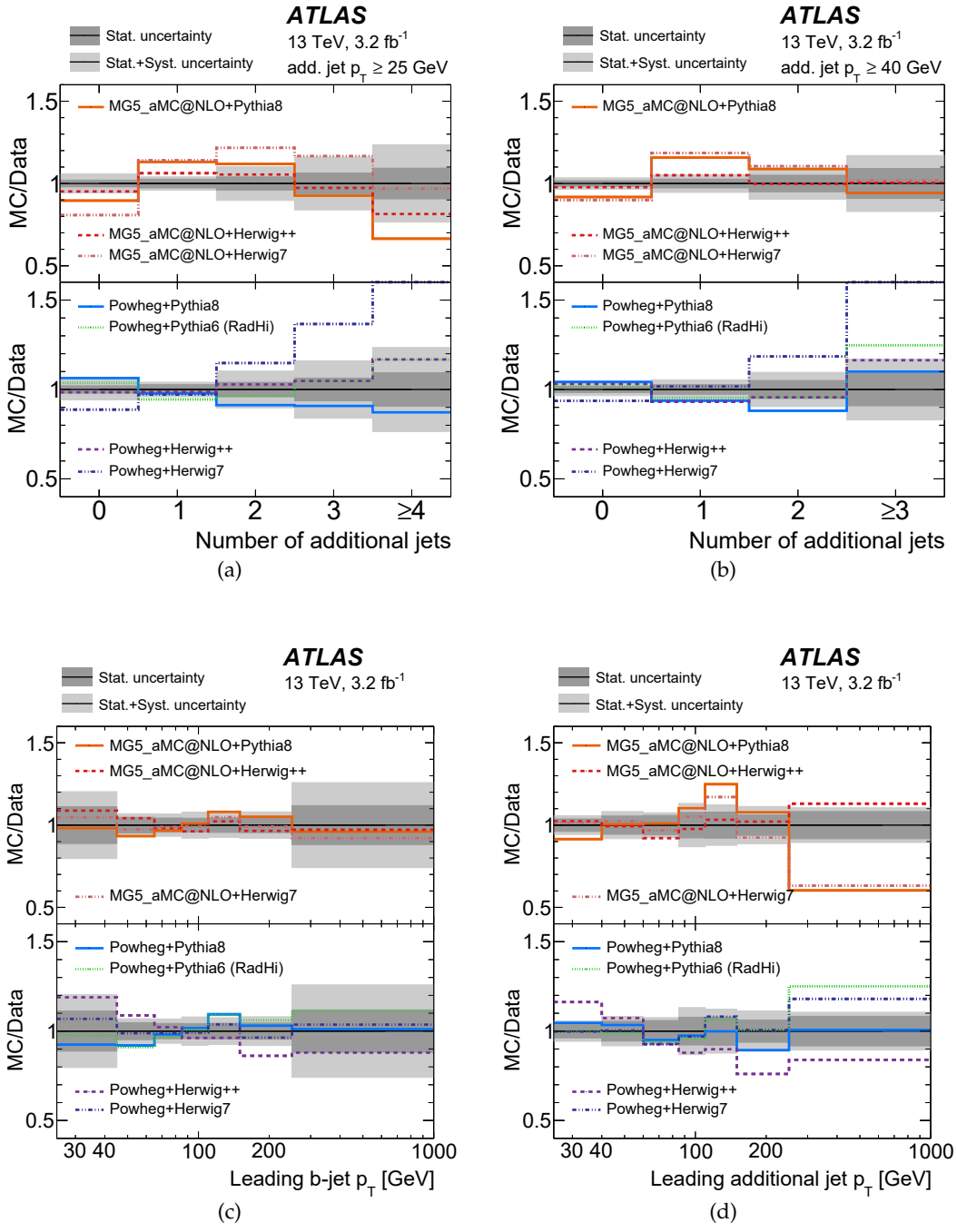

Figure 11.2.: Ratios of different ME + PS generator combinations of the normalised cross-section to the measurement for (a) jet multiplicity for additional jet $p_{\mathrm{T}} >$ 25 GeV, (b) jet multiplicity for additional jet $p_{\mathrm{T}} >$ 40 GeV, (c) leading b-jet p_{T} and (d) leading additional jet p_{T}. The shaded regions show the statistical uncertainty (dark grey) and total uncertainty (light grey).

Relative uncertainty in [%] in additional jets multiplicity					
Sources	0	1	2	3	≥ 4
Data statistics	2.1	2.7	4.0	6.0	9.0
JES/JER	5.0	1.8	7.0	12.0	16.0
b-tagging	0.5	0.2	0.7	1.4	2.0
ISR/FSR modelling	0.4	0.5	2.2	3.8	6.0
Signal modelling	1.9	2.0	5.6	6.0	11.0
Other	1.4	0.9	2.5	3.3	5.0
Total	6.0	4.0	10.0	16.0	24.0

Table 11.1.: Summary of relative uncertainties in [%] for the jet multiplicity measurement using a jet p_{T} threshold of 25 GeV. "Signal modelling" sources of systematic uncertainty includes the hadronisation, parton shower and NLO modelling uncertainties. "Other" sources of systematic uncertainty refers to lepton and jet selection efficiencies, background (including pile-up jets) estimations, and the PDF.

Relative uncertainty in [%] in additional jets multiplicity				
Sources	0	1	2	≥ 3
Data statistics	1.7	2.7	5.0	9.0
JES/JER	2.0	2.5	6.0	9.0
b-tagging	0.3	0.4	1.1	1.8
ISR/FSR modelling	0.2	0.4	3.0	6.0
Signal modelling	2.0	3.7	4.4	9.0
Other	0.7	0.8	1.5	4.1
Total	3.4	5.0	10.0	17.0

Table 11.2.: Summary of relative uncertainties in [%] for the jet multiplicity measurement using a jet p_{T} threshold of 40 GeV. "Signal modelling" sources of systematic uncertainty includes the hadronisation, parton shower and NLO modelling uncertainties. "Other" sources of systematic uncertainty refer to lepton and jet selection efficiencies, background (including pile-up jets) estimations, and the PDF.

Sources	Relative uncertainty in leading b-jet p_{T} [GeV] in [%]						
	25–45	45–65	65–85	85–110	110–150	150–250	> 250
Data statistics	11.0	5.0	4.3	4.2	4.4	5.0	12.0
JES/JER	11.0	2.3	1.3	2.4	3.2	4.2	6.0
b-tagging	6.0	1.1	0.9	1.0	1.9	5.0	14.0
ISR/FSR modelling	6.0	0.9	1.0	2.1	3.1	0.9	0.1
Signal modelling	9.0	2.0	5.0	6.0	2.1	0.4	15.0
Other	4.4	3.0	1.4	1.7	3.0	2.2	10.0
Total	20.0	7.0	7.0	8.0	8.0	8.0	26.0

Table 11.3.: Summary of relative measurement uncertainties in [%] for the leading b-jet p_{T} distribution. "Signal modelling" sources of systematic uncertainty includes the hadronisation, parton shower and NLO modelling uncertainties. "Other" sources of systematic uncertainty refers to lepton and jet selection efficiencies, background (including pile-up jets) estimations, and the PDF.

Sources	Relative uncertainty in leading additional jet p_{T} [GeV] in [%]						
	25–40	40–60	60–85	85–110	110–150	150–250	> 250
Data statistics	3.8	6.0	6.0	8.0	8.0	6.0	8.0
JES/JER	2.9	3.3	2.1	2.7	3.8	3.8	4.2
b-tagging	0.3	0.2	0.6	0.4	0.6	0.4	1.3
ISR/FSR modelling	0.6	1.6	1.4	0.7	2.4	4.0	2.1
Signal modelling	2.5	4.0	3.6	10.0	8.0	8.0	4.0
Other	1.5	2.8	1.8	3.4	2.4	1.6	1.8
Total	6.0	8.0	8.0	13.0	12.0	11.0	11.0

Table 11.4.: Summary of relative measurement uncertainties in [%] for the leading additional jet p_{T} distribution. "Signal modelling" sources of systematic uncertainty includes the hadronisation, parton shower and NLO modelling uncertainties. "Other" sources of systematic uncertainty refers to lepton and jet selection efficiencies, background (including pile-up jets) estimations, and the PDF.

11.2. Statistical comparison

The unfolded data are compared with different MC predictions using χ^2 tests. The χ^2 values are obtained by using full covariance matrices, which are produced from the unfolding including systematic and statistical uncertainties. The χ^2 is calculated using:

$$\chi^2 = S^{\mathrm{T}}_{n-1}\mathrm{Cov}^{-1}_{n-1}S_{n-1} \tag{11.1}$$

where S_{n-1} corresponds to the vector of the difference between the unfolded data and MC generator predictions of the normalised cross-section for one less than the total number of bins in the distribution. Cov_{n-1} is the $(n-1)\times(n-1)$ matrix derived from the full covariance matrix and obtained by discarding the corresponding row or column. The full covariance matrix is singular and non-invertible, as it is evaluated using normalised distributions. From the χ^2 and the $n-1$ degrees of freedom the p- values are evaluated, which relate to the probability that the χ^2 is larger than or equal to the observed value.
χ^2 and p-values are shown in Tables 11.5 and 11.6. In general, a good agreement between data and predictions is observed. However, one can see that the agreement with data is slightly better for MadGraph5_aMC@NLO+Herwig++ compared to
Powheg+Herwig++.
The ratio of the data to predictions of Powheg+PYTHIA 6 with different levels of QCD radiation both in the matrix-element calculation and in the parton shower is also shown. Powheg+PYTHIA 6 (RadLo) does not describe the data well. The central prediction of Powheg+PYTHIA 6 yields fewer jets than in data; however, the predictions are still within the experimental uncertainties. Powheg+PYTHIA 6 (RadHi) describes the data most consistently, which is also confirmed by high p-values for all p_{T} thresholds. The Powheg+PYTHIA 6 (RadLo) sample has p-values around 0.5 and the central sample mostly between 0.8 and 0.9.

	$p_{\mathrm{T}}>25$ GeV		$p_{\mathrm{T}}>40$ GeV	
Generator	χ^2/NDF	p-value	χ^2/NDF	p-value
Powheg+PYTHIA 6	0.82/4	0.94	0.83/3	0.84
Powheg+PYTHIA 8	0.43/4	0.98	0.90/3	0.83
Powheg+Herwig++	0.51/4	0.97	0.88/3	0.83
Powheg+Herwig7	8.62/4	0.07	4.87/3	0.18
MG5_aMC@NLO+PYTHIA 8	5.51/4	0.24	3.10/3	0.38
MadGraph5_aMC@NLO+Herwig++	1.28/4	0.86	0.49/3	0.92
MadGraph5_aMC@NLO+Herwig7	3.14/4	0.54	4.31/3	0.23
Sherpa v2.2	0.43/4	0.98	0.85/3	0.84
Powheg+PYTHIA 6 (RadHi)	1.20/4	0.88	1.06/3	0.79
Powheg+PYTHIA 6 (RadLo)	4.15/4	0.39	2.05/3	0.56

Table 11.5.: Values of χ^2/NDF and p-values between the unfolded normalised cross-section and the predictions for additional-jet multiplicity measurements. The number of degrees of freedom is equal to the number of bins minus one.

Generator	Leading b-jet p_{T}		Leading additional jet p_{T}	
	χ^2/NDF	p-value	χ^2/NDF	p-value
Powheg+Pythia 6	2.24/6	0.90	3.50/6	0.74
Powheg+Pythia 8	1.94/6	0.93	2.28/6	0.89
Powheg+Herwig++	1.95/6	0.92	18.5/6	0.01
Powheg+Herwig7	1.26/6	0.97	1.95/6	0.92
MG5_aMC@NLO+Pythia 8	1.99/6	0.92	10.5/6	0.10
MadGraph5_aMC@NLO+Herwig++	2.03/6	0.92	2.97/6	0.81
MadGraph5_aMC@NLO+Herwig7	1.32/6	0.97	2.31/6	0.89
Sherpav2.2	0.71/6	0.99	4.03/6	0.67
Powheg+Pythia 6 (RadHi)	2.79/6	0.83	1.68/6	0.95
Powheg+Pythia 6 (RadLo)	2.16/6	0.90	3.27/6	0.77

Table 11.6.: Values of χ^2/NDF and p-values between the unfolded normalised cross-section and the predictions for the jet p_{T} measurements. The number of degrees of freedom is equal to one less than the number of bins in the distribution.

11.3. Unfolded distributions of additional observables

Figure 11.3 shows the normalized differential cross-section as function of the jet multiplicity for the m_{llbb} regions $m_{\mathrm{llbb}} < 300$ GeV, 300 GeV $< m_{\mathrm{llbb}} < 450$ GeV and $m_{\mathrm{llbb}} > 450$ GeV. The unfolded distribution for data is compared to several theoretical predictions. All of the generators provide a reasonable description of the jet multiplicity in all m_{llbb} regions within the uncertainties. The total uncertainty ranges from 20% for low extra jet multiplicities to up to 50% for higher jet multiplicities. The statistical is below 10% for all bins except the highest. With more collected data from 2016 and 2017 runs, measurements to higher jet multiplicities are possible since the luminosity for this dataset is ten times larger than the 2015 dataset used in this analysis.
In Figure 11.4 the normalized differential cross-section as function of H_{T}, $\Delta\phi(\mathrm{j},\mathrm{j})$, $\Delta R(\mathrm{j},\mathrm{j})$ and m_{jj} is shown. All theoretical predictions are matching the data quite well. The size of the uncertainty band is about constant for all observables in all bins. The statistical uncertainty contributes to almost 50% to the total uncertainty in some bins. Combined with the fact that the distributions of some generators have different shapes compared to others or data one could expect significantly better results with complete Run-2 data.

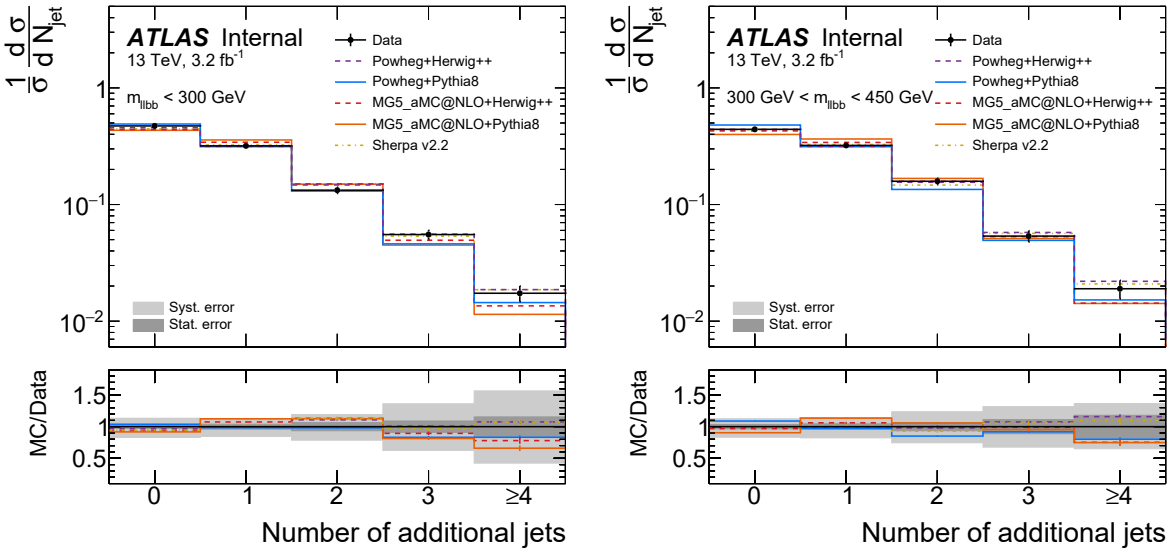

(a)

(b)

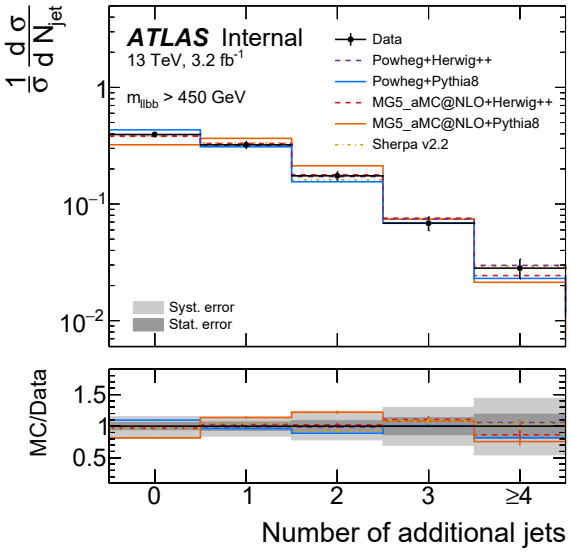

(c)

Figure 11.3.: Distributions of the unfolded jet multiplicity distribution in different m_{llbb} regions for data and simulation. The m_{llbb} regions are (a) $m_{\mathrm{llbb}} < 300$ GeV, (b) 300 GeV $< m_{\mathrm{llbb}} < 450$ GeV and (c) $m_{\mathrm{llbb}} > 450$ GeV. The statistical errors are shown as a dark gray and the total uncertainty (statistical and systematical) are shown as a light gray band.

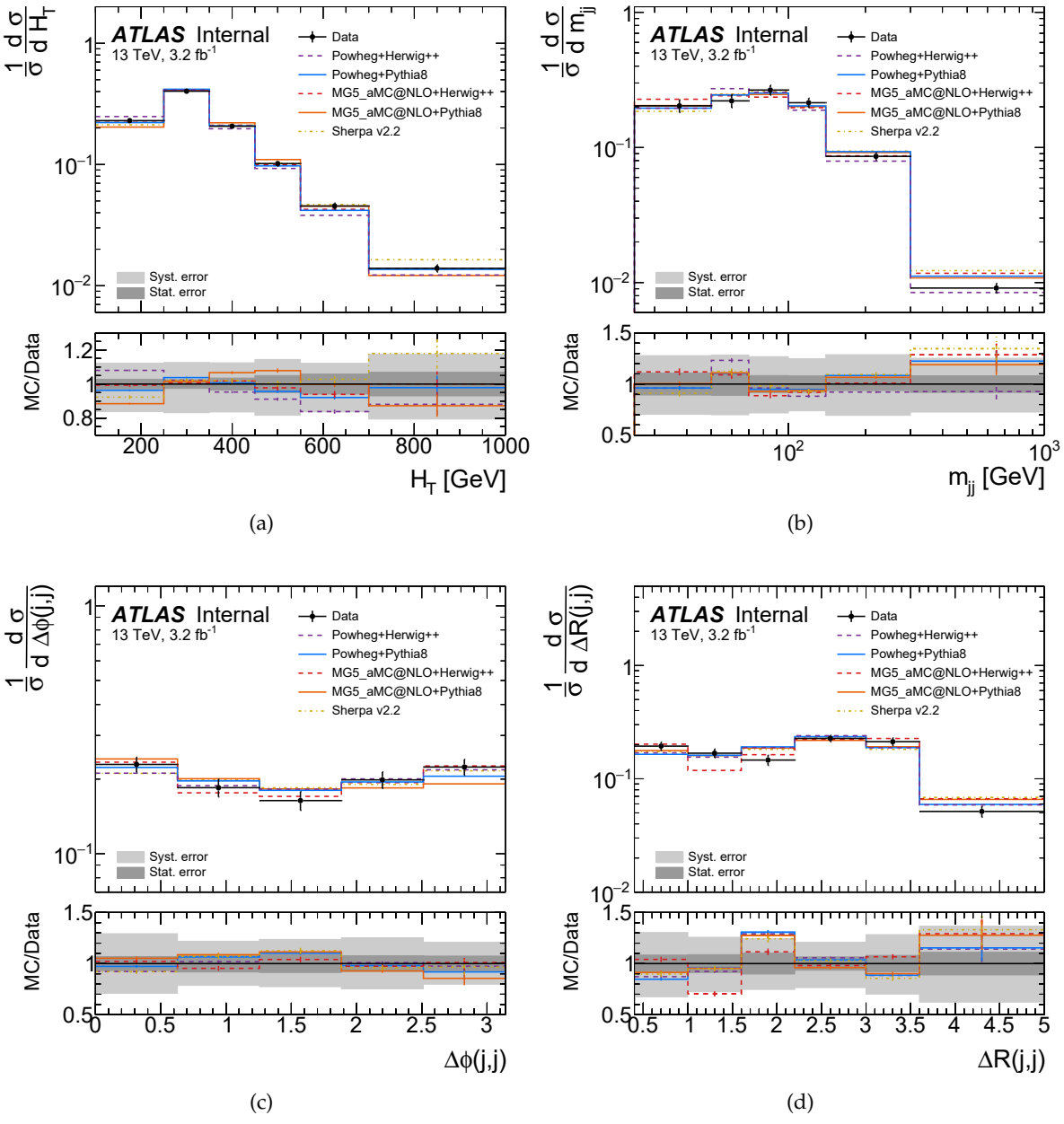

Figure 11.4.: Distributions of the unfolded (a) H_{T}, (b) $\Delta\phi(\mathrm{j},\mathrm{j})$, (c) $\Delta R(\mathrm{j},\mathrm{j})$ and (d) m_{jj} distribution for data and simulation. The statistical errors are shown as a light gray and the total uncertainty (statistical and systematical) are shown as a dark gray band.

12. Conclusions

In this thesis studies of additional jet activity, in the form of differential cross section measurements, have been presented for dileptonic $t\bar{t}$ events identified by having an opposite-sign $e\mu$ pair and at least two b-tagged jets. Due to the large luminosity reached by the LHC, a large number of top quarks get produced, which allows differential cross section measurements of top quark pair production in association with additional jets with very high precision.
The measurements have been performed using 3.2 fb^{-1} of $\sqrt{s} = 13$ TeV $p - p$ collision data collected by the ATLAS Detector in 2015 at the LHC. The measurements were corrected back to the particle level using correction factors and iterative Bayesian unfolding.
The results have been compared with different theoretical predictions used in other ATLAS analyses. The measurements were found to be in generally good agreement with the MC simulations. Powheg+PYTHIA 8 and MadGraph5_aMC@NLO+Herwig++ generators show the best agreement with data, and MadGraph5_aMC@NLO+PYTHIA 8 is generally less favoured. Interestingly, the Powheg+PYTHIA 6 RadHi simulation was usually in better agreement with data than the nominal Powheg+PYTHIA 6 sample.
The predictions of the generators are sensitive to variables such as choice of QCD scale and parton showering parameters, and the precision of these results allows tuning the generators for future measurements, decreasing the amount of parameter variation that must be considered in evaluating simulation uncertainties for future analyses.
The ATLAS detector has collected even more data during 2016 and 2017, which allows performing more precision measurements. The increased sample size helps to reduce statistical uncertainties and the improvement in measurements to derive scale factors, and correction factors will decrease systematic uncertainties, which overall results in a better distinction between measured data and theoretical predictions.
The additional observables developed in this thesis, H_{T} and $\Delta R(\mathrm{j},\mathrm{j})$, got slightly adapted to measure additional b-jets in $t\bar{t}$ events in a measurement performed using 36.1 fb^{-1} of $\sqrt{s} = 13$ TeV $p - p$ collision data collected by the ATLAS Detector during 2015 and 2017 at the LHC [103].

A. Additional background estimation distributions

A.1. Additional Drell-Yan background distributions

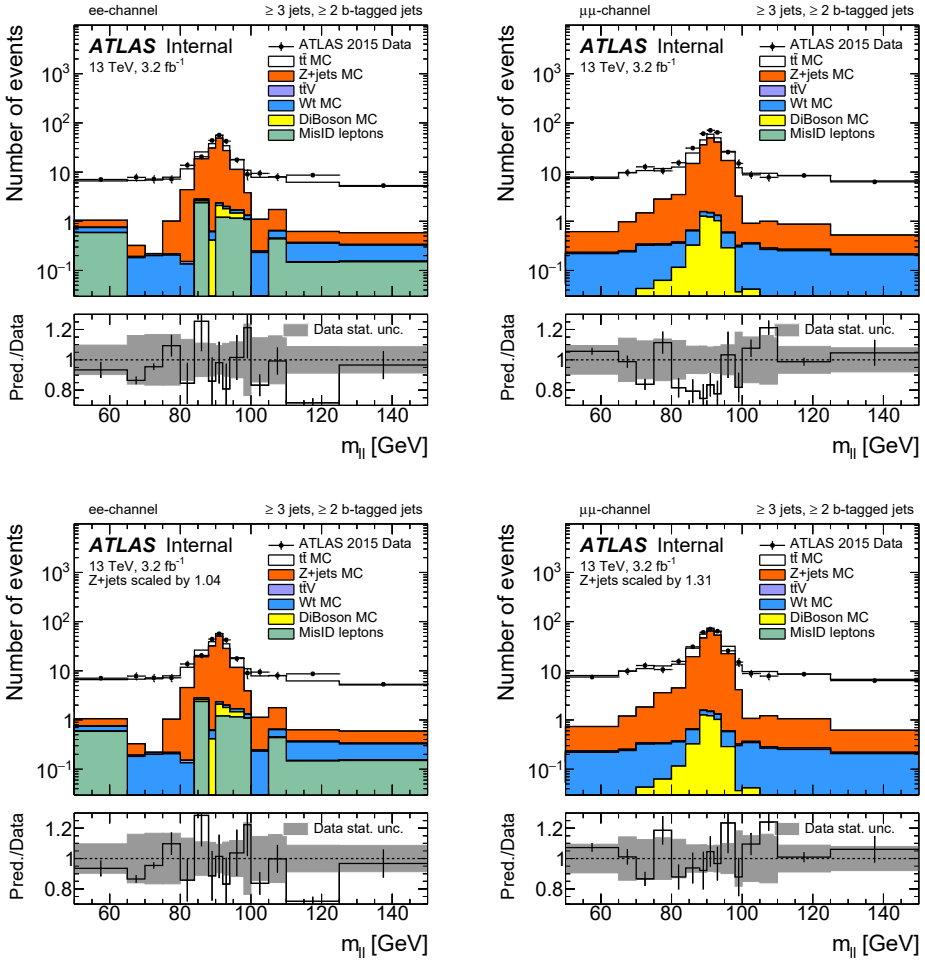

Figure A.1.: Dilepton mass distributions in the same lepton flavour channels with standard selection except dilepton mass cut and requirement of at least one additional jet before applying the normalisation scale factors. Before (a,b) and after (c,d) applying the normalisation scale factors. The area under the the Z peak in (a,b) is used to derive the uncertainty on the normalisation scale factor.

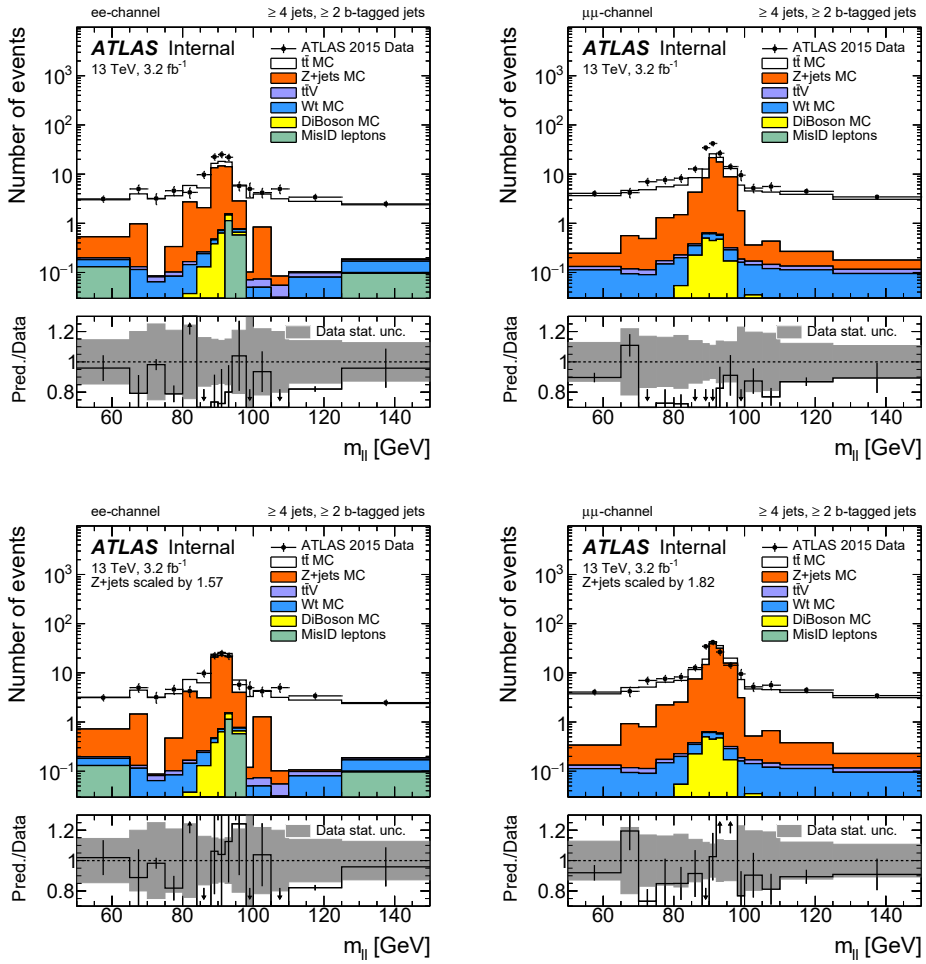

Figure A.2.: Dilepton mass distributions in the same lepton flavour channels with standard selection except dilepton mass cut and requirement of at least two additional jets before applying the normalisation scale factors. Before (a,b) and after (c,d) applying the normalisation scale factors. The area under the the Z peak in (a,b) is used to derive the uncertainty on the normalisation scale factor.

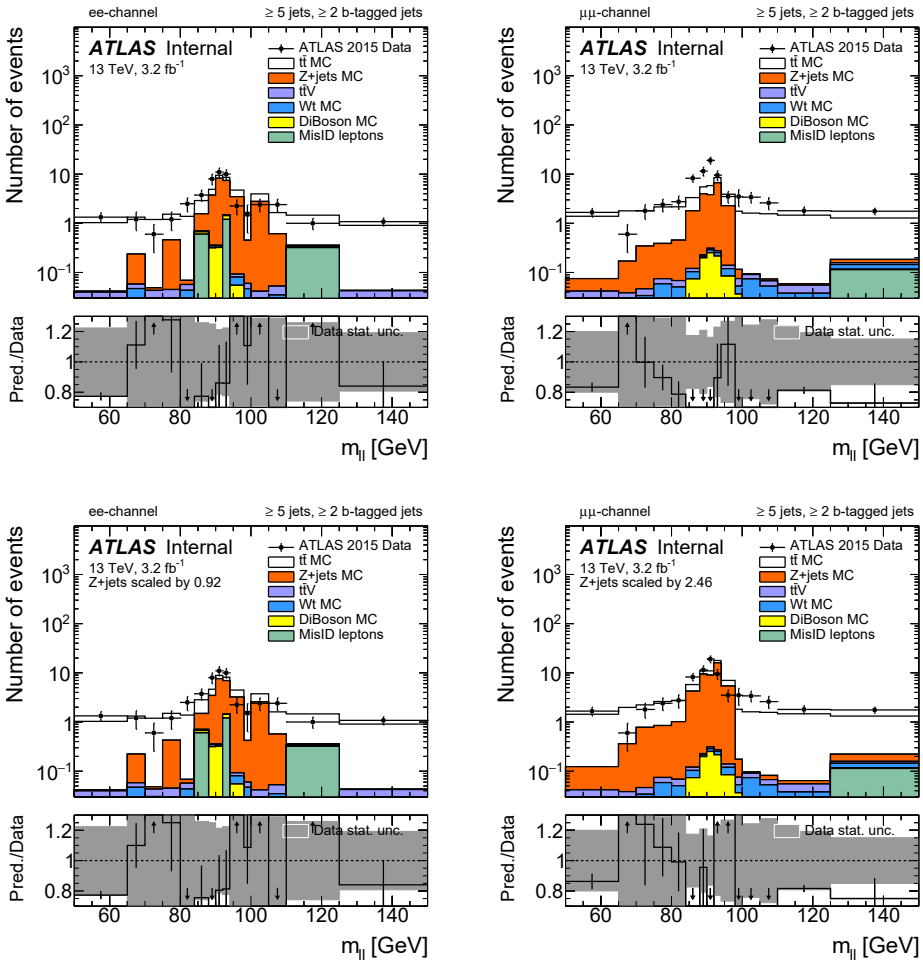

Figure A.3.: Dilepton mass distributions in the same lepton flavour channels with standard selection except dilepton mass cut and requirement of at least three additional jets before applying the normalisation scale factors. Before (a,b) and after (c,d) applying the normalisation scale factors. The area under the the Z peak in (a,b) is used to derive the uncertainty on the normalisation scale factor.

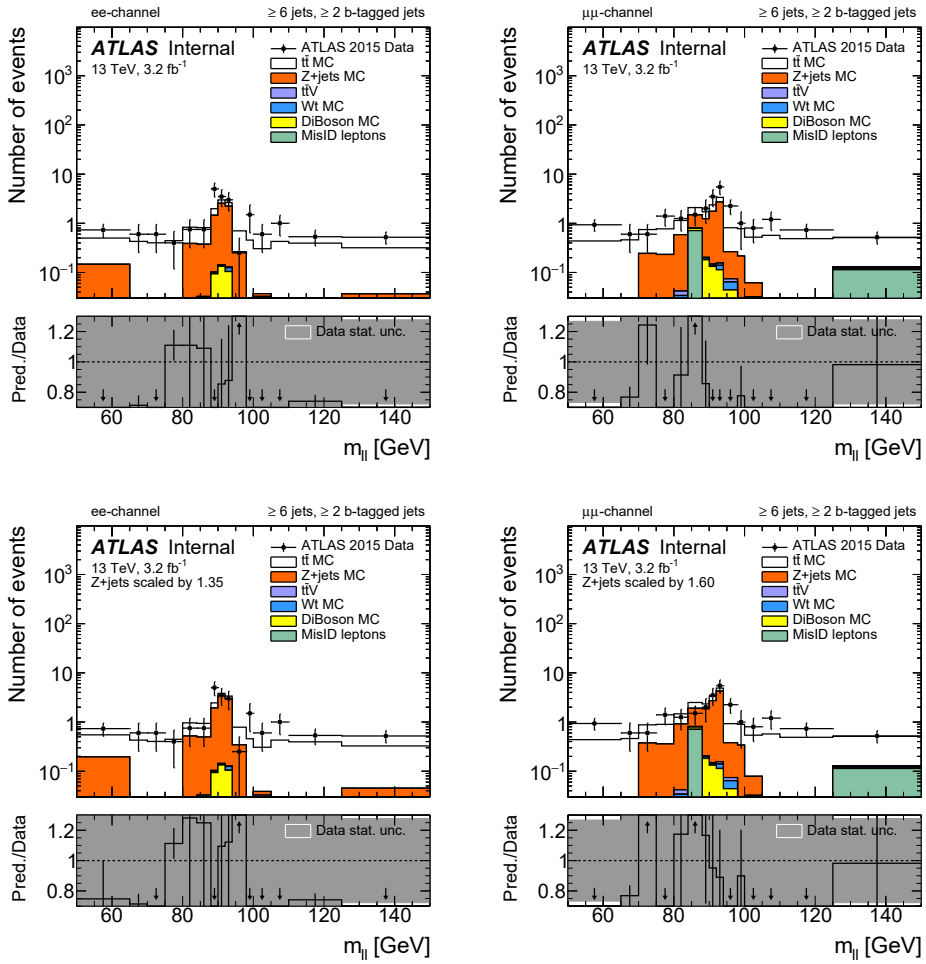

Figure A.4.: Dilepton mass distributions in the same lepton flavour channels with standard selection except dilepton mass cut and requirement of at least four additional jets before applying the normalisation scale factors. Before (a,b) and after (c,d) applying the normalisation scale factors. The area under the the Z peak in (a,b) is used to derive the uncertainty on the normalisation scale factor.

A.2. Additional misidentified leptons distributions

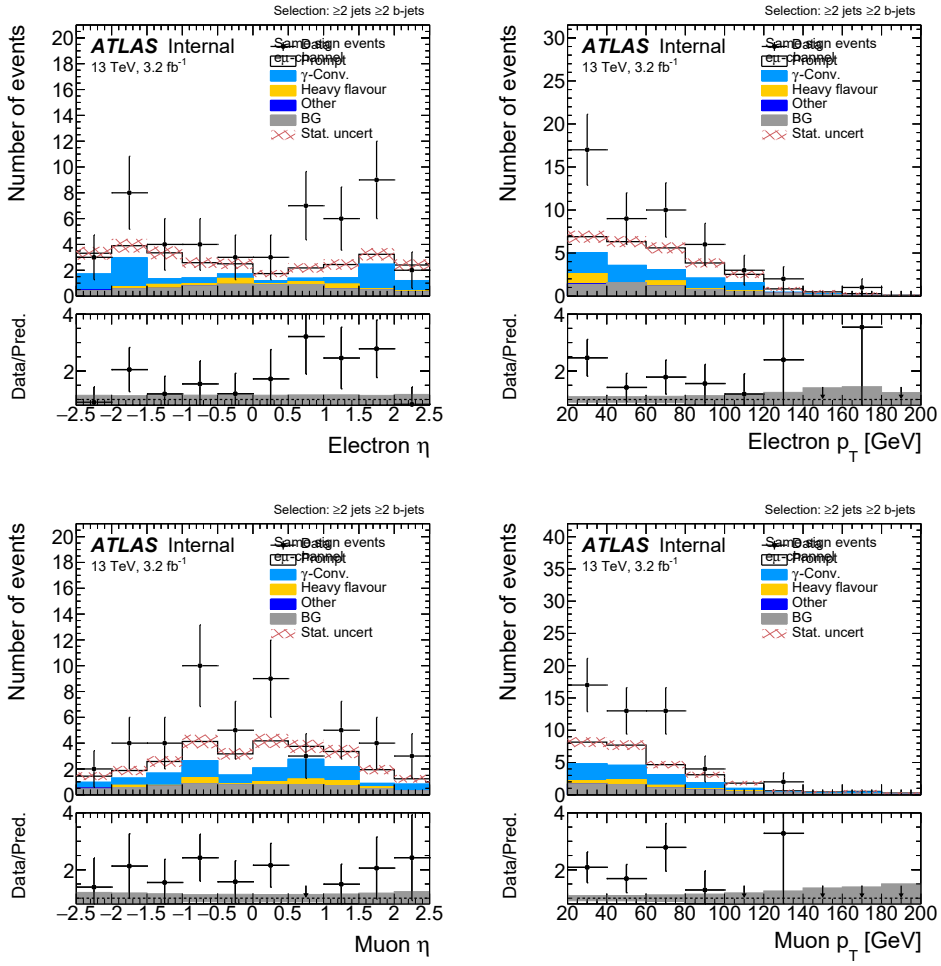

Figure A.5.: Distribution of electron and muon $|\eta|$ and p_T in same-sign eμ events with at least two b-tagged jets. The simulation prediction is broken down into contributions where both leptons are prompt or one is a misidentified lepton from photon conversion or heavy-flavour decay.

B. Additional comparsions between data and Monte Carlo at reconstruction level

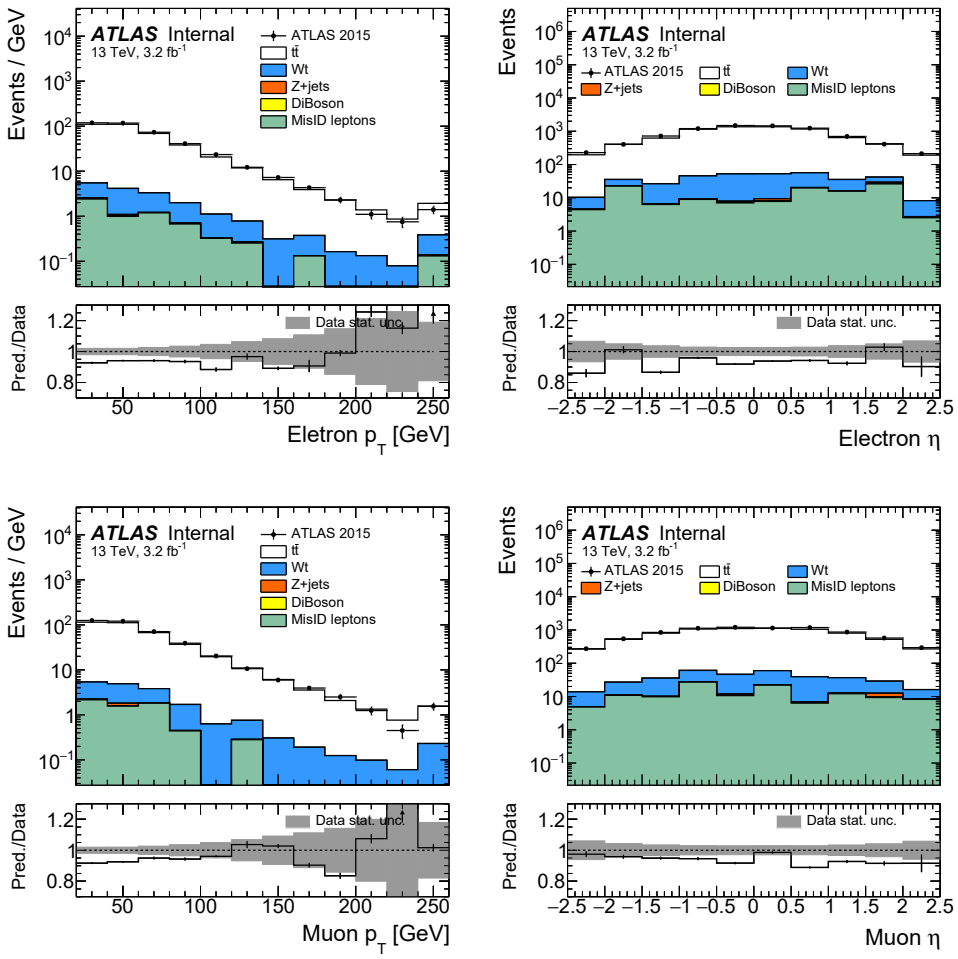

Figure B.1.: Distributions in events fulfilling the standard selection criteria as in Table 8.1 for (a) p_{T} of electron, (b) η of electron, (c) p_{T} of muon and (d) η of muon. Uncertainties are statistical only.

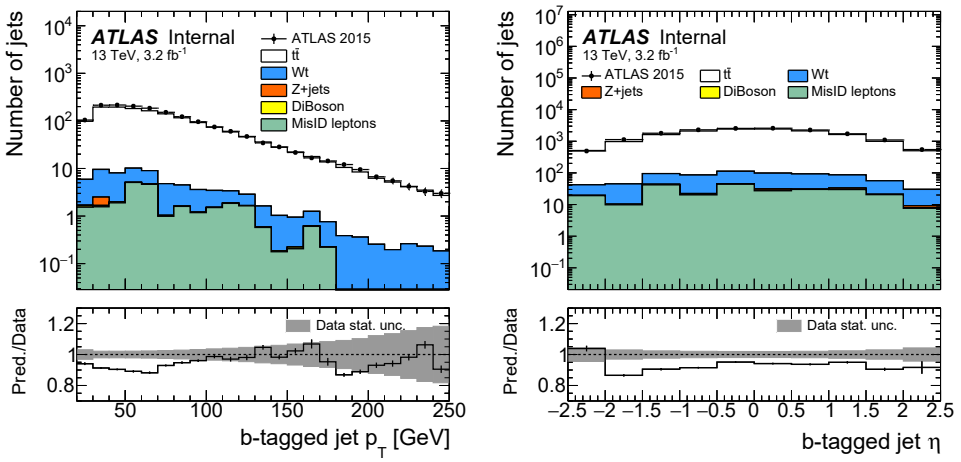

Figure B.2.: Distributions in events fulfilling the standard selection criteria as in Table 8.1 for (a) p_{T} and (b) η of the two b-tagged jets. Uncertainties are statistical only.

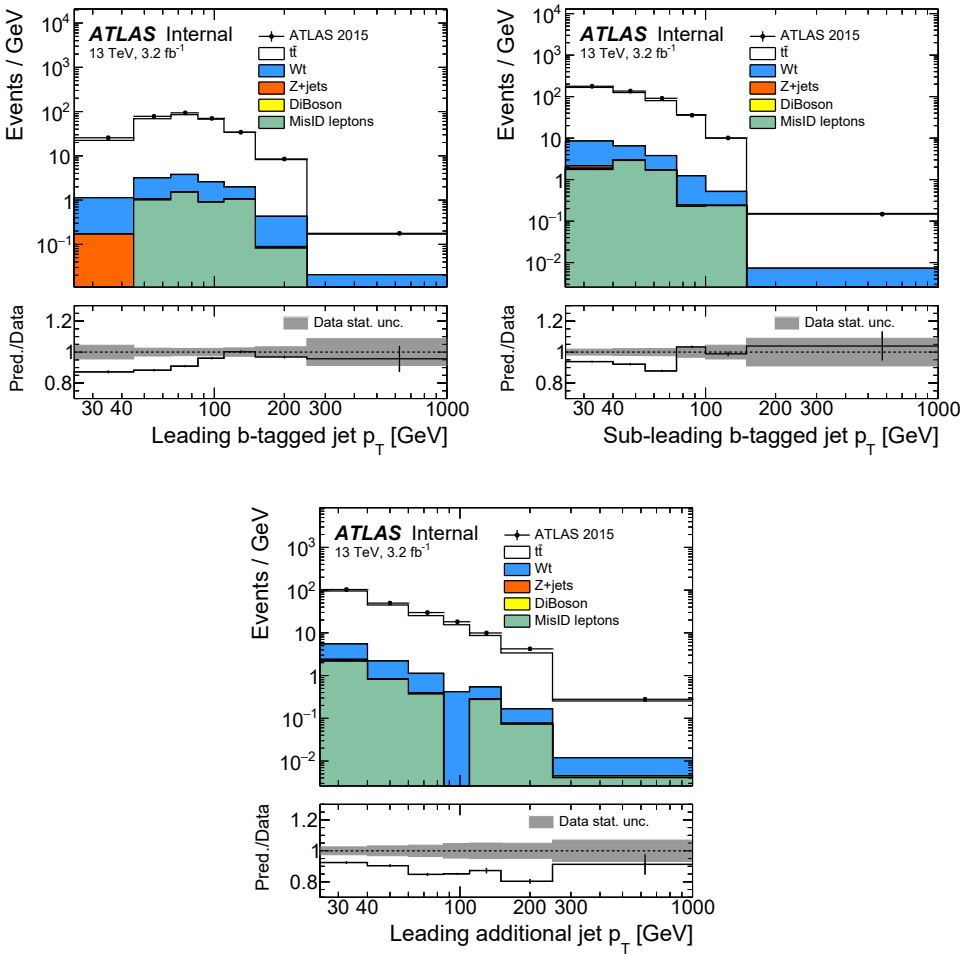

Figure B.3.: Leading b-jet p_{T} (a), sub-leading b-jet p_{T} (b) and leading additional jet p_{T} (c) distributions in events fulfilling the standard selection criteria as in Table 8.1. Uncertainties are statistical only.

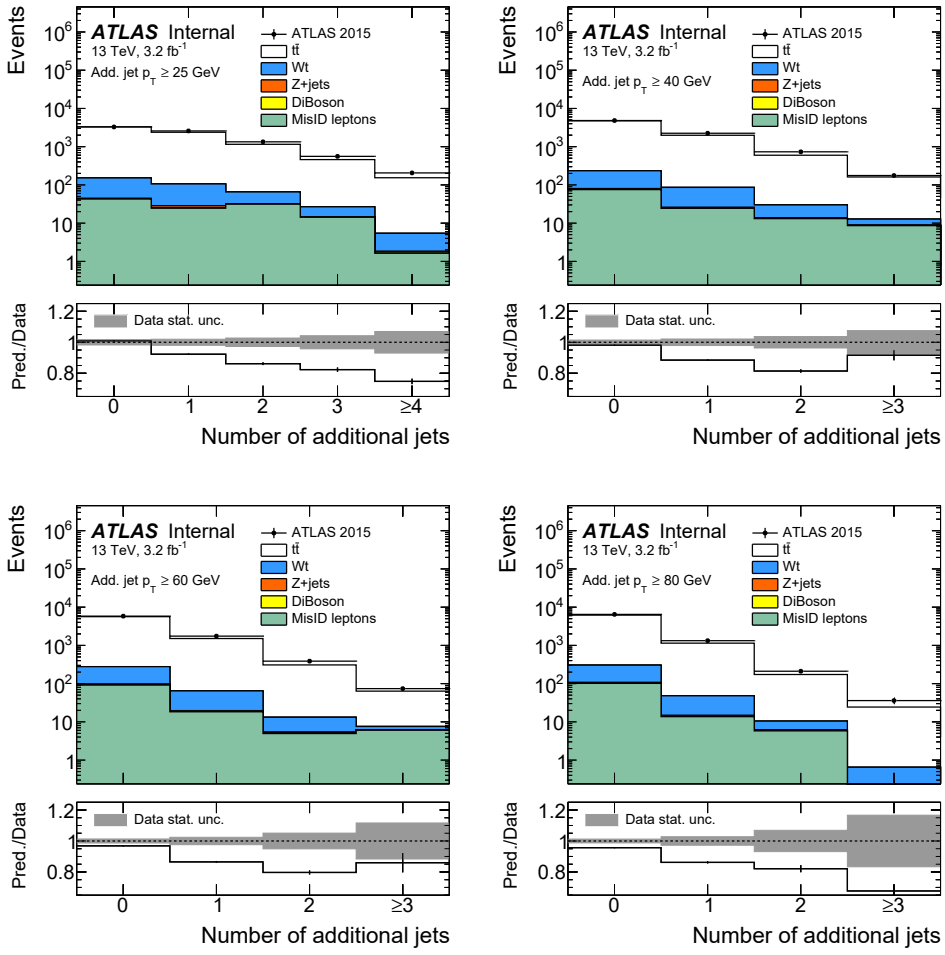

Figure B.4.: Distributions of the additional jet multiplicity in events fulfilling the standard selection criteria as in Table 8.1. Additional jets with (a) jet $p_T > 25$ GeV, (b) jet $p_T > 40$GeV, (c) jet $p_T > 60$ GeV and (d) jet $p_T > 80$ GeV are shown. Uncertainties are statistical only.

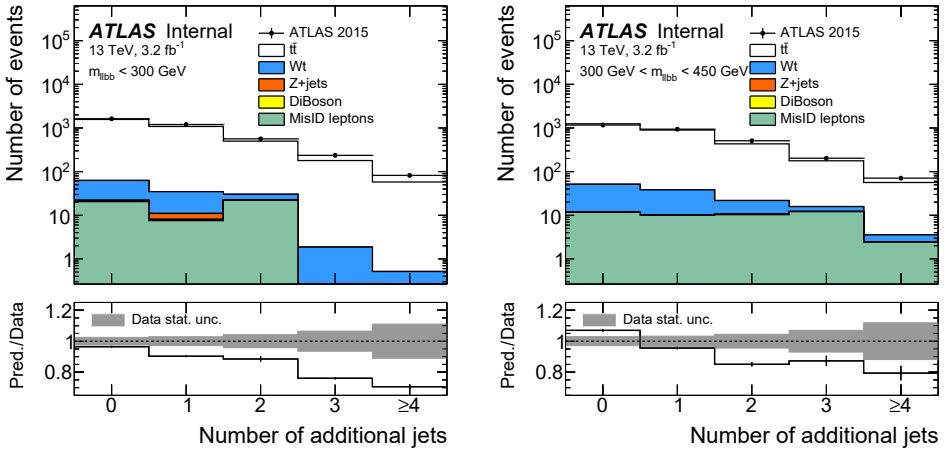

(a) (b)

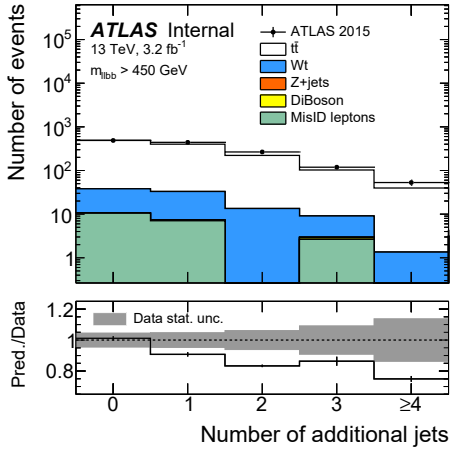

(c)

Figure B.5.: Jet multiplicity distributions in events fulfilling the standard selection criteria as in Table 8.1 for (a) $m_{\mathrm{llbb}} < 300$ GeV, (b) 300 GeV $< m_{\mathrm{llbb}} < 450$ GeV and (c) $m_{\mathrm{llbb}} > 450$ GeV. Uncertainties are statistical only.

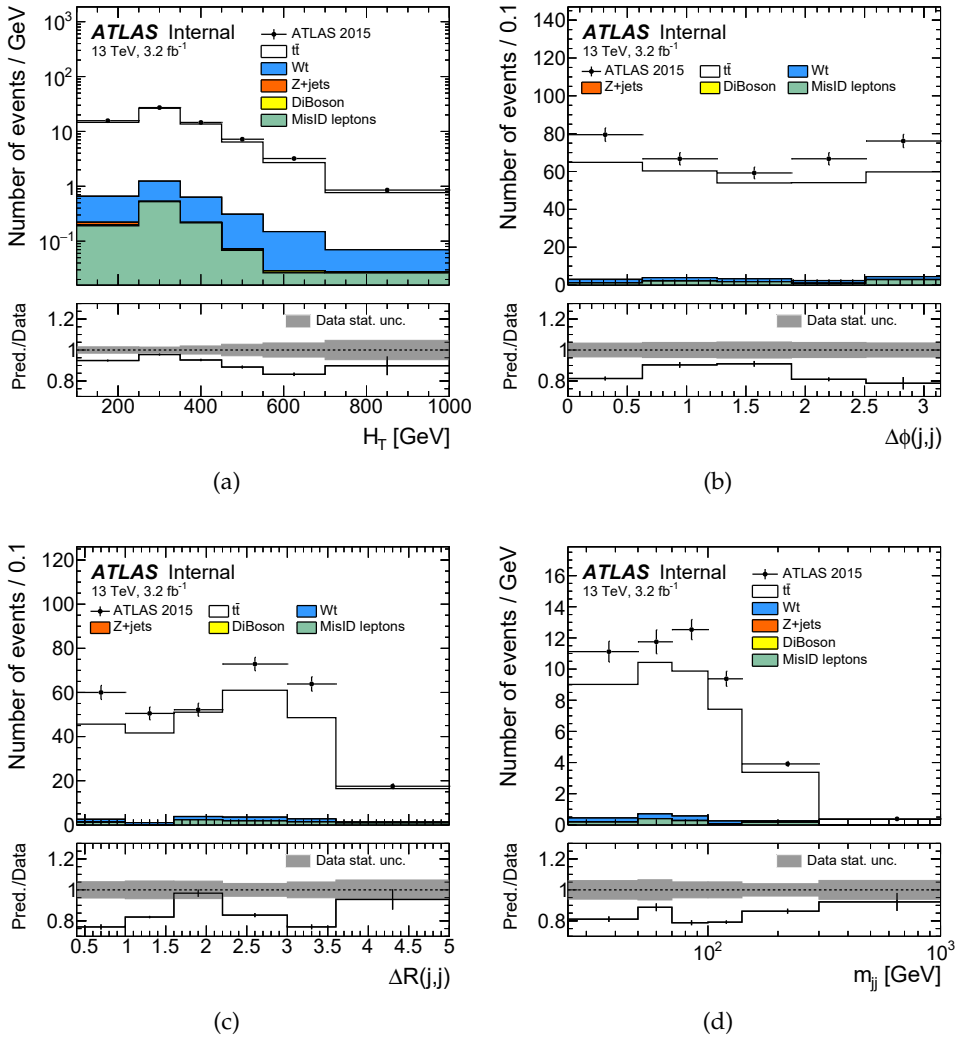

Figure B.6.: Distributions of (a) H_{T}, (b) $\Delta\phi(\mathrm{j},\mathrm{j})$, (c) $\Delta R(\mathrm{j},\mathrm{j})$ and (d) m_{jj} in events fulfilling the standard selection criteria as in Table 8.1. Uncertainties are statistical only.

C. Additional unfolding distributions

C.1. Additional distributions at particle level

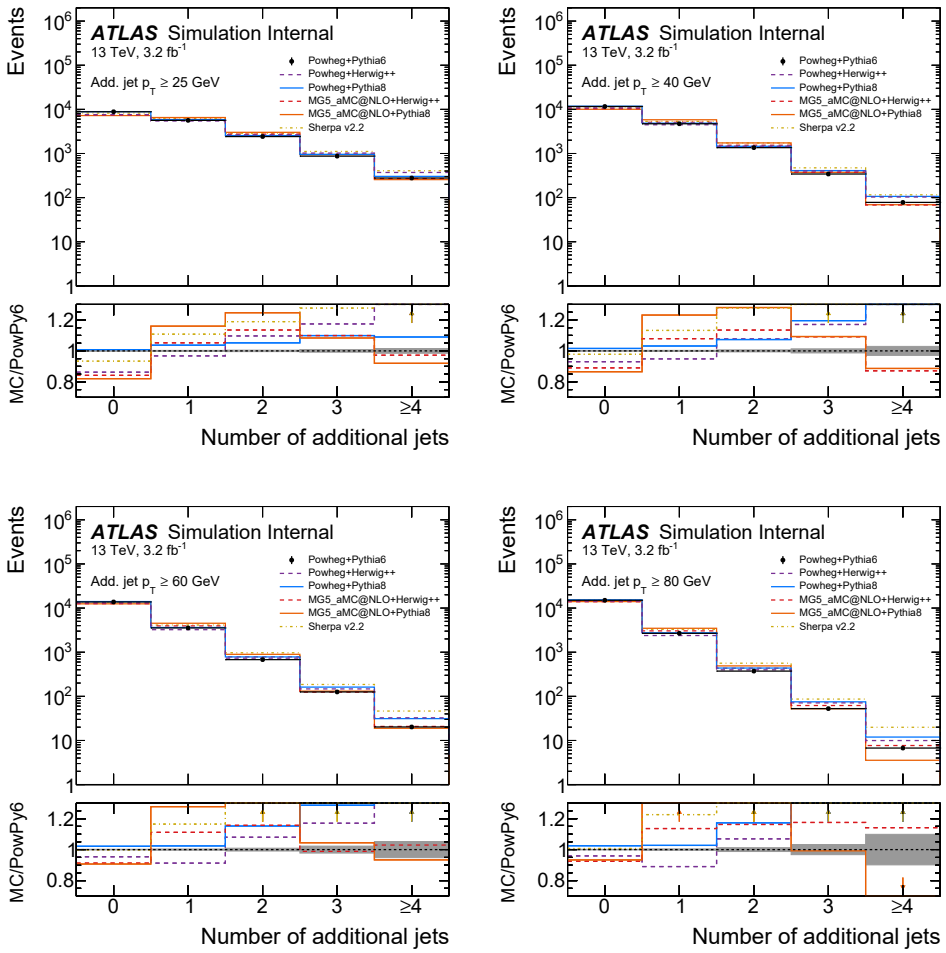

Figure C.1.: Generator comparison of jet multiplicity at particle level for different jet p_{T} thresholds: (a) 25 GeV, (b) 40 GeV, (c) 60 GeV and (d) 80 GeV.

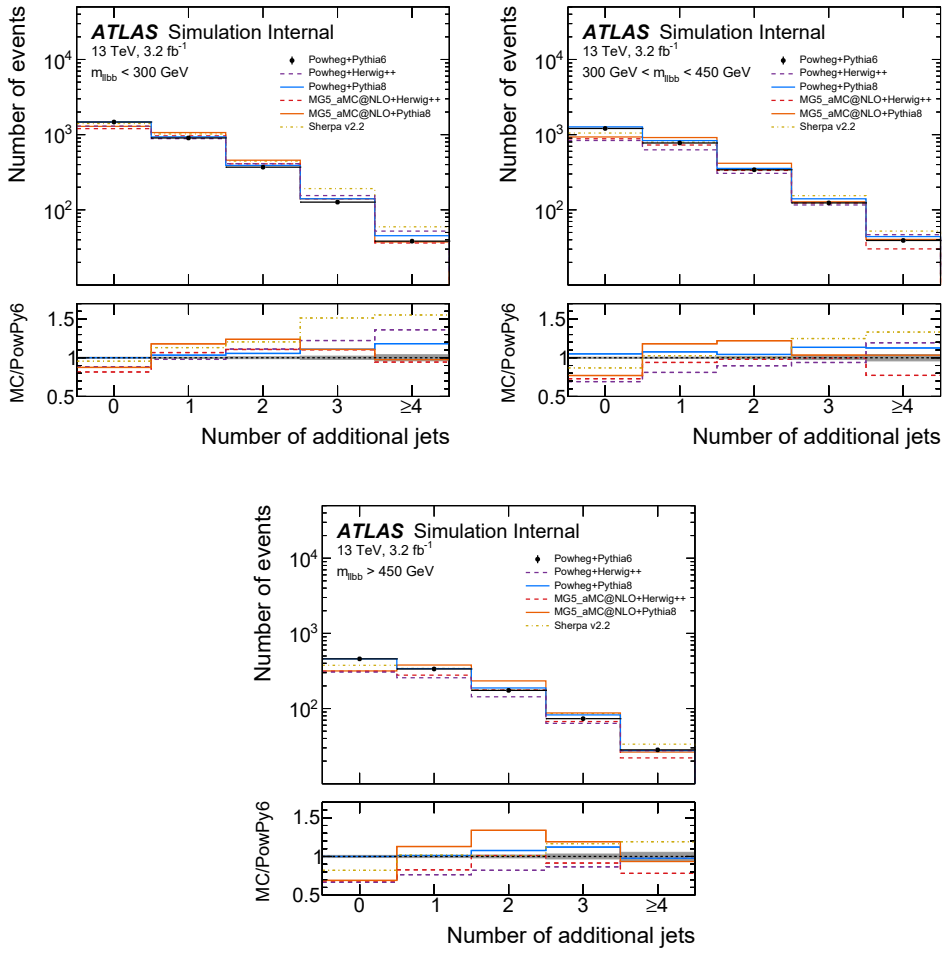

Figure C.2.: Generator comparison of jet multiplicity at particle level in different m_{llbb} regions: (a) m_{llbb} < 300 GeV, (b) 300 GeV < m_{llbb} < 450 GeV and (c) m_{llbb} > 450 GeV. In the bottom pad MC preditions are compared to the baseline Powheg+PYTHIA 6 simulation.

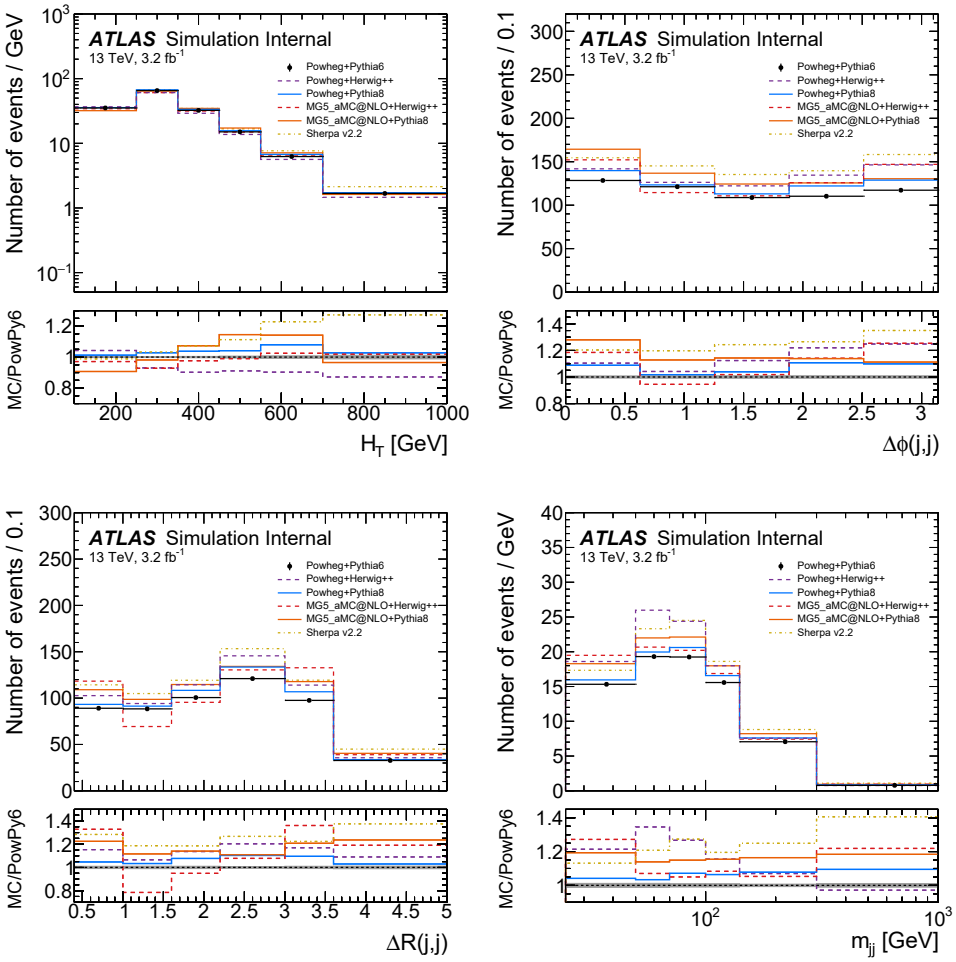

Figure C.3.: Generator comparison of distributions of (a) H_{T}, (b) $\Delta\phi(\mathrm{j},\mathrm{j})$, (c) $\Delta R(\mathrm{j},\mathrm{j})$ and (d) m_{jj} at particle level. In the bottom pad MC preditions are compared to the baseline Powheg+PYTHIA 6 simulation.

C.2. Acceptance correction

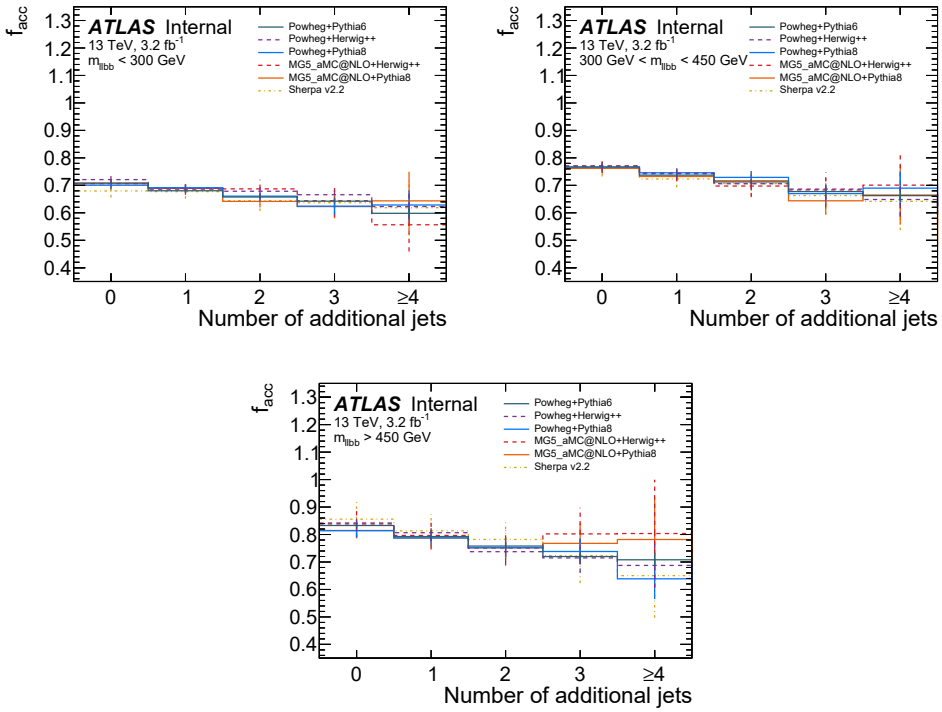

Figure C.4.: Acceptance correction as defined in Equation 9.3 for the jet multiplicity in different m_{llbb} regions: (a) $m_{\mathrm{llbb}} < 300$ GeV, (b) 300 GeV $< m_{\mathrm{llbb}} < 450$ GeV and (c) $m_{\mathrm{llbb}} > 450$ GeV. The additional jets are counted on reconstruction level. The distributions are shown with statistical uncertainties only. The black point represents the corrections from the baseline Powheg+PYTHIA 6 MC, the distributions from other MCs are overlaid just for reference.

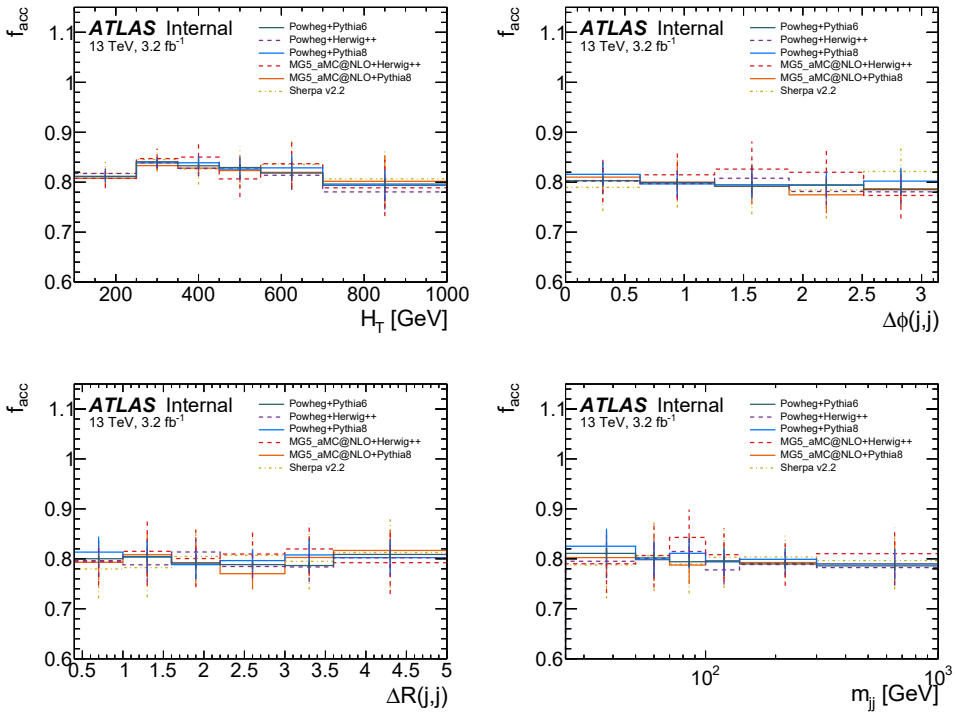

Figure C.5.: Acceptance correction as defined in Equation 9.3 for (a) H_{T}, (b) $\Delta\phi(\mathrm{j},\mathrm{j})$, (c) $\Delta R(\mathrm{j},\mathrm{j})$ and (d) m_{jj} at reconstruction level. The distributions are shown with statistical uncertainties only. The black point represents the corrections from the baseline Powheg+PYTHIA 6 MC, the distributions from other MCs are overlaid just for reference.

C.3. Response matrix

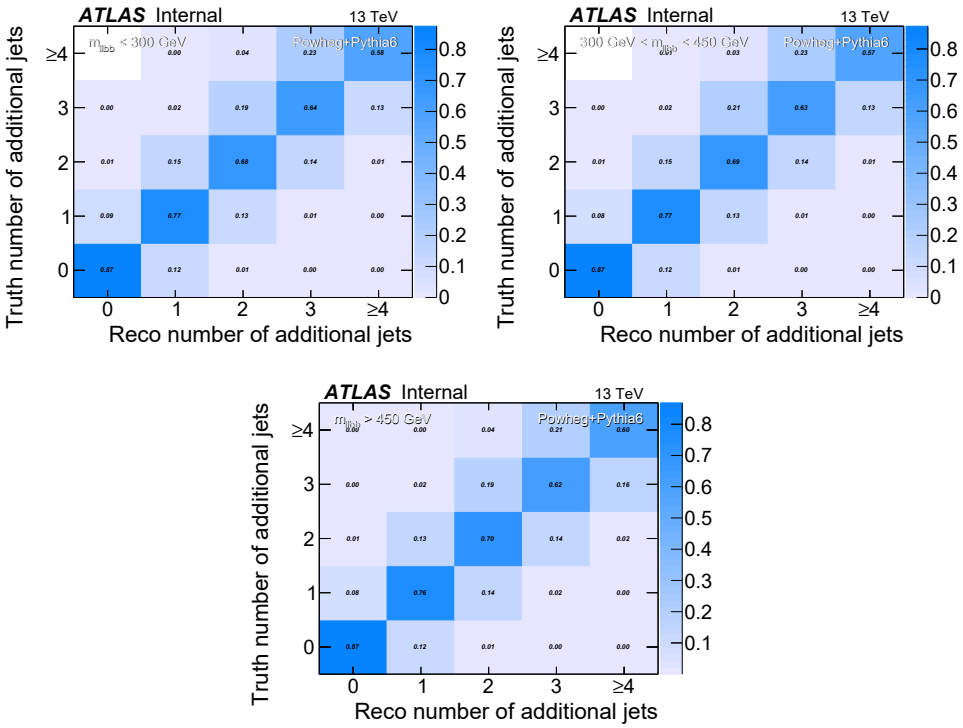

Figure C.6.: Response matrix for the jet multiplicity in different m_{llbb} regions: (a) $m_{\mathrm{llbb}} < 300$ GeV, (b) 300 GeV $< m_{\mathrm{llbb}} < 450$ GeV and (c) $m_{\mathrm{llbb}} > 450$ GeV. The matrix is filled from events of the baseline Powheg+PYTHIA 6 MC where both reconstruction and particle level requirements are fulfilled.

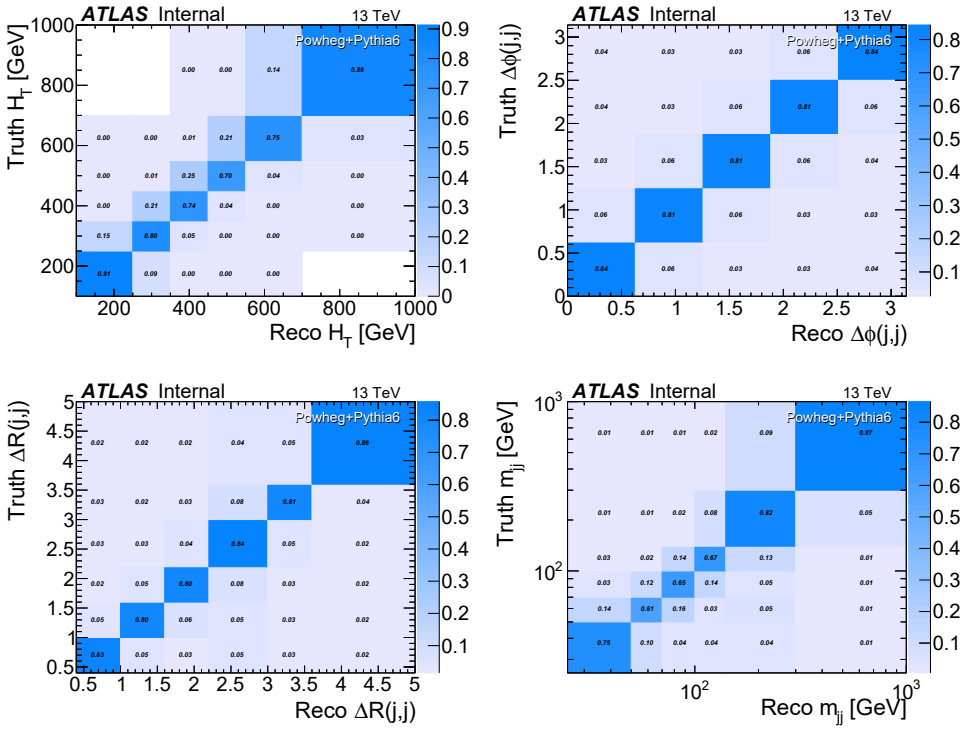

Figure C.7.: Response matrix for (a) H_T, (b) $\Delta\phi(j,j)$, (c) $\Delta R(j,j)$ and (d) m_{jj}. The matrix is filled from events of the baseline Powheg+PYTHIA 6 MC where both reconstruction and particle level requirements are fulfilled.

C.4. Efficiency correction

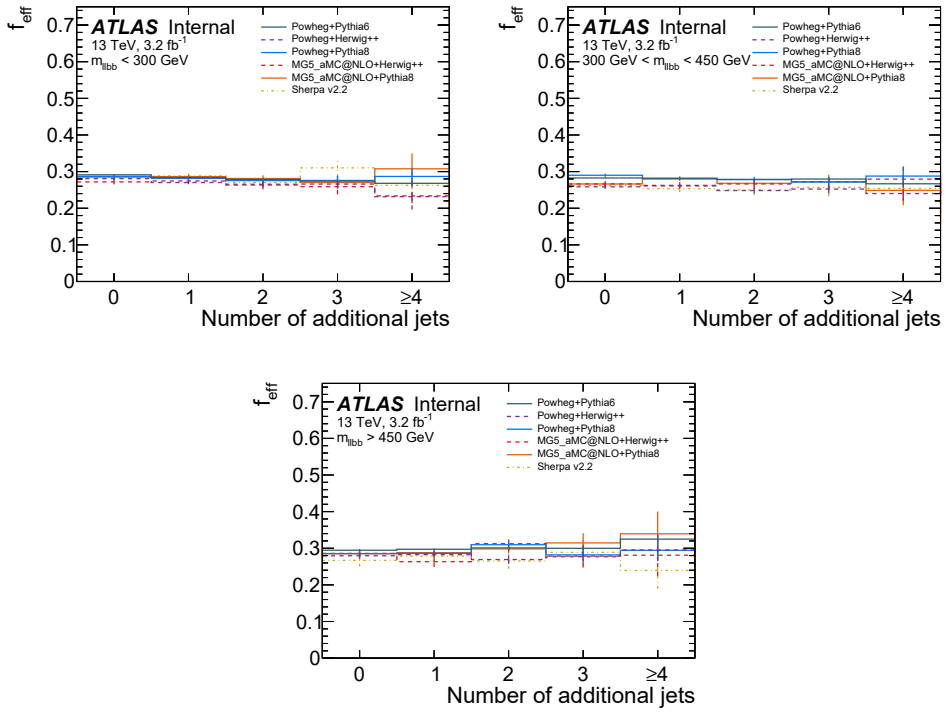

Figure C.8.: Efficiency correction as defined in Equation 9.4 for the jet multiplicity in different m_{llbb} regions: (a) $m_{\text{llbb}} < 300$ GeV, (b) 300 GeV $< m_{\text{llbb}} < 450$ GeV and (c) $m_{\text{llbb}} > 450$ GeV. The additional jets are counted on particle level. The distributions are shown with statistical uncertainties only. The black point represents the corrections from the baseline Powheg+PYTHIA 6 MC, the distributions from other MCs are overlaid just for reference.

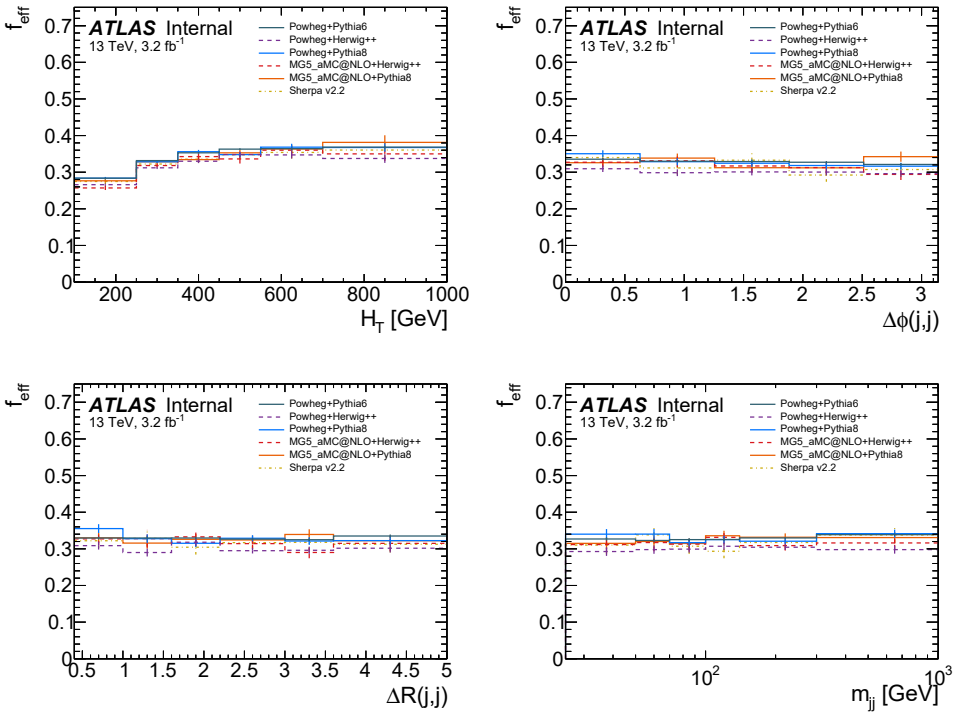

Figure C.9.: Efficiency correction as defined in Equation 9.4 for (a) H_T, (b) $\Delta\phi(j,j)$, (c) $\Delta R(j,j)$ and (d) m_{jj} at particle level. The distributions are shown with statistical uncertainties only. The black point represents the corrections from the baseline Powheg+PYTHIA 6 MC, the distributions from other MCs are overlaid just for reference.

C.5. Closure test

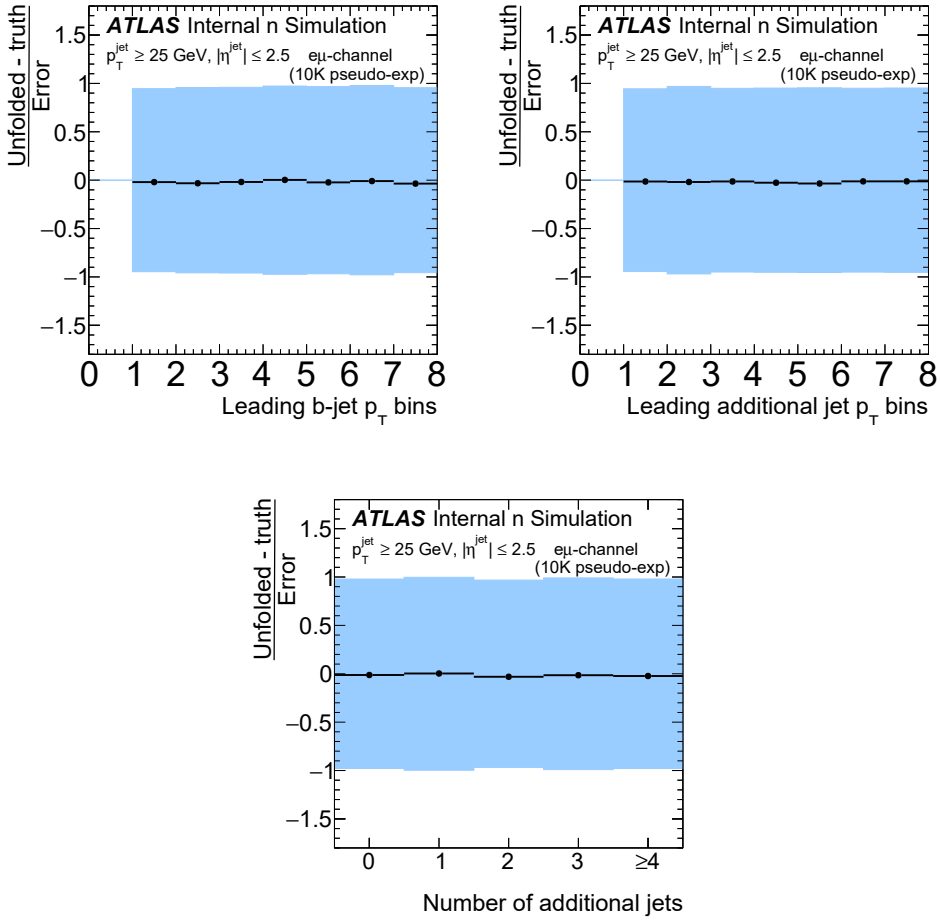

Figure C.10.: Pull distributions as defined in Equation 9.5 for (a) leading b-jet p_T, (b) leading additional jet p_T and (c) jet multiplicity with $p_T > 25$ GeV. The uncertainty on the unfolding method is obtained from mean value of the error from 10000 unfolded distributions (blue band).

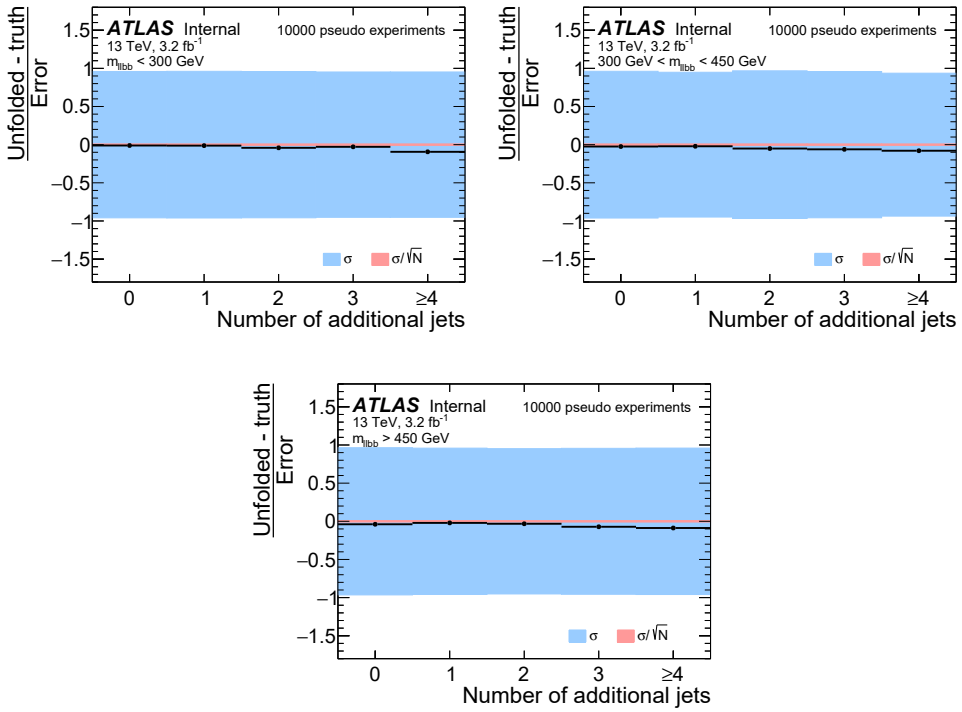

Figure C.11.: Pull distributions as defined in Equation 9.5 for the jet multiplicity in different m_{llbb} regions: (a) $m_{\mathrm{llbb}} < 300$ GeV, (b) 300 GeV $< m_{\mathrm{llbb}} < 450$ GeV and (c) $m_{\mathrm{llbb}} > 450$ GeV. The uncertainty on the unfolding method is obtained from mean value of the error from 10000 unfolded distributions (blue band), where the error from an individual experiment comes from the covariance matrix of the unfolding (red band).

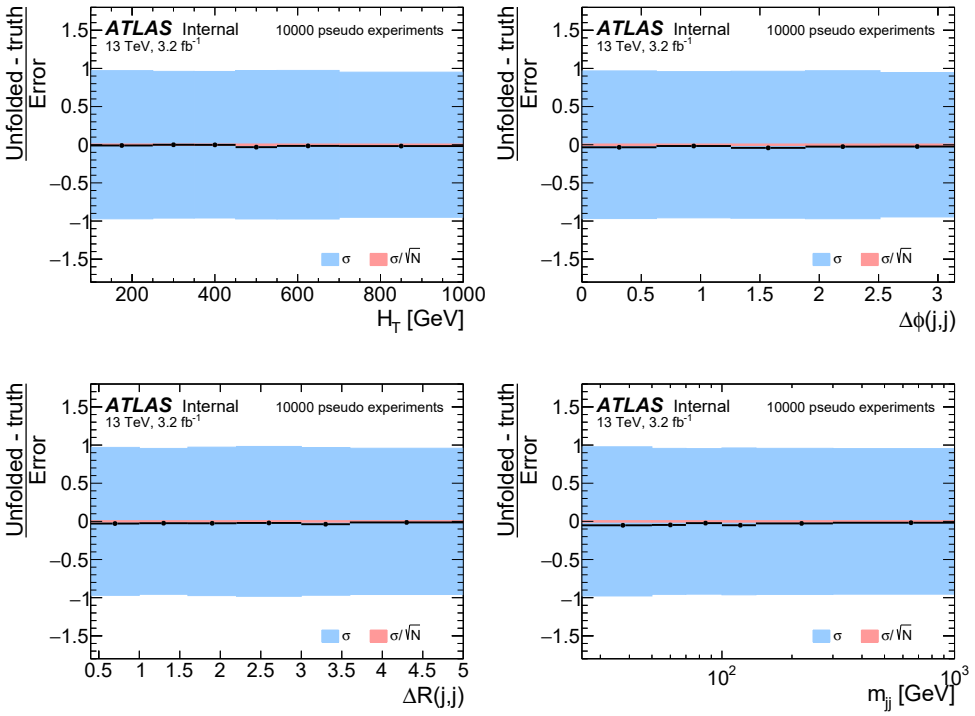

Figure C.12.: Pull distributions as defined in Equation 9.5 for (a) H_{T}, (b) $\Delta\phi(\mathrm{j},\mathrm{j})$, (c) $\Delta R(\mathrm{j},\mathrm{j})$ and (d) m_{jj}. The uncertainty on the unfolding method is obtained from mean value of the error from 10000 unfolded distributions (blue band), where the error from an individual experiment comes from the covariance matrix of the unfolding (red band).

C.6. Stress test

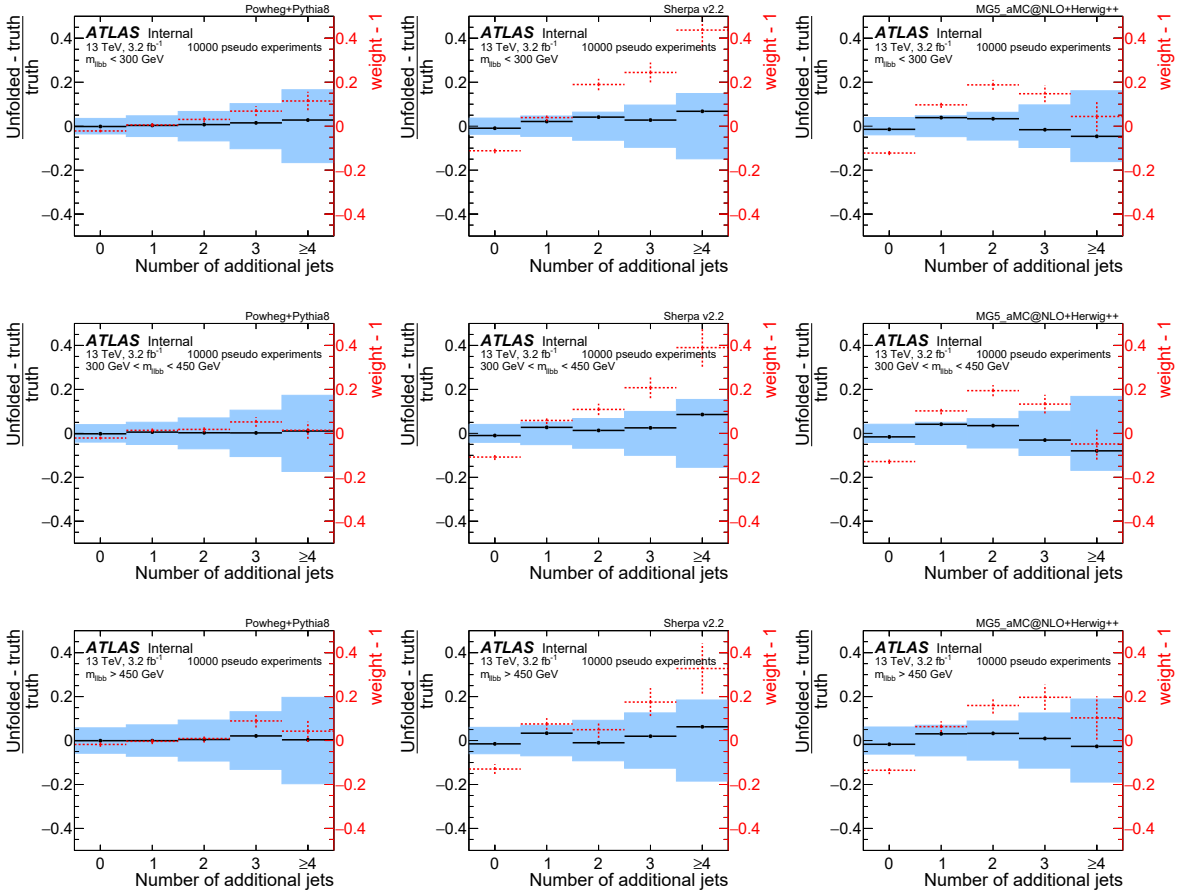

Figure C.13.: Bias distributions representing the stress test as defined in Equation 9.6 for the jet multiplicity in different m_{llbb} regions: (a-c) m_{llbb} < 300 GeV, (d-f) 300 GeV < m_{llbb} < 450 GeV and (g-i) m_{llbb} > 450 GeV. The input distributions are reweighted based on Powheg+PYTHIA 8 (left), Sherpa v2.2 (middle) and MadGraph5_aMC@NLO+Herwig++ (right). The red points visualise the shift (weight-1) from the reweighting, where the weight is the ratio of distributions in the alternative models and Powheg+PYTHIA 6 at the particle level. The black points represent the mean of the Gaussian fit to the bias distribution from 10000 pseudoexperiments and blue band represents the width of the Gaussian.

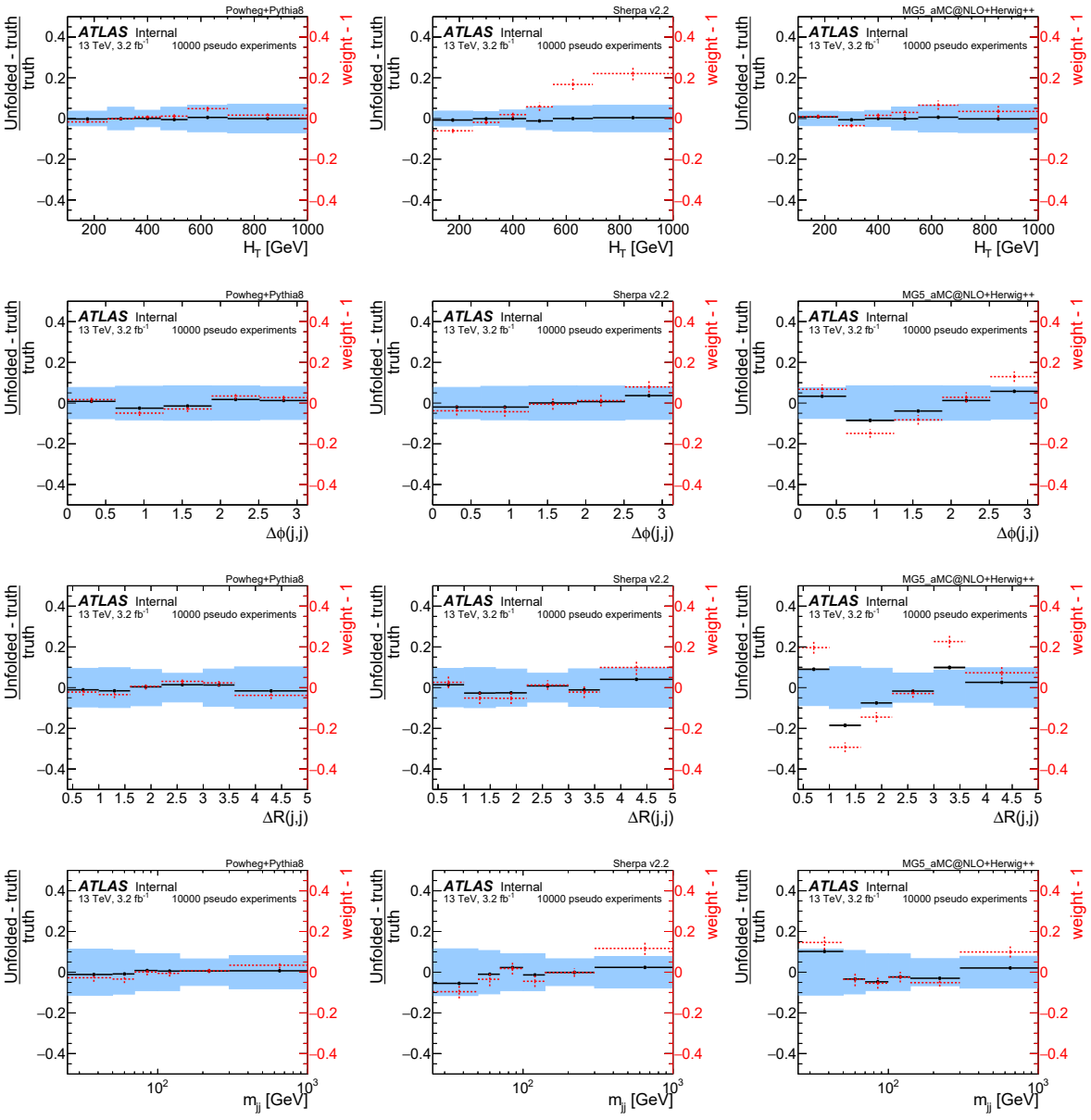

Figure C.14.: Bias distributions representing the stress test as defined in Equation 9.6 for (a-c) H_{T}, (d-f) $\Delta\phi(\mathrm{j},\mathrm{j})$, (g-i) $\Delta R(\mathrm{j},\mathrm{j})$ and (j-l) m_{jj}. The input distributions are reweighted based on Powheg+PYTHIA 8 (left), Sherpa v2.2 (middle) and MadGraph5_aMC@NLO+Herwig++ (right). The red points visualise the shift (weight-1) from the reweighting, where the weight is the ratio of distributions in the alternative models and Powheg+PYTHIA 6 at the particle level. The black points represent the mean of the Gaussian fit to the bias distribution from 10000 pseudoexperiments and blue band represents the width of the Gaussian.

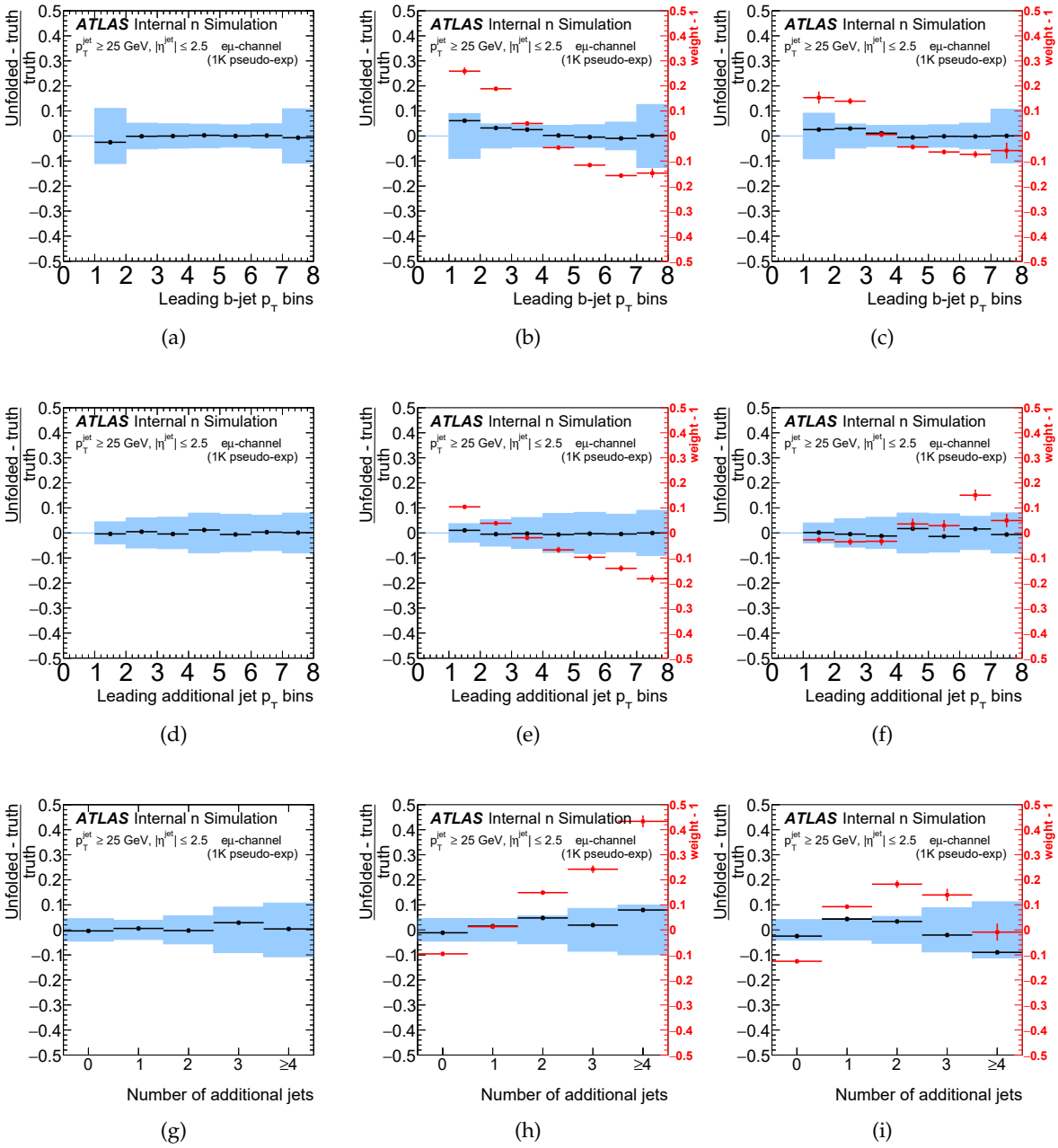

Figure C.15.: Bias distributions representing the stress test as defined in Equation 9.6 for leading b-jet p_{T}(top row), leading additional jet p_{T} (middle row) and jet multiplicity with $p_{\mathrm{T}} > 25$ GeV (bottom row). The input distributions are reweighted based on Powheg+PYTHIA 8 (left), Powheg+Herwig++ (middle) and MadGraph5_aMC@NLO+Herwig++ (right). The red points visualise the shift (weight-1) from the reweighting, where the weight is the ratio of distributions in the alternative models and Powheg+PYTHIA 6 at the particle level. The black points represent the mean of the Gaussian fit to the bias distribution from 10000 pseudoexperiments and blue band represents the width of the Gaussian.

Bibliography

[1] Lyndon Evans and Philip Bryant. LHC Machine. *JINST*, 3:S08001, 2008.

[2] ATLAS Collaboration. Measurement of the $t\bar{t}$ production cross-section as a function of jet multiplicity and jet transverse momentum in 7 TeV proton–proton collisions with the ATLAS detector. *JHEP*, 1501:020, 2015.

[3] ATLAS Collaboration. Measurement of jet activity in top quark events using the $e\mu$ final state with two b-tagged jets in pp collisions at $\sqrt{s} = 8$ TeV with the ATLAS detector. *JHEP*, 09:074, 2016.

[4] Serguei Chatrchyan et al. Measurement of jet multiplicity distributions in $\mathrm{t\bar{t}}$ production in pp collisions at $\sqrt{s} = 7\,\mathrm{TeV}$. *Eur. Phys. J.*, C74:3014, 2015. [Erratum: Eur. Phys. J.C75,no.5,216(2015)].

[5] CMS Collaboration. Measurement of $\mathrm{t\bar{t}}$ production with additional jet activity, including b quark jets, in the dilepton decay channel using pp collisions at $\sqrt{s} = 8\,\mathrm{TeV}$. *Eur. Phys. J.*, C76(7):379, 2016.

[6] CMS Collaboration. Measurement of differential cross sections for top quark pair production using the lepton+jets final state in proton-proton collisions at 13 TeV. *Phys. Rev. D*, 95:092001, 2017.

[7] ATLAS Collaboration. *ATLAS: Detector and physics performance technical design report. Volume 1*. Technical Design Report ATLAS. CERN, Geneva, 1999.

[8] Oliver Sim Brüning, Paul Collier, P Lebrun, Stephen Myers, Ranko Ostojic, John Poole, and Paul Proudlock. *LHC Design Report*. CERN, Geneva, 2004.

[9] Christiane Lefèvre. The CERN accelerator complex. Complexe des accélérateurs du CERN, Dec 2008.

[10] ATLAS collaboration. The ATLAS Inner Detector commissioning and calibration. *Eur. Phys. J.*, C70:787–821, 2010.

[11] Karolos Potamianos. The upgraded Pixel detector and the commissioning of the Inner Detector tracking of the ATLAS experiment for Run-2 at the Large Hadron Collider. *PoS*, EPS-HEP2015:261, 2015.

[12] David J Griffiths. *Introduction to elementary particles; 2nd rev. version*. Physics textbook. Wiley, New York, NY, 2008.

[13] ATLAS collaboration. Observation of a new particle in the search for the standard model higgs boson with the atlas detector at the lhc. *Physics Letters B*, 716(1):1 – 29, 2012.

[14] CMS collaboration. Observation of a new boson at a mass of 125 gev with the cms experiment at the lhc. *Physics Letters B*, 716(1):30 – 61, 2012.

[15] Andrew Purcell. GO ON A PARTICLE QUEST AT THE FIRST CERN WEBFEST. https://cds.cern.ch/journal/CERNBulletin/2012/35/News%20Articles/1473657, 2012. [Online; accessed 01-March-2018].

[16] ATLAS collaboration. Summary plots from the ATLAS Top physics group. https://atlas.web.cern.ch/Atlas/GROUPS/PHYSICS/CombinedSummaryPlots/TOP/, 2018. [Online; accessed 03-March-2018].

[17] John C. Collins, Davison E. Soper, and George F. Sterman. Factorization of Hard Processes in QCD. *Adv. Ser. Direct. High Energy Phys.*, 5:1–91, 1989.

[18] Joseph R. Incandela, Arnulf Quadt, Wolfgang Wagner, and Daniel Wicke. Status and Prospects of Top-Quark Physics. *Prog. Part. Nucl. Phys.*, 63:239–292, 2009.

[19] Andy Buckley, James Ferrando, Stephen Lloyd, Karl Nordström, Ben Page, Martin Rüfenacht, Marek Schönherr, and Graeme Watt. LHAPDF6: parton density access in the LHC precision era. *Eur. Phys. J.*, C75:132, 2015.

[20] Michal Czakon, Paul Fiedler, and Alexander Mitov. Total Top-Quark Pair-Production Cross Section at Hadron Colliders Through $O(\alpha\frac{4}{S})$. *Phys. Rev. Lett.*, 110:252004, 2013.

[21] C. Patrignani et al. Review of Particle Physics. *Chin. Phys.*, C40(10):100001, 2016.

[22] Torbjorn Sjostrand. Monte Carlo Tools. In *Proceedings, 65th Scottish Universities Summer School in Physics: LHC Physics (SUSSP65): St. Andrews, UK, August 16-29, 2009*, pages 309–339, 2009.

[23] Stefan Hoeche. Monte Carlo Simulations. https://theory.slac.stanford.edu/our-research/simulations. [Online; accessed 03-March-2018].

[24] Andy Buckley et al. General-purpose event generators for LHC physics. *Phys. Rept.*, 504:145–233, 2011.

[25] Torbjorn Sjostrand. Jet Fragmentation of Nearby Partons. *Nucl. Phys.*, B248:469–502, 1984.

[26] Bo Andersson, G. Gustafson, G. Ingelman, and T. Sjostrand. Parton Fragmentation and String Dynamics. *Phys. Rept.*, 97:31–145, 1983.

[27] B. R. Webber. A QCD Model for Jet Fragmentation Including Soft Gluon Interference. *Nucl. Phys.*, B238:492–528, 1984.

[28] T. Sjöstrand, S. Mrenna, and P. Skands. Pythia 6.4 Physics and Manual. *JHEP*, 0605:026, 2006.

[29] T. Sjöstrand, S. Mrenna, and P. Skands. A Brief Introduction to Pythia 8.1. *Comput. Phys. Commun.*, 178:852, 2008.

[30] M. Bahr et al. Herwig++ Physics and Manual. *Eur. Phys. J. C*, 58:639–707, 2008.

[31] Johannes Bellm et al. Herwig 7.0/Herwig++ 3.0 release note. *Eur. Phys. J.*, C76(4):196, 2016.

[32] Stefan Hoeche, Frank Krauss, Marek Schonherr, and Frank Siegert. QCD matrix elements + parton showers: The NLO case. *JHEP*, 04:027, 2013.

[33] P. Bartalini et al. Multi-Parton Interactions at the LHC. *arXiv:1111.0469*, Nov 2011.

[34] J. Alwall, R. Frederix, S. Frixione, V. Hirschi, F. Maltoni, O. Mattelaer, H. S. Shao, T. Stelzer, P. Torrielli, and M. Zaro. The automated computation of tree-level and next-to-leading order differential cross sections, and their matching to parton shower simulations. *JHEP*, 07:079, 2014.

[35] Paolo Nason. A new method for combining NLO QCD with shower Monte Carlo algorithms. *JHEP*, 0411:040, 2004.

[36] Stefano Frixione, Paolo Nason, and Carlo Oleari. Matching NLO QCD computations with Parton Shower simulations: the POWHEG method. *JHEP*, 0711:070, 2007.

[37] S. Agostinelli et al. GEANT4: A simulation toolkit. *Nucl. Instrum. Meth.*, A506:250–303, 2003.

[38] ATLAS Collaboration. The ATLAS Simulation Infrastructure. *Eur. Phys. J. C*, 70:823–874, 2010.

[39] ATLAS Collaboration. The simulation principle and performance of the ATLAS fast calorimeter simulation FastCaloSim. Technical Report ATL-PHYS-PUB-2010-013, CERN, Geneva, Oct 2010.

[40] Simone Alioli, Paolo Nason, Carlo Oleari, and Emanuele Re. A general framework for implementing NLO calculations in shower Monte Carlo programs: the POWHEG BOX. *JHEP*, 1006:043, 2010.

[41] Hung-Liang Lai, Marco Guzzi, Joey Huston, Zhao Li, Pavel M. Nadolsky, et al. New parton distributions for collider physics. *Phys. Rev. D*, 82:074024, 2010.

[42] ATLAS Collaboration. Simulation of top quark production for the ATLAS experiment at $\sqrt{s} = 13$ TeV. Technical Report ATL-PHYS-PUB-2016-004, CERN, Geneva, Jan 2016.

[43] Peter Zeiler Skands. Tuning Monte Carlo Generators: The Perugia Tunes. *Phys. Rev. D*, 82:074018, 2010.

[44] Daniel Stump, Joey Huston, Jon Pumplin, Wu-Ki Tung, H. L. Lai, Steve Kuhlmann, and J. F. Owens. Inclusive jet production, parton distributions, and the search for new physics. *JHEP*, 10:046, 2003.

[45] ATLAS Collaboration. Measurements of normalized differential cross sections for $t\bar{t}$ production in pp collisions at $\sqrt{s} = 7$ TeV using the ATLAS detector. *Phys. Rev. D*, 90(7):072004, 2014.

[46] ATLAS Collaboration. ATLAS Run 1 Pythia8 tunes. Technical Report ATL-PHYS-PUB-2014-021, CERN, Geneva, Nov 2014.

[47] T. Gleisberg, Stefan. Hoeche, F. Krauss, M. Schonherr, S. Schumann, et al. Event generation with SHERPA 1.1. *JHEP*, 0902:007, 2009.

[48] Fabio Cascioli, Philipp Maierhofer, and Stefano Pozzorini. Scattering Amplitudes with Open Loops. *Phys. Rev. Lett.*, 108:111601, 2012.

[49] Tanju Gleisberg and Stefan Höche. Comix, a new matrix element generator. *JHEP*, 0812:039, 2008.

[50] Steffen Schumann and Frank Krauss. A Parton shower algorithm based on Catani-Seymour dipole factorisation. *JHEP*, 03:038, 2008.

[51] Höche, Stefan and Krauss, Frank and Schonherr, Marek and Siegert, Frank. QCD matrix elements + parton showers: The NLO case. *JHEP*, 04:027, 2013.

[52] Nikolaos Kidonakis. Two-loop soft anomalous dimensions for single top quark associated production with a W^- or H^-. *PRD*, 82:054018, 2010.

[53] Stefano Frixione, Eric Laenen, Patrick Motylinski, Bryan R. Webber, and Chris D. White. Single-top hadroproduction in association with a W boson. *JHEP*, 07:029, 2008.

[54] J Butterworth, E Dobson, U Klein, B Mellado Garcia, T Nunnemann, J Qian, D Rebuzzi, and R Tanaka. Single Boson and Diboson Production Cross Sections in pp Collisions at sqrts=7 TeV. *ATL-COM-PHYS-2010-695*, 2010.

[55] ATLAS Collaboration. Charged-particle distributions in $\sqrt{s} = 13$ TeV pp interactions measured with the ATLAS detector at the LHC. *Phys. Lett. B*, 758:67–88, 2016.

[56] Gavin P. Salam and Gregory Soyez. A Practical Seedless Infrared-Safe Cone jet algorithm. *JHEP*, 05:086, 2007.

[57] Matteo Cacciari, Gavin P. Salam, and Gregory Soyez. The anti-k_t jet clustering algorithm. *JHEP*, 04:063, 2008.

[58] S. Catani, Yuri L. Dokshitzer, M. Olsson, G. Turnock, and B.R. Webber. New clustering algorithm for multi - jet cross-sections in e+ e- annihilation. *Phys.Lett.*, B269:432–438, 1991.

[59] Stephen D. Ellis and Davison E. Soper. Successive combination jet algorithm for hadron collisions. *Phys. Rev. D*, 48:3160–3166, 1993.

[60] S. Catani, Yuri L. Dokshitzer, M. H. Seymour, and B. R. Webber. Longitudinally invariant K_t clustering algorithms for hadron hadron collisions. *Nucl. Phys. B*, 406:187–224, 1993.

[61] Yuri L. Dokshitzer, G.D. Leder, S. Moretti, and B.R. Webber. Better jet clustering algorithms. *JHEP*, 9708:001, 1997.

[62] M. Wobisch and T. Wengler. Hadronization corrections to jet cross-sections in deep inelastic scattering. *hep-ph/9907280*, 1998.

[63] Matteo Cacciari and Gavin P. Salam. Dispelling the N^3 myth for the k_t jet-finder. *Phys. Lett. B*, 641:57–61, 2006.

[64] Matteo Cacciari, Gavin P. Salam, and Gregory Soyez. FastJet user manual. *Eur. Phys. J. C*, 72:1896, 2012.

[65] Gavin P. Salam. Towards jetography. *Eur. Phys. J. C*, 67:637, 2010.

[66] ATLAS collaboration. Measurement of jet activity produced in top-quark events with an electron, a muon and two b-tagged jets in the final state in pp collisions at $\sqrt{s} = 13$ TeV with the ATLAS detector. *Eur. Phys. J.*, C77(4):220, 2017.

[67] ATLAS Collaboration. Measurement of $t\bar{t}$ production with a veto on additional central jet activity in pp collisions at $\sqrt{s} = 7$ TeV using the ATLAS detector. *Eur. Phys. J. C*, 72:2043, 2012.

[68] ATLAS Collaboration. Comparison of Monte Carlo generator predictions from Powheg and Sherpa to ATLAS measurements of top pair production at 7 TeV. ATL-PHYS-PUB-2015-011, 2015.

[69] ATLAS Collaboration. Comparison of Monte Carlo generator predictions to ATLAS measurements of top pair production at 7 TeV. Technical Report ATL-PHYS-PUB-2015-002, CERN, Geneva, Jan 2015.

[70] ATLAS Collaboration. Further ATLAS tunes of PYTHIA 6 and Pythia 8. ATL-PHYS-PUB-2011-014, 2011.

[71] A. D. Martin, W. J. Stirling, R. S. Thorne and G. Watt. Parton distributions for the LHC. *Eur. Phys. J. C*, 63:189, 2009.

[72] Joseph Reichert. The Upgrade and Performance of the ATLAS Electron and Photon Triggers Towards Run 2. Technical Report ATL-DAQ-PROC-2015-037, CERN, Geneva, Oct 2015.

[73] Rafal Bielski. The ATLAS Muon Trigger Performance in Run I and Initial Run II Performance. Technical Report ATL-DAQ-PROC-2015-029, CERN, Geneva, Sep 2015.

[74] ATLAS Collaboration. Top Reconstruction Group. `https://twiki.cern.ch/twiki/bin/view/AtlasProtected/TopReconstructionGroup`. Accessed: 2015-11-04.

[75] T. Cornelissen, M. Elsing, I. Gavrilenko, W. Liebig, E. Moyse, and A. Salzburger. The new ATLAS track reconstruction (NEWT). *J. Phys. Conf. Ser.*, 119:032014, 2008.

[76] A Salzburger. The ATLAS Track Extrapolation Package. Technical Report ATL-SOFT-PUB-2007-005. ATL-COM-SOFT-2007-010, CERN, Geneva, Jun 2007.

[77] Guennadi Borissov, David William Casper, Kathryn Grimm, Simone Pagan Griso, Lars Egholm Pedersen, Kirill Prokofiev, Matthew Scott Rudolph, and Andrew Mark Wharton. ATLAS strategy for primary vertex reconstruction during Run-2 of the LHC. Technical Report ATL-SOFT-PROC-2015-016. 7, CERN, Geneva, May 2015.

[78] W. Lampl et al. Calorimeter clustering algorithms: Description and performance. *ATL-LARG-PUB-2008-002*, 2008. https://cdsweb.cern.ch/record/1099735.

[79] ATLAS collaboration. Jet energy measurement with the ATLAS detector in proton-proton collisions at $\sqrt{s} = 7$ TeV. *Eur. Phys. J.*, C73(3):2304, 2013.

[80] ATLAS collaboration. Selection of jets produced in 13TeV proton-proton collisions with the ATLAS detector. Technical Report ATLAS-CONF-2015-029, CERN, Geneva, Jul 2015.

[81] ATLAS Collaboration. Jet Calibration and Systematic Uncertainties for Jets Reconstructed in the ATLAS Detector at $\sqrt{s} = 13$ TeV. Technical Report ATL-PHYS-PUB-2015-015, CERN, Geneva, Jul 2015.

[82] ATLAS collaboration. Monte Carlo Calibration and Combination of In-situ Measurements of Jet Energy Scale, Jet Energy Resolution and Jet Mass in ATLAS. Technical Report ATLAS-CONF-2015-037, CERN, Geneva, Aug 2015.

[83] Matteo Cacciari, Gavin P. Salam, and Gregory Soyez. The Catchment Area of Jets. *JHEP*, 04:005, 2008.

[84] The ATLAS collaboration. Jet global sequential corrections with the ATLAS detector in proton-proton collisions at sqrt(s) = 8 TeV. Technical Report ATLAS-CONF-2015-002, CERN, Geneva, Mar 2015.

[85] ATLAS Collaboration. Uncertainty release for analyses using ICHEP2015 calibration version. `https://twiki.cern.ch/twiki/bin/viewauth/AtlasProtected/JetUncertainties2015ICHEP2016`. Accessed: 2016-02-04.

[86] ATLAS collaboration. Jet energy measurement and its systematic uncertainty in proton-proton collisions at $\sqrt{s} = 7$ TeV with the ATLAS detector. *Eur. Phys. J.*, C75:17, 2015.

[87] ATLAS Collaboration. Performance of pile-up mitigation techniques for jets in pp collisions at $\sqrt{s} = 8$ TeV using the ATLAS detector. *Eur. Phys. J.*, C76(11):581, 2016.

[88] ATLAS Collaboration. Expected performance of the ATLAS b-tagging algorithms in Run-2. Technical Report ATL-PHYS-PUB-2015-022, CERN, Geneva, Jul 2015.

[89] The ATLAS collaboration. Calibration of b-tagging using dileptonic top pair events in a combinatorial likelihood approach with the ATLAS experiment. Technical Report ATLAS-CONF-2014-004, CERN, Geneva, Feb 2014.

[90] The ATLAS collaboration. Electron and photon energy calibration with the ATLAS detector using LHC Run 1 data. *Eur. Phys. J.*, C74(10):3071, 2014.

[91] The ATLAS collaboration. Electron efficiency measurements with the ATLAS detector using the 2015 LHC proton-proton collision data. Technical Report ATLAS-CONF-2016-024, CERN, Geneva, Jun 2016.

[92] The ATLAS collaboration. Measurement of the muon reconstruction performance of the ATLAS detector using 2011 and 2012 LHC proton-proton collision data. *Eur. Phys. J.*, C74(11):3130, 2014.

[93] The ATLAS collaboration. Muon reconstruction performance of the ATLAS detector in proton-proton collision data at $\sqrt{s}$ =13 TeV. *Eur. Phys. J.*, C76(5):292, 2016.

[94] The ATLAS collaboration. Electron and photon energy calibration with the ATLAS detector using data collected in 2015 at $\sqrt{s} = 13$ TeV. Technical Report ATL-PHYS-PUB-2016-015, CERN, Geneva, Aug 2016.

[95] ATLAS collaboration. Measurement of the $t\bar{t}$ production cross-section using $e\mu$ events with b-tagged jets in pp collisions at $\sqrt{s}$=13 TeV with the ATLAS detector. *Phys. Lett.*, B761:136–157, 2016.

[96] ATLAS Collaboration. Tagging and suppression of pileup jets with the ATLAS detector. Technical Report ATLAS-CONF-2014-018, CERN, Geneva, May 2014.

[97] G. D'Agostini. A Multidimensional unfolding method based on Bayes' theorem. *Nucl. Instrum. Meth.*, A362:487–498, 1995.

[98] Tim Adye. Unfolding algorithms and tests using RooUnfold. In *Proceedings, PHYSTAT 2011 Workshop on Statistical Issues Related to Discovery Claims in Search Experiments and Unfolding, CERN,Geneva, Switzerland 17-20 January 2011*, pages 313–318, Geneva, 2011. CERN, CERN.

[99] ATLAS Collaboration. Electron energy scale for Run 2. `https://twiki.cern.ch/twiki/bin/view/AtlasProtected/EGammaCalibrationRun2`. Accessed: 2015-09-03.

[100] ATLAS Collaboration. Jet energy scale measurements and their systematic uncertainties in proton-proton collisions at $\sqrt{s} = 13$ TeV with the ATLAS detector. *Physical Review D*, 96(7), Oct 2017.

[101] Francesca Ungaro. Jvt calibrations. Jet Calibration and Resolution meeting, `https://indico.cern.ch/event/478075/contributions/1156283/attachments/1225639/1797670/ungaro_160209_JVT.pdf`, 2016. Accessed: 2017-11-12.

[102] Jon Butterworth et al. PDF4LHC recommendations for LHC Run II. *J. Phys.*, G43:023001, 2016.

[103] ATLAS Collaboration. Measurements of fiducial and differential cross-sections of $t\bar{t}$ production with additional heavy-flavour jets in proton-proton collisions at $\sqrt{s}$ = 13 TeV with the ATLAS detector. Technical Report ATLAS-CONF-2018-029, CERN, Geneva, Jul 2018.

List of Figures

List of Tables

Selbständigkeitserklärung

Ich erkläre, dass ich die Dissertation selbständig und nur unter Verwendung der von mir gemäß §7 Abs. 3 der Promotionsordnung der Mathematisch-Naturwissenschaftlichen Fakultät, veröffentlicht im Amtlichen Mitteilungsblatt der Humboldt-Universität zu Berlin Nr. 126/2014 am 18.11.2014 angegebenen Hilfsmittel angefertigt habe.

Berlin, den 26.03.2019 Christoph Eckardt